UNIVERSITA' DEGLI STUDI DI PARMA

Dottorato di ricerca in Scienza e Tecnologia dei Materiali Innovativi

Ciclo XXVII (2012-2014)

New forms of polar and spin ordering in $Pb_2(Mn,Co)WO_6$ double perovskites: symmetry analysis of ferroic properties.

Coordinatore
Chiar.mo Prof. Enrico Dalcanale

Tutor:
Chiar.mo Prof. Gianluca Calestani
Dott.ssa Lara Righi

Dottorando: Fabio Orlandi

2015

"...What is it indeed that gives us the feeling of elegance in a solution, in a demonstration? It is the harmony of the diverse parts, their symmetry, their happy balance; in a word it is all that introduces order, all that gives unity, that permits us to see clearly and to comprehend at once both the ensemble and the details..."

Henri Poincaré (1854-1912)

In N. Rose Mathematical Maxims and Minims, Raleigh NC:Rome Press Inc., 1988.

Table of Contents

1 Introduction

In recent years, the scientific community focused on the study of new multifunctional materials, in which the simultaneous presence of different functionalities can make a compound useful to fabricate a single device able to handle several tasks. In this framework the multiferroics material, especially the magneto-electric systems, have a special place.

In this type of systems the symmetry constrains, dictated from the magnetic point group, play an essential role regulating all the physical properties and in particular the magneto-electrical coupling in the system. In fact, the Neumann's principle says that, "*the symmetry elements of any physical property of a crystal must include all the symmetry elements of the point group of the crystal*".[1] This brings up the importance of the determination of the magnetic symmetry in this type of compounds. However, except some excellent examples reported in the literature, the problem is very often underestimated, or even neglected.

This PhD thesis presents the study of a double perovskite system, $Pb_2(Mn,Co)WO_6$, that revealed a complex and quite interesting magneto-electric multiferroic character. The study is based on the accurate analysis of the magnetic symmetry that, joined with a comprehensive physical characterization, allows defining in detail the complicated picture of the system properties. The

magnetic symmetry analysis of these compounds was performed taking advantage of the “coloured” superspace formalism. Starting from the analysis of the nuclear incommensurate modulated phases, the superspace formalism was extended to the magnetic structure. Thanks to the Jana2006 software, the formalism was straightforwardly applied to the symmetry analysis of the commensurate and incommensurate magnetic structures found in the system. The “coloured” superspace formalism is based on the knowledge of the magnetic point groups (Shubnikov groups) and on the introduction of additional dimensions to define incommensurate periodical distortions of spin arrangements throughout the magnetic lattice. The refinement of selected parameters related to the magnetic symmetry expressed in an n-dimensional space efficiently determines the solution of the magnetic modulation. The great potential of this method lies in the explicit knowledge of the magnetic and nuclear symmetry of the materials (as stated by the Neumann principle) and in the full exploitation of the symmetry constrains in defining the tensor properties of the system. This assumes a fundamental importance in the characterization of magneto-electric multiferroics, as shown by the study of the $Pb_2(Mn,Co)WO_6$ system, in which the generalized use of the superspace formalism demonstrated to be able to define the possible physical properties of the system. This happened even in presence of commensurate structures, whose description could be accomplished also with conventional tools of structure analysis. However, even in these cases, the superspace approach demonstrates to be the most efficient in offering an easy interpretation of the commensurate-incommensurate phase transitions.

2 State of the Art

2.1 Double perovskites

2.1.1 Crystal structure

The perovskite structure is one of the most common structural prototypes for complex metal oxides in nature, thanks to an unusual lattice flexibility that can allow, trough small distortion, to host different cations with different size and charge. The ideal perovskite structure, ABX_3, has cubic symmetry *Pm-3m,* with the "small" B site cation located in octahedral coordination polyhedra generated by the X anion. The BX_6 octahedra form a corner-sharing framework, whose voids are filled by the larger 12-coordinated A cations. Beside the dimensional control offered by the size of the B and X ions, the possibility to tilt cooperatively the octahedral framework represents an additional degree of freedom that increases the flexibility of the structure in hosting cations with different size and functionality. Moreover the BX_6 octahedra itself can be furthermore distorted via Jahn-Teller effect or ferroelectric instabilities. The distortion of the BX_6 framework requires a progressive symmetry reduction, from the cubic prototype down to monoclinic.

By taking into account only the tilt of the octahedra and by applying group theory, the possible isotropy subgroups are 15[1] and correspond to the possible tilting schemes described by Glazer.[2] Because of this structural flexibility it is not surprising that compounds with perovskite structure exhibit a wide range of electric and magnetic proprieties, going from insulating materials to superconductors,[3] from spin polarized[4] to ionic conductors,[5] from ferromagnetic[6] to magnetic frustrated compounds,[7] from ferroelectric[8] to piezoelectric system.[8] Some of the previous properties are simultaneously shown in perovskite systems, allowing new interesting states like multiferroicity.[9]

Generally, the best chemical way to change the physical properties of a material is the partial substitution of the cations in the structure. In the case of perovskites, the substitution can affect both the A and B sites; recently, the attention of the scientific community was focused on systems where half of the B site cations are substituted by another atom. Two situations are possible in this case: a) the two cations are randomly distributed on the B site of the lattice, that keeps the simple perovskite structure; b) the two cations are perfectly ordered, giving rise to a double perovskite structure usually indicated as $A_2BB'X_6$. The ordering of different cations in the B site drives the symmetry of the system and represents a new degree of freedom in the engineering of the properties.

Three types of cationic ordering are theoretically possible in double perovskites and are shown in figure 2-1. Generally the B site orders in a rock-salt type arrangement in which each B cation is surrounded by six B'; the prototype structure is called elpasolite and refers to the mineral K_2NaAlF_6. A layered structure, where the B and B' cations alternate in one direction, is also possible; this case is typical of some copper compounds, in which a structure organized in layers of elongated and undistorted octahedra allows to accommodate the strong Jahn-Teller effect.[10] Finally, very rarely, the B site orders in a columnar way, but this type of order was observed only when also the A site is occupied by two species.[11] Because of the rarity of the last two

types of ordering, only the rock-salt type one will be taken into account in this thesis.

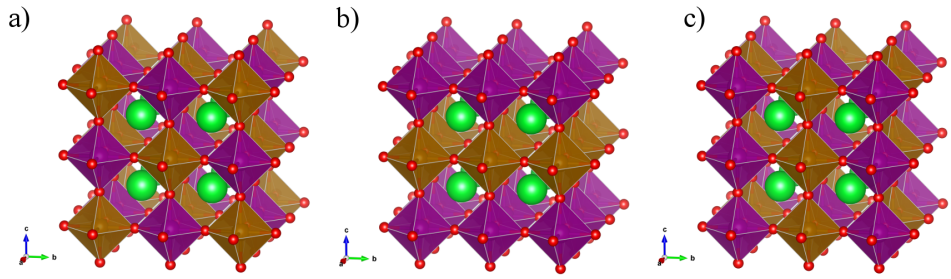

Figure 2-1 Possible types of cationic order in the B site of the $A_2BB'X_6$ double perovskite system: a) rock-salt type, b) layered, c) columnar.

The main driving force for ordering is the difference in the oxidation state of the two cations.[12] By considering two species B and B' with a high charge difference, the minimization of the electrostatic repulsion would lead to hinder the proximity of cations with the highest charge. In a more formal way, the Madelung energy of an order lattice increases proportionally with the B site charge difference. When this energy overcomes the entropic term in determining the free energy of the system, the structure becomes ordered. The ordering is also influenced by the difference of the ionic radii of the two cations, since a regular arrangement of the structure is better realized by alternating smaller and larger atoms, instead to put them randomly. Other but less important factors are, for the oxides, the oxygen content and the covalence of the B-O bond, especially in presence of atoms of the XV and XVI groups like Sb^{5+} or Te^{6+}.[12]

As any real material, also ordered double perovskites contain by entropic reasons defects that can influence the system proprieties. The most interesting are the ones that interrupt the B site order leading to anti-site defects that can extend to anti-phase boundaries, separating two domains in which the B and B' sub-lattices are inverted. These types of defects, generating planes characterized

by B-O-B and B'-O-B' exchange paths, can affect significantly the magnetic properties of the system.

The ordering of the B site implies a symmetry reduction with respect to the simple perovskite and the final space group is constrained by the type of ordering and the bonding geometries dictated by the A, B, and B' species. Since the rock-salt one is the most common type of ordering, in this section we will focus on it. The undistorted $A_2BB'X_6$ structure has cubic *Fm-3m* symmetry and the cell is related to the simple perovskite by the doubling of the lattice parameters. As in case of the simple perovskite, the tilt of the octahedral framework is the most common distortion of the double structures and, by the group analysis conducted by Howard et al.,[13] it leads to twelve possible space groups. This symmetry analysis does not take into account other types of distortion generated by single ion properties, like second order Jahn-Teller effect or bond covalence. For example, when the A site of the perovskite is occupied by Pb^{2+} or Bi^{3+}, the strong stereoactivity of this ions, due to the hybridization of the $6s^2$ doublet with the oxygen *p*-states, can distort the oxygen lattice, further reducing the symmetry and influencing even the B site octahedra. Moreover, in literature are present some examples in which the presence of a *p*-element in the B site of the perovskite induce more produced lattice distortions.[12] Generally all these distortions further reduce the symmetry of the system, inducing in some cases ferroic orders like (anti)-ferroelectricity or piezoelectricity.

The correct assignment of the space group for the double perovskite systems is a crucial point in the study of these compounds, since all the physical properties of the systems are constrained by the point group symmetry (e.g. ferroic proprieties). However, this is often quite complex. As shown earlier, the symmetry is influenced by a series of lattice distortions that are generally related one to another. Furthermore these structural distortions are quite small and masked by strong pseudo-symmetry effect.[14-16] The correct indexing of the powder pattern could be very tricky in these conditions and the unit cell parameters cannot indicate, alone, the correct symmetry of the lattice since that

is contained in the reflection intensities. Unfortunately some cases exist, where different space groups can explain the same powder diffraction pattern, in particular in presence of strong peak overlap or weakness of superstructure reflection.[17] Furthermore, different type of distortions, arising from cationic order, tilt and A-site distortion, can influence the intensity of the same reflections, making the structure solution from powder data very complicated.[12, 14, 15, 18] The problem could be solved by the analysis of single crystal diffraction data. However, in several cases, the presence of pseudo symmetry and/or the crossing of phase transitions during the preparation procedure influence the crystal growth, giving rise to intrinsically twinned crystals that complicate the data analysis.

An accurate symmetry analysis by diffraction data is undoubtedly facilitated by the simultaneous use of different radiations and techniques. The use of synchrotron radiation increase the contribution of the heavy metals, being the atomic scattering factors for X-ray proportional to the atomic number Z, whereas neutron diffraction can improve the contrast of light atoms and electron diffraction can enhance the intensity of superstructure or satellite reflections. Moreover, additional symmetry information can be supplied by the analysis of the physical proprieties of the system, when the presence of anisotropy or ferroic proprieties implies the break of the spatial inversion centre.

2.1.2 Electric and magnetic proprieties of double perovskite

The electric properties of the $A_2BB'X_6$ compounds are mainly driven by the choice of the B cations. The wide range of electric properties observed for the double perovskites, ranging from metallic to insulating materials, is due to the possibility to combine *3d, 4d, 5d* and even *4f* transition metals with different oxidation states. Most of the compounds show insulating to semiconductor behaviour, with conduction mechanisms ranging from thermally activated to small-polaron hopping, to Mott variable-range hopping. Some $A_2BB'X_6$

compounds show metallic behaviour with spin-polarized electron conduction. The prototype compound and probably the most studied one is Sr_2FeMoO_6,[19, 20] that is a ferrimagnetic, half-metallic compound at RT and shows a tunnelling negative magnetoresistive (TMR) effect even at RT and for low magnetic field, which is very interesting for application. The TMR effect and the half metallic character are strongly related; the overlap between the *d*-states of the transition metals and the oxygen *p*-states give rise to a conduction down-spin band. The TMR effect is generated by the tunnelling of the carriers between the different grains of the ceramic sample; indeed no TMR effect was detected in single crystal samples.[21]

Insulating compounds can be used as dielectrics when they present high values of the dielectric constant, low losses and good thermal stability. Different double perovskite systems show very high (in some cases even colossal)[22, 23] values of the dielectric constant, but in most of the cases the dielectric losses and the thermal stability are not suitable for the application. Nevertheless, the possibility of fine-tuning of the proprieties, offered by the cationic substitution, could open new possibilities for application.

Ferroelectric compounds are very interesting in electronics, in particular for the development of non-volatile memories, like Ferroelectric Random Access Memory (FeRAM), for which the stored information is the sign of the electrical polarization. For this application some perovskites, for example the lead zirconium titanate PZT,[24] have been quite used. The ferroelectric ordering is mainly due to polarizabilities of the atoms and to the second order Jahn-Teller effect. For example, in the case of PZT, the d^0 cations in the B site (Ti^{4+} and Zr^{4+}) are shifted from the centre of the coordination octahedron and, joined with the high polarizabilities of the lead ions, generate the ferroelectric properties. In the frame of the double perovskites, the lead-based systems $Pb_2BB'O_6$ gained a lot of attention.[25-32] These compounds usually exhibit high transition temperatures, well above RT, ascribed to antiferroelectric ordering. The degree of ordering of the B site strongly influences the ferroelectric properties. In fact

disordered samples show relaxor behaviour,[29-31] whereas highly ordered samples exhibit classical antiferroelectric proprieties.[27-28]

As for the electronic proprieties, the magnetism in double perovskites is quite complex and various. Thanks to the flexibility of the perovskite structure, different combinations of paramagnetic cations on the A and B sites induce magnetic ground states ranging from classical antiferromagnetic[32, 27] to ferromagnetic[33] arrangements, passing thought ferrimagnetic[34] and glassy states.[35] Given the dual nature of the perovskite lattice, the super-exchange topology is rather complex. When a single paramagnetic atom occupy the B site, like in the A_2BWO_6 systems, there are two possible super-exchange paths that link the magnetic atoms: the 90° nearest neighbour (90NN) path and the 180° next nearest neighbour (180NNN) path, highlighted in figure 2-2. The relative intensity of these two interactions is quite complex to define; in most cases these interactions are of the same order of magnitude and are, usually, in competition giving a frustrated character to the system. In an ideal cubic double perovskite the paramagnetic ions form an edge-sharing tetrahedral lattice; by considering only the 90NN antiferromagnetic interaction, this lead to a geometrical frustration,[35] which however may be removed by the 180NNN interaction or via a spin driven Jahn-Teller effect like in pyrochlore systems.[36]

In the case of two paramagnetic atoms in the B and B' sites the situation is more similar to the single perovskite system. Every B atoms is surrounded by six B' near neighbour and the most short exchange path is the B-O-B' exchange interaction. This interaction is usually the strongest one, but depending on the relative energy of the B and B' orbitals, the overlap could be weak, so that the B-O-B'-O-B interaction may become competitive or even stronger. Anyhow, the possibility to insert in an ordered way two different *d* metals in the structure, allows achieving different types of interactions. Usually insulating oxide with perovskite structure are antiferromagnetic due to the Goodenough[37]-Kanamori[38] rules that indicate ferromagnetic interactions only with combination of half-filled with empty or full orbitals. This combination of orbitals is not possible in

stoichiometric perovskite with a unique B site cation and ferromagnetism in these compounds is due to itinerant electrons or double exchange interactions.

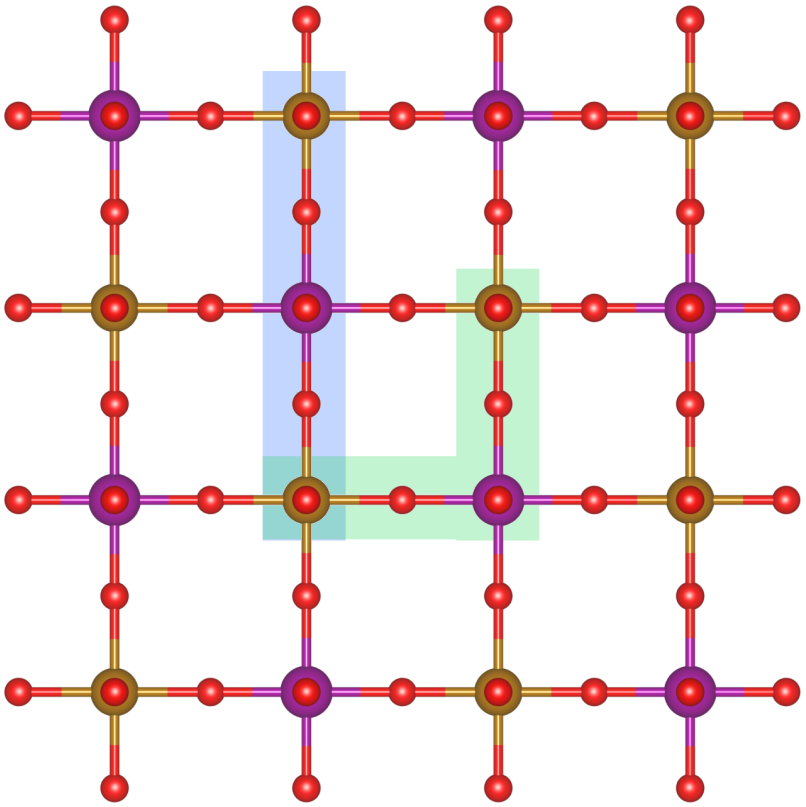

Figure 2-2 Projection of an ordered double perovskite octahedral network; 90° nearest neighbour (90NN) and 180° next nearest neighbour (180NNN) exchange paths are evidenced in green and blue respectively.

The itinerant electrons are quite important also in double perovskites, in particular for what concerns the half-metallic compounds. These systems show ferri-magnetic order[34] with high transition temperature well above RT. In Sr_2FeMoO_6,[19] for example, the iron atoms order ferromagnetically; the same do also the Mo atoms, but with a moment that is reduced with respect to the expected value of $1\mu_B$.[34] Band calculation indicates that the polarised conduction

band is formed principally by the Mo d^1 band[10] and the itinerant character of this electron induces the strong FM coupling of the iron lattice. [20]

The magnetic properties of the system are also strongly influenced by the nature of the A site cation. A first general effect is produced by the lattice distortion induced by the size of the cation, a small ion inducing a tilting of the octahedral network changing the overlap between the B cation and the oxygen orbitals. Another interesting effect was noted by Raevski et al. on the solid solution $Pb_{1-x}Ba_xFe_{1/2}Nb_{1/2}O_3$,[39] where the magnetic transition temperature drops from 120 K to almost 50 K at x = 0.2. It was hypothesized that the presence on the A site of lead atoms induce a new super-exchange interaction between the magnetic atoms, via the strong hybridization of the lead $6s^2$ orbitals with the oxygen *p* states, that is perturbed by the Ba substitution.

In conclusion, double perovskites show a wide range of electric and magnetic proprieties that, in some cases, can be simultaneously present in the system. The possibilities to obtain in the same phase magnetic and electric properties, joined to the possibility to their fine tuning by chemical substitution, makes the double perovskites good candidates to multiferroism. Nevertheless, few works are present in literature concerning the study of multiferroics materials with double perovskite structure and in particular the study of the coupling between the different ferroic ordering in these structures.

2.1.3 Multiferroics

Hans Schmid gave the first definition of multiferroic materials in 1994 as *"... materials, in which two or all three of the properties 'ferroelectricity.' 'ferromagnetism' and 'ferroelasticity' occur simultaneously in the same phase, and in which the magnetic point group has been reliably established by magnetoelectric, optical, dielectric, magnetic and related studies on single crystals and single domains..."*[40] Nowadays the definition takes into account all the long range ordering, like antiferromagnetism, ferrimagnetism etc… , but

some authors in the field define multiferroics only the systems that display a coupling between the ferroic orders. Very interesting are the magnetoelectric multiferroic systems, which allows in principle an electrical control of the magnetization and vice versa, even if a strong coupling between the orders is required for technological application. Such materials could open a new type of information technology in which the information could be storage by magnetic and electric polarization giving rise to a four-state[41] or even eight-stage logic,[42] or surpass the limitation of the current memory technology like reading and writing times, exploiting the magneto-electric effect. For these reasons the publication and the citation in the field are increasing since 2003 (Figure 2-3), year in which Kimura et al.[42] show the magnetic control of the electric polarization in a $TbMnO_3$ single crystal.

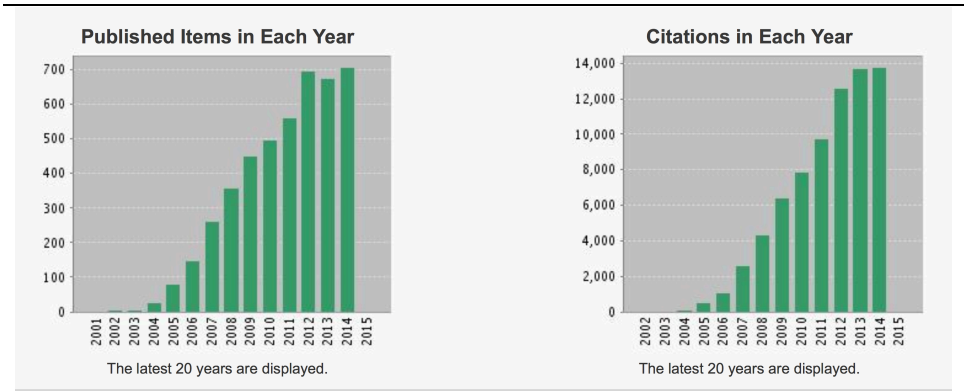

Figure 2-3 Number of publications and citations of paper with topic "multiferroic" from "ISI-web of science"[44]

The definition suggested by Schimid in the '90 is quite restrictive and point out the importance of the knowledge of the magnetic point group and of its "*reliably*" in the study of multiferroics materials. The difficulty in obtaining single-phase multiferroic materials is related to the strong symmetry constrains required by both ferroic orders. On one side the presence of ferroelectricity requires the absence in the point group of the inversion centre, reducing the

possible point group from 32 to 21. However, the lack of the symmetry inversion centre is not a sufficient condition to obtain ferroelectric materials. In fact, the spontaneous polarization in a ferroelectric material must be inverted by the application of an external electric field. This reflects on the point group of the system, that must be polar, limiting the choice to 10 point group: *1, 2, m, mm2, 4, 4mm, 3, 3m, 6, 6mm*. On the other side, the magnetic order requires by definition the breaking of the time-inversion symmetry. The combination between the crystallographic space groups and the time inversion symmetry operation generate the so-called magnetic space groups that will be described in detail in the next chapter. Furthermore it was shown by Hill that the two-ferroic orders try to mutually exclude each other.[45] The ferroelectric proprieties in transition metal oxide materials are generally attributed to a formation of covalent bond that induces displacement of the metal from the centre of the coordination polyhedral. This instability requires usually a d^0 metal, like Ti^{4+} in $BaTiO_3$. On the contrary the magnetic properties are generated by un-paired *d* electrons, in contradiction with the requirement for ferroelectric instability.

The multiferroic magneto-electric materials are generally divided into two groups, Type I and II, on the basis of the microscopic origin of the ferroic properties. In the Type I multiferroics the electric and magnetic ferroic ordering have a different microscopic origin. In particular these materials are proper ferroelectric in which the polarization is induced by an off centring of the cations in the oxygen coordination polyhedra. This ferroelectric distortion can be driven by second order Jahn-Teller effect that induces covalence in the bond between the cation and the oxygen atoms, like in case of a d^0 metal on the B site, or alternatively by a stereoactive role of a lone pair ions like Pb^{2+} or Bi^{3+} in the A site. A classical example of type I multiferroic is $BiFeO_3$.[46] In this compound the ferroelectricity is produced by the stereoactive Bi^{3+} ion and the magnetic properties are induced by the iron sublattice.[46] In multiferroic Type I materials the values of the spontaneous electric and magnetic polarization can be quite large, but the coupling is usually very small or even absent, since the two

proprieties are generate by different sublattices and the ordering phenomena occur at different temperatures.

Type II compounds are improper ferroelectric in which the spontaneous polarization is induced by the magnetic order; this implies a rather strong coupling but the absolute value of the spontaneous electric polarization is usually too small for applicative purposes. From a symmetry point of view the breaking of the time inversion symmetry, required from the magnetic transition, induces the breaking also of the inversion centre and allow the establishment of a spontaneous magnetic and electric polarization. The mechanisms that can induce simultaneously the breaking of the time and spatial inversion symmetry can be divided in two classes: symmetric exchange interaction and the anti-symmetric spin exchange interaction. In the former, observed in collinear structures, the spontaneous electrical polarization **P** is generated by the interaction between neighbour spins that induces a striction of the lattice along defined directions. The generation of **P** require of course some restrictions: a) the sum on the lattice of the striction effects must differ from zero; b) the striction must affect cations with different charge or a tilted polyhedral network, so that the induced distortion could create an unbalance between the barycentres of cations and anions. The induced **P** is proportional to the dot product of neighbour spins

$$P \propto \sum_{i,j} \alpha_{i,j} \vec{S}_i \cdot \vec{S}_j$$

where $\alpha_{i,j}$ is the exchange striction constant. Some examples of this mechanism are supplied by the orthorhombic rare earth perovskites $RMnO_3$ (R=Ho, Er, Tm)[47-49] and some compound of the RMn_2O_5 series.[50-53] The second mechanism is based upon the anti-symmetric exchange interactions and is also known as inverse Dzyaloshinskii-Moriya (DM) interaction. The DM exchange interactions stabilize some types of non-collinear magnetic ordering, like spiral or cycloid ordering, that can break the spatial inversion symmetry. The DM

interaction, in oxide, could be expressed as $D_{i,j} \cdot \vec{S}_i \times \vec{S}_j$ where $\boldsymbol{D_{i,j}}$ is the Dzyaloshinskii-Moriya vector. $\boldsymbol{D_{i,j}}$ is proportional to $\vec{x} \times \vec{r}_{i,j}$ where **x** is the distance of the oxygen atoms from the 180° B-O-B line and $\mathbf{r}_{i,j}$ is the distance between the two magnetic atoms. Since in spiral magnetic ordering the sign of the $\vec{S}_i \times \vec{S}_j$ product is the same for all pairs, the DM interaction push all the oxygen atoms away in the same direction generating a polarization **P** perpendicular to the propagation vector of the magnetic structure. Some interesting examples of this mechanism are for example represented, in case of perovskite structures, by $TbMnO_3$ [43] or, in case of other structures, by $MnWO_4$[54] and CuO[55]. It is worthy to outline that not all the non-collinear or modulated structure can give rise to an electrical polarization. This occurs in particular if the expression of the spiral ordering is invariant with respect to the sign change of the spatial coordinate, as in case of spin-wave structures, where the magnetic order does not break the inversion symmetry.

2.2 Reference

[1] Howard C. J. and Stokes H. T. "*Group-Theoretical Analysis of Octahedral Tilting in Perovskites*" Acta Cryst. (1998), B54, 782-789.

[2] Glazer A. M. "*The classification of tilted octahedra in perovskites*" Acta Cryst. (1972), B28, 3384- 3392.

[3] Wu M. K., Ashburn J. R.,Torng C. J., Hor P. H., Meng R. L., Gao L., Huang Z. J., Wang Y. Q., and Chu C. W. "*Superconductivity at 93 K in a new mixed-phase Y-Ba-Cu-O compound system at ambient pressure*" Phys. Rev. Lett. (1987), 58, 908.

[4] Pickett W. E. and Singh D. J "*Electronic structure and half-metallic transport in the $La_{1-x}Ca_xMnO_3$ system*" Phys. Rev. B (1996) 53, 1146.

[5] Li M., Pietrowski MJ., De Souza RA., Zhang H., Reaney IM., Cook SN., "*A family of oxide ion conductors based on the ferroelectric perovskite $Na_{0.5}Bi_{0.5}TiO_3$.*" Nat. Mater. (2014), 13, 31.

[6] Schiffer P., Ramirez A. P., Bao W., and Cheong S-W. "*Low Temperature Magnetoresistance and the Magnetic Phase Diagram of $La_{1-x}Ca_xMnO_3$*" Phys. Rev. Lett. (1995), 75, 3336.

[7] Wiebe C. R., Greedan J. E., Kyriakou P. P., Luke G. M., Gardner J. S., Fukaya A., Gat-Malureanu I. M., Russo P. L., Savici A. T., and Uemura Y. J. "*Frustration-driven spin freezing in the S=12 fcc perovskite Sr_2MgReO_6*" Phys. Rev. B (2003) 68, 134410.

[8] Bhalla A. S., Guo R., Roy R. "*The perovskite structure – a review of its role in ceramic science and technology*" R. Mater Res Innov (2000),4, 3.

[9] Cheong S.W. and Mostovoy M. "*Multiferroics: a magnetic twist for ferroelectricity*" Nat. Mater. (2007), 6, 13.

[10] Anderson M. T. and Poeppelmeier K. R. "*Lanthanum copper tin oxide (La_2CuSnO_6): a new perovskite-related compound with an unusual arrangement of B cations*" Chem. Mater. (1991), 3, 476–482.

[11] Woodward P. M., Cox D. E. , Vogt T., Rao C. N. R. and Cheetham A. K. "*Effect of Compositional Fluctuations on the Phase Transitions in* $(Nd_{1/2}Sr_{1/2})MnO_3$" Chem. Mater. (1999), 11, 3528–3538.

[12] Vasala S. and Karppinen M. "$A_2BB'O_6$ *perovskites: A review*" Progress in Solid State Chemistry (2014), doi:10.1016/j.progsolidstchem.2014.08.001.

[13] Howard C. J., Kennedy B. J. and Woodward P. M. "*Ordered double perovskites - a group-theoretical analysis*" Acta Cryst. (2003). B59, 463-471.

[14] Barnes P. W., Lufaso M. W. and Woodward P. M. "*Structure determination of* $A_2M^{3+}TaO_6$ *and* $A_2M^{3+}NbO_6$ *ordered perovskites: octahedral tilting and pseudosymmetry*" Acta Cryst. (2006), B62, 384-396.

[15] Gateshki M., Igartua J. M. and Hernández-Bocanegra E. "*X-ray powder diffraction results for the phase transitions in* Sr_2MWO_6 *(M = Ni, Zn, Co, Cu) double perovskite oxides*" J. Phys.: Condens. Matter (2003), 15, 6199.

[16] Ortega-San Martin L., Chapman J. P., Lezama L., Saiz Garitaonandia J. J., Sànchez Marcos J., Rodrıguez-Fernandez J., Arriortua M. and Rojo T. "*Spin-glass behaviour in the double perovskite ''*Sr_2FeTeO_6*'' due to mis-site disorder and cation vacancy formation*" J. Mater. Chem. (2006),16, 66-76.

[17] Fu W.T., Gotz R.J. and IJdo D.J.W. "*On the symmetry and crystal structures of* Ba_2LaIrO_6*"* J. Solid State Chem. (2010), 183, 419.

[18] Saines P. J., Spencer J. R., Kennedy B. J. and Avdeev M. "*Structures and crystal chemistry of the double perovskites* $Ba_2LnB'O_6$ *(Ln=lanthanide* $B'=Nb^{5+}$ *and* Ta^{5+}*): Part I. Investigation of* Ba_2LnTaO_6 *using synchrotron X-ray and neutron powder diffraction*" J Solid State Chem. (2007), 180, 2991.

[19] Kobayashi K-I. , Kimura T. , Sawada H., Terakura K. and Tokura Y. "*Room-temperature magnetoresistance in an oxide material with an ordered double-perovskite structure*" Nature (1998), 395, 677.

[20] Sarma D. D., Mahadevan P., Saha-Dasgupta T., Ray S. and Kumar A. "*Electronic Structure of* Sr_2FeMoO_6" Phys. Rev. Lett. (2000), 85, 2549.

[21] Tomioka Y., Okuda T., Okimoto Y., Kumai R., Kobayashi K-I. and Tokura Y. "*Magnetic and electronic properties of a single crystal of ordered double perovskite Sr_2FeMoO_6*" Phys Rev B (2000), 61, 422.

[22] Yan-Qing T., Meng Y. and Yong-Mei H. "*Structure and colossal dielectric permittivity of Ca_2TiCrO_6 ceramics*" J Phys D Appl Phys (2013), 46, 015303.

[23] Yang W.Z., Mao M.M., Liu X.Q. and Chen X.M. "*Structure and dielectric relaxation of double-perovskite La_2CuTiO_6 ceramics*" J Appl Phys (2010), 107, 124102.

[24] Kim K. and Lee S. "*Integration of lead zirconium titanate thin films for high density ferroelectric random access memory*" J. Appl. Phys. (2006), 100, 051604.

[25] Baldinozzi, G., Calvarin, A., Sciau, Ph., Grebille, D., Suard, E. "*Neutron Rietveld refinement of the incommensurate phase of the ordered perovskite Pb_2CoWO_6*" Acta Cryst. (2000), B56, 570-576.

[26] Larrégola, S. A., Alonso, J. A., Sheptyakov, D., Alguerò, M., Muñoz, A., Pomjakushin, V., Pedregosa, J. C. "*High-Temperature Behavior and Polymorphism in Novel Members of the Perovskite Family Pb_2LnSbO_6 (Ln = Ho, Er, Yb, Lu)*" Inorg. Chem. (2011), 50, 5545-5557.

[27] Ivanov, S. A., Nordblad, P., Mathieu, R., Tellgren R., Ritter C. "*Structural and magnetic properties of the ordered perovskite Pb_2CoTeO_6*" Dalton Trans. (2010), 39, 11136–11148.

[28] Blasco, J., Merino, R.I., García, J., Sánchez, M.C. "*Properties and phase transition of the ordered perovskite Pb_2MnWO_6*" J. Phys.: Condens. Matter (2006), 18, 2261-2271.

[29] Ivanov, S.A., Eriksson, S. G., Tellgren, R. H. and Rundlo, R. "*Neutron powder diffraction study of the magnetoelectric relaxor $Pb(Fe_{2/3}W_{1/3})O_3$*" Mater. Res. Bull. (2004), 39, 2317–2328.

[30] Malibert C, Dkhil B, Kiat JM, Durand D, Berar J-F and Spasojevic-de Bire A. "*Order and disorder in the relaxor ferroelectric perovskite $Pb(Sc_{1/2}Nb_{1/2})O_3$*

(PSN): comparison with simple perovskites $BaTiO_3$ and $PbTiO_3$" J Phys Condens Matter 1997, 9, 7485.

[31] Perrin C., Menguy N., Bidault O., Zahra C.Y., Zahra A-M., Caranoni C, Hilczer B. and Stepanov A. "*Influence of B-site chemical ordering on the dielectric response of the $Pb(Sc_{1/2}Nb_{1/2})O_3$ relaxor*" J. Phys. Condens. Matter (2001), 13, 10231.

[32] Azad A.K., Eriksson S.-G., Eriksen J. and Rundlof H. "*Magnetic ordering of Fe in $Sr_{2-x}Ba_xFeWO_6$ (x=0.0, 0.33, 0.67, 1.00) studied by neutron powder diffraction*" Journal of Magn. Magn. Materials (2004), 272, 771–773.

[33] Dass R. I. and Goodenough J. B. "*Multiple magnetic phases of La_2CoMnO_6*" Phys Rev B (2003), 67, 014401.

[34] Ritter C., Ibarra M R, Morellon L, Blasco J, Garcìa J. and De Teresa J. M. *"Structural and magnetic properties of double perovskites $AA'FeMoO_6$ (AA'= Ba_2, BaSr, Sr_2 and Ca_2)"* J. Phys.: Condens. Matter (2000), 12, 8295–8308.

[35] Coomer FC and Cussen EJ. "*Structural and magnetic properties of Ba_2LuMoO_6: a valence bond glass*" J Phys Condens Matter (2013), 25,082202.

[36] Yamashita Y. and Ueda K. "*Spin-Driven Jahn-Teller distortion in a pyrochlore system*" Phys. Rev. Lett. (2000) 85,4960-4963.

[37] J. B. Goodenough, "*Theory of the Role of Covalence in the Perovskite-Type Manganites [La, M(II)]MnO_3*" Phys. Rev. (1955), 100, 564.

[38] Kanamori J. "*Superexchange interaction and symmetry properties of electron orbitals*" J. Phys. Chem. Solids (1959), 10, 87.

[39] Raevski P., Kubrin S. P., Raevskaya S. I., Titov V. V., Sarychev D. A., Malitskaya M. A., Zakharchenko I. N., and Prosandeev S. A. "*Experimental evidence of the crucial role of nonmagnetic Pb cations in the enhancement of the Néel temperature in perovskite $Pb_{1-x}Ba_xFe_{1/2}Nb_{1/2}O_3$.*" Phys. Rev. B (2009)80, 024108.

[40] Schmid H. "*Multi-ferroic magnetoelectrics*" Ferroelectrics (1994), 162, 317

[41] Gajek M,, Bibes M., Fusil S., Bouzehouane K., Fontcuberta J., Barthélémy A. and Fert A.“*Tunnel junctions with multiferroic barriers*” Nature Materials (2007), 6, 296 – 302.

[42] Yang F., Tang M. H., Ye Z. , Zhou Y. C., Zheng X. J., Tang J. X., Zhang J. J., and He J. “*Eight logic states of tunneling magnetoelectroresistance in multiferroic tunnel junctions*” J. Appl. Phys. (2007), 102, 044504.

[43] Kimura T., Goto T., Shintani H., Ishizaka K., Arima T. and Tokura Y. “*Magnetic control of ferroelectric polarization*” Nature (2003) 426, 55-58.

[44] ISI web of science http://apps.webofknowledge.com

[45] Hill, N.A. “*Why Are There so Few Magnetic Ferroelectrics?”* J. Phys. Chem. B 2000, 104, 6694-6709.

[46] Catalan G. and Scott J.F. “*Physics and Applications of Bismuth Ferrite*” Adv. Mater. (2009), 21, 2463–2485.

[47] Lorenz B., Wang Y. and Chu C. W. *“Ferroelectricity in perovskite $HoMnO_3$ and $YMnO_3$”* Phys. Rev. B (2007) 76, 104405.

[48] Sergienko I. A., Sen C. and Dagotto E. *“Ferroelectricity in the Magnetic E-Phase of Orthorhombic Perovskites”* Phys. Rev. Lett. (2006) 97, 227204.

[49] Lee N., Choi Y. J., Ramazanoglu M., Ratcliff II W., Kiryukhin V. and Cheong S.-W. *“Mechanism of exchange striction of ferroelectricity in multiferroic orthorhombic $HoMnO_3$ single crystals”* Phys. Rev. B (2011), 84, 020101(R).

[50] Radaelli P.G. and Chapon L.C. *“A neutron diffraction study of RMn_2O_5 multiferroics”* J. Phys.: Condens. Matter (2008), 20, 434213.

[51] Noda Y., Kimura H., Fukunaga M., Kobayashi S., Kagomiya I. and Kohn K. *“Magnetic and ferroelectric properties of multiferroic RMn_2O_5”* J. Phys.: Condens. Matter (2008), 20, 434206.

[52] Hur N., Park S., Sharma P. A., Ahn J. S., Guha S. and Cheong S-W. *“Electric polarization reversal and memory in a multiferroic material induced by magnetic fields”* Nature (2004), 429, 392.

[53] Hur N., Park S., Sharma P. A., Guha S., and Cheong S-W. *"Colossal Magnetodielectric Effects in $DyMn_2O_5$"* Phys. Rev. Lett. (2004) 93, 107207.

[54] Arkenbout A. H., Palstra T. T. M., Siegrist T., and Kimura T. "*Ferroelectricity in the cycloidal spiral magnetic phase of $MnWO_4$*" Phys. Rev. B (2006), 74, 184431.

[55] Kimura T., Sekio Y., Nakamura H., Siegrist T. and A. Ramirez P. "*Cupric oxide as an induced-multiferroic with high-T_C*" Nature Materials (2008), 7, 291 – 294.

3 Magnetic symmetry and superspace approach

3.1 Introduction

As already pointed out in the previous chapter, the knowledge of the magnetic point group has a fundamental importance in the study of multiferroic materials, since it constrains the tensor properties of the system. In fact, the Neumann principle asserts that the symmetry of a physical property cannot be lower than the one of the point group of the crystal. This principle, applied to the magneto-electric multiferroics, defines the breaking of both time and spatial inversion symmetry as the symmetry requirements for the existence of such materials.

Hereafter, the definition of the time-inversion symmetry and its combination with the other symmetry operators leading to the definition of the magnetic space groups will be illustrated. The last two sections will describe the generalization of the coloured symmetry to the superspace formalism.

3.2 Magnetic moment and symmetry operations

The magnetism in transition metal (TM) oxides is due to the un-paired electrons in the *d*-shells. These electrons generate a magnetic moment on the TM site and, in first approximation, we can consider the magnetic moment $\boldsymbol{\mu}$ as generated from spiral electronic current in the orbitals. In this approximation the magnetic moment is given by $\vec{\mu} = 1/2\vec{r} \times \vec{i}$, where $\boldsymbol{r}$ is the radius of the spiral and $\boldsymbol{i}$ is the current. In this way the magnetic moment is defined as a classical axial vector or pseudo-vector.

To understand how the symmetry acts on an axial vector we have first to divide the classical symmetry operators into two classes: the proper and improper operators. The first are operators, which do not change the handiness of an object, whereas the latter are operators, like mirror or improper rotations, which invert the handiness. The action of a proper symmetry operation on an axial vector is the same performed on a polar vector, as well as on any scalar or pseudo-scalar quantity. For example, a twofold axis does not invert a polar vector and do the same on an axial one (figure 3-1). On the contrary an improper twofold axis (i.e. a mirror) acts differently, adding the reversal of the axial vector direction. In fact, in figure 3-1, the mirror transforms in clockwise the anticlockwise current loop that generates the magnetic moment (axial vector), changing of the spin sign.

This can be mathematically described by taking into account the parity of the operator. Let us consider the point symmetry operator described by the *R* matrix; the action of this operator on a polar vector or scalar quantity $\boldsymbol{u}$ is given by:

$$\vec{u}_j = R\vec{u}_i \qquad (1$$

For an axial vector $\boldsymbol{\mu}$, the action of the symmetry operator R depends on its parity (i.e. on the sign of the determinant of the R matrix), being:

$$\vec{\mu}_j = \det[R] R \vec{\mu}_i \qquad (2$$

This lead to the reversal of the vector direction for det[R]= -1, i.e. if R is an improper symmetry operator.

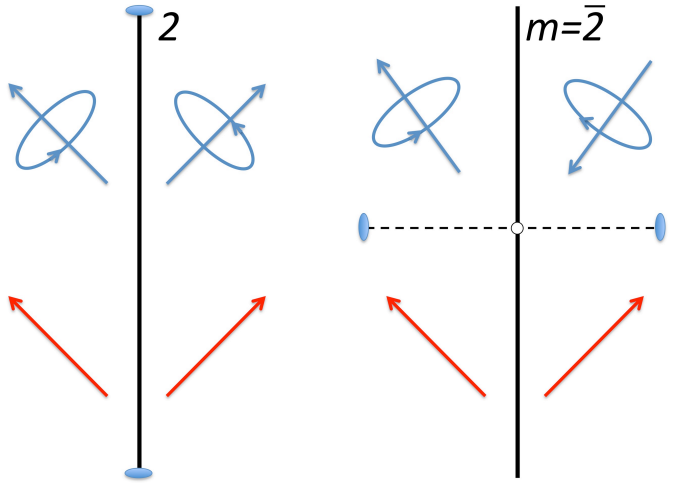

Figure 3-1 Left) effect of a proper rotation on an axial (blue) and polar vector (red). Right) action of an improper rotation on the same elements. Note the direction of the current in the coil that is reversed by the action of the improper rotation.

When space groups describing the symmetry of magnetic structures are concerned, the existence of a group of symmetry that leaves invariant a magnetic structure requires an additional symmetry operator that inverts the sign of an axial vector. This new symmetry operation, that can be considered an anti-identity operation, is generally indicated as 1' and it is worthy to underline that it acts only on axial vectors, whereas polar vectors as well as scalar or pseudo-

scalar objects, are invariant upon its action. This operator is necessary, in combination with the crystallographic ones, to describe in a comprehensive manner all the symmetry operations present in a periodic distribution of axial vector quantities.

In the case of the magnetic moment, the action of 1' is the reversal of the spin sign by inverting the direction of the current loop. For this reason, the 1' operator is generally called “spin reversal” or “time reversal” operator. The latter definition takes into account that the reversal of the time direction induces a change of the current loop, producing the spin inversion.

A space group in which the 1' operator appears by itself is known as “paramagnetic” or grey space group, since in this condition magnetic ordering is forbidden. In fact, if we consider a magnetic moment vector $\boldsymbol{\mu}$ located on an atom, 1' will generate $-\boldsymbol{\mu}$ at the same location, so that there can not be a net magnetic moment.

To obtain magnetic symmetry operations, 1' must be combined with the classical symmetry operators. The combination is indicated in the formalism $\{R, \partial|\mathbf{t}\}$, in which R is the rotational (point) part of the operator, $\partial = \pm 1$ indicate the time inversion sign and $\mathbf{t}$ is the translation. The symmetry operator $\{R, \partial|\mathbf{t}\}$ transforms an atom in position $\boldsymbol{r}_i$ with moment $\boldsymbol{m}_i$ to one in $\boldsymbol{r}_j$ with moment $\boldsymbol{m}_j$ by the relations:

$$\begin{aligned} \{R,\delta\,|\,\vec{t}\,\}\vec{r}_i &= R\vec{r}_i + \vec{t} = \vec{r}_j \\ \{R,\delta\,|\,\vec{t}\,\}\vec{m}_i &= \delta\det[R]R\vec{m}_i = \vec{m}_j \end{aligned} \qquad (3$$

Usually a symmetry element that includes the time inversion, i.e. an anti-symmetry element, is indicated with a primed symbol. For example the *m'* symbol used in figure 3-2 indicates the combination of the mirror plane with the time inversion operators.

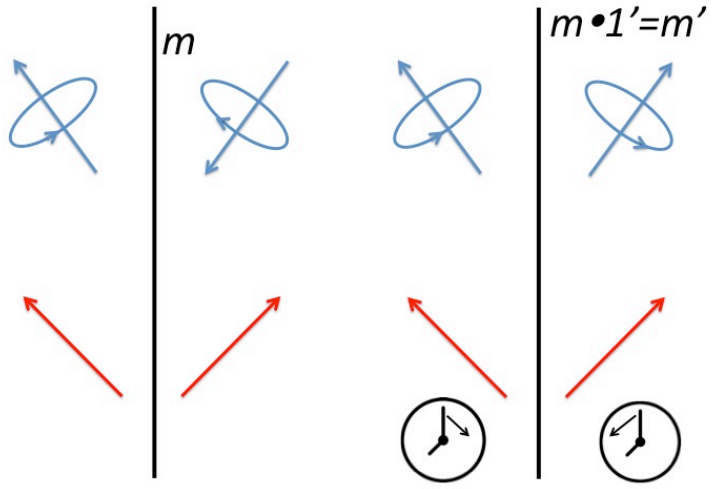

Figure 3-2 Left) Action of a mirror plane on an axial (blue) and a polar vector (red). Right) action of a primed mirror plane of the same objects. Note that the time inversion symmetry changes the direction of the time (indicates from the two clocks) and change the direction of the current loop respect to the un-primed operator. For the polar vector (red) the primed and un-primed operators have the same effect.

3.3 Magnetic (Shubnikov) groups

After defining the magnetic symmetry operations, it is possible to construct the magnetic space groups, called Shubnikov groups in honour of Alexey Vasilyevich Shubnikov that first studied the anti-symmetry and formulated the two colour space groups,[1] for which 1' represents the colour inversion. The fundamental rule to construct the magnetic space groups is that the product of two primed operators must give an un-primed one, for example 2'•2'=1. By applying this rule, all the magnetic space groups can be generated. By considering a classical space group **G** and defining **I** a group containing the operations {1,1'}, all the magnetic space groups **P** derived from **G** are subgroups of the direct product **G⊗I.** First the **G** group is itself a magnetic space group, called Fedorov group, in which every element is un-primed and all the symmetry

operations act on the magnetic moment; the **G+G•1'** group is the so called grey group and is the paramagnetic space group of **G.** The systematic procedure to obtain the other magnetic space groups is a direct consequence of the fundamental rule described above. Let us define **H** as a subgroup of order 2 of **G**. The magnetic space group **P** can be obtained by considering **H** as the un-primed elements and by priming all the remaining **(G-H)** elements; the resulting space groups are **P=H+(G-H)•1'.** This procedure can be applied to all kind of symmetry groups: point groups, space groups and even translation groups. In this way one can construct all the possible two colour groups derived from **G,** but not all of these can allow magnetic order since the combination of primed and un-primed elements might determine the vanishing of the magnetization. By systematically applying this to the 230 space groups, one can obtain all the two colour space groups describing magnetic structures with propagation vector corresponding to the **Γ** point of the Brillouin zone (propagation vector κ=(0 0 0)). As previously mentioned the method to construct the two colour groups can be applied to the translation groups to obtain the magnetic lattices. Let us denote with **L** the group of the lattice translations constructed by the lattice generators plus, if present, the centring operations. By taking into account the subgroups **H** of order 2 of **L** it is possible to define the magnetic lattice $\mathbf{P_M=H+(L-H)\ \bullet 1'}$.

Following the procedure described above it is possible to derive, starting from **G,** all the coloured space groups **P** that could be divided into 4 types:

- Type I: **P=G** (Fedorov Group)
- Type II: **P=G+G•1'** (grey group or paramagnetic group)
- Type III: **P=G+(G-H)•1'** where **H** is an equi-translational subgroups of order 2 of **G**. In this type of groups, half of the symmetry elements contains the time inversion symmetry and are indicated in the space group notation with a primed symbol. The lattice translations do not contain the time inversion symmetry. These types of magnetic groups describe the magnetic structure related to the Γ point of the Brillouin zone.

- Type IV: **P=G+(G-H)•1'** where **H** is en equi-class subgroup of order 2 of **G**. In these magnetic space groups, half of the lattice transitions are combined with the time inversion symmetry. This implies that the magnetic point group of a type IV group is actually a grey group. Type IV groups describe the magnetic structure with propagation vector related to special points of the Brillouin zone. The notations of the magnetic lattice in the BSN setting[2] are reported in table 3-1.

Table 3-1 Lattice type notation in the BNS[2] setting. In the symbol the first capital letter indicates the type of the crystal lattice (primitive or centred), whereas the subscript letter indicates the primed translations: lowercase letters indicate a primed direction, capital latters indicate primed centred translation. The BNS lattice, if formed by the translation ***t*** of the **H** subgroups of **G**, consequently contains the primed operations as a fractional translation of ***t***; it follows that the magnetic unit cell is larger than the nuclear one. In the table, for each BNS lattice symbol, the primed fractional translation respect to the magnetic unit cell is reported.

Lattice symbol	Primed translation
$\mathbf{P_S}$	(0,0,1/2) triclinic only
$\mathbf{P_a}$	(1/2,0,0)
$\mathbf{P_b}$	(0,1/2,0)
$\mathbf{P_c}$	(0,0,1/2)
$\mathbf{P_A}$	(0,1/2,1/2)
$\mathbf{P_B}$	(1/2,0,1/2)
$\mathbf{P_C}$	(1/2,1/2,0)
$\mathbf{P_I}$	(1/2,1/2,1/2)
$\mathbf{A_a}$	(1/2,0,0)
$\mathbf{A_b}$	(0,1/2,0)
$\mathbf{A_B}$	(1/2,0,1/2)
$\mathbf{B_b}$	(0,1/2,0)
$\mathbf{B_a}$	(1/2,0,0)
$\mathbf{B_A}$	(0,1/2,1/2)
$\mathbf{C_c}$	(0,0,1/2)
$\mathbf{C_a}$	(1/2,0,0)
$\mathbf{C_A}$	(0,1/2,1/2)
$\mathbf{F_S}$	(1/2,1/2,1/2)
$\mathbf{I_a}$	(1/2,0,0)
$\mathbf{I_b}$	(0,1/2,0)
$\mathbf{I_c}$	(0,0,1/2)
$\mathbf{R_I}$	(0,0,1/2)

Daniel B. Litvin derived all the four type of magnetic space groups and edited the magnetic crystallographic tables.[6] These tables report symmetry elements, Wyckoff positions and symmetry permitted components of the magnetization for each atomic position.

3.4 Space groups determination and magnetic structure analysis

The experimental determination of the magnetic structure is performed by the analysis of neutron diffraction data. Since neutrons are elementary particles possessing spin ½, they can interact with the magnetic moments present in the system principally via dipole-dipole interactions. The diffracted intensity can be calculated similarly to X-ray recalling that the magnetic density is a vector quantity.

Defining $\boldsymbol{\rho}_{\mathrm{mag}}$ the unit cell magnetic density generated by the unpaired electrons, the structure factor for un-polarized neutrons of the **H** reflection can be obtained by the Fourier transform of ρ_{mag}

$$F(\vec{H}) = p\int \rho_{mag}(r)\exp[2\pi i\vec{H}\cdot\vec{r}]dr \qquad (4$$

where $p = r_e\gamma/2$ (r_e is the classical electron radii and γ magnetic moment of the neutron) is the conversion factor of the magnetic density from Bohr magnetons to scattering lengths unit. Because of the atomicity of the crystal structure, it is possible to substitute the magnetic density of the unit cell with a summation over all the magnetic atoms in the cell. The Fourier transform has now the form:

$$F(\vec{H}) = p\int \sum_{i}^{N} \rho_i(\vec{r} - \vec{r}_i)\exp[2\pi i\vec{H}\cdot(\vec{r} - \vec{r}_i)]dr$$

$$F(\vec{H}) = p\sum_{i}^{N} \int \rho_i(R_i)\exp[2\pi i\vec{H}\cdot(\vec{R}_i + \vec{r}_i)]dR_i \qquad (5$$

$$F(\vec{H}) = p\sum_{i}^{N} \exp[2\pi i\vec{H}\cdot\vec{r}_i]\int \rho_i(R_i)\exp[2\pi i\vec{H}\cdot\vec{R}_i]dR_i$$

The integral part of the last expression is the non-normalized form factor of the i-th atoms:

$$F(\vec{H}) = p\sum_{i}^{N} (\hat{H}\times\vec{M}_i\times\hat{H}) f_i(\vec{H})\exp[2\pi i\vec{H}\cdot\vec{r}_i]$$

$$F(\vec{H}) = p\sum_{i}^{N} \vec{M}_{i\perp} f_i(\vec{H})\exp[2\pi i\vec{H}\cdot\vec{r}_i] \qquad (6$$

where $\vec{M}_{i\perp}$ is the magnetization component normal to the scattering vector ***H***. The fact that the neutron magnetic diffraction allows to observe only the magnetization normal to the scattering vector is a direct consequence of the vector character of the interactions and makes possible the determination of the direction of the spins with respect to the crystal lattice in a neutron diffraction experiment. By using equation 6, the intensity of the magnetic reflections can be calculated by introducing all the needed corrections, like thermal factor, Lorenz factor etc. The nuclear and magnetic intensities are additive and of the same order of magnitude.

Obviously, the magnetic diffraction intensity appears only for ordered structures and the 2θ positions of magnetic reflections and the related propagation vector κ of the magnetic structure are usually found by comparing the diffraction patterns recorded below and above a magnetic transition. The integrated intensity of the reflections can give us the relative orientation and magnitude of the magnetic moment in the structure, but in order to take

advantage of the symmetry constrains, the magnetic space group of the structure has to be determined.

The magnetic space group of a material is strictly related to the nuclear space groups **G** and to the propagation vector. By applying the procedure described earlier, a list of possible magnetic space groups can be obtained. Another, more formal way, to introduce the time inversion symmetry and to obtain the possible magnetic space groups related to the parent space group **G**, is the use of the representation theory[3] and in particular the so called isotropy subgroup.[4] When a system undergoes a symmetry-reducing transition (as the one induced by the time-symmetry breaking) not all the symmetry elements of the parent high symmetry phase are retained; the symmetry elements that are retained during the transition form the so called isotropy subgroup and will became the space groups of the low simmetry structure. For a given κ-point of the first Brillouin zone the related isotropy subgroups are finite and can be determined by the application of the representation theory. A very useful tool to determine the isotropy subgroup is the ISODISTOR software.[5]

Once that a list of possible magnetic space groups has been obtained, the magnetic structure solution must be searched in all of them to find the best model. Fortunately, the number of possible groups can be reduced by the observation of magnetic systematic absences. Like in case of nuclear space groups, the structure factor of symmetry related reflections must be the same. If $\{R,\partial|\mathbf{t}\}$ is the symmetry operator that relate **H** with *R***H,** then the relation between the structure factor is given by:

$$F(\vec{H}) = \delta \det[R] \exp(2\pi i \vec{H} \cdot \vec{t}) F[R\vec{H}] \qquad (7$$

Being **H**=*R***H** one obtains a relation similar to the one for the nuclear scattering, except for the axial nature of **F(H)**. The application of the equation 7 to all the symmetry operators of the magnetic space group gives the magnetic systematic absences. For example, whatever paramagnetic space group **G+G•1'**

is considered, the presence of the {1'| 0 0 0} operator gives, from equation 7, **F(H)=−F(H)** that imply a zero intensity (systematic absence) of all the magnetic reflections. Unlike the systematic absences in nuclear scattering, that are exclusively produced by symmetry elements containing non-integer translations (lattice centring, glide planes and screw axis), in the magnetic symmetry some point elements (improper rotation axes) can generate absences due to the axial vector nature of the magnetic moment. For example, a mirror normal to the x direction in the real space, relate the (h 0 0) reflections to the (-h 0 0) ones. By applying the equation 7 to this family of reflections, related by the $\{m_x|0\ 0\ 0\}$ symmetry operation, one obtains the relation F(h 0 0)= −F(h 0 0), being δ= 1 and det[*R*]=−1. This indicates the systematic absence of (h 0 0) reflections for any h value.

Moreover, since the neutron scattering in sensible only to the magnetization component normal to the scattering vector, some reflections may have zero intensity because of the direction of the magnetization in the structure and this can help to find the correct magnetic model by suggesting additional constrain to the magnetization components. The list of the systematic absences for each magnetic space group and the symmetry-forced form factor, indicating which component of the magnetization contributes to each family of reflections, can be found on the Bilbao crystallographic server[7-9] and in particular by the MAGNEXT[10] software. In order to calculate the influence of the space group on the structure factor, the MAGNEXT software[10] use the group theory and the projector operators obtaining a sort of symmetry adapted structure factors. Once that the correct magnetic space group has been determined, the structure refinement could be carried on in the same way as for nuclear structure, namely by refining the magnetic parameters of the asymmetric unit, being the whole structure obtained by applying the symmetry operators of the space group.

3.5 Superspace formalism

Crystals are defined as solid materials in which atoms are arranged according to a periodic space lattice. The long-range order is due to a perfect 3D translational symmetry, and the interaction with a radiation with wavelength in the order of the lattice distances, give rise to a diffraction pattern. In some cases, the perfect 3D lattice periodicity is lost, due to modulation of atomic positions, occupancy factors or whatever structural parameter; these systems are called aperiodic crystals because of the lack of the perfect translational periodicity. Some examples are the incommensurate and commensurate modulated structures, composite crystals and quasi-crystals. In this thesis, only the former will be analysed.

Brouns, Visser and de Wolff reported the first example of modulated crystal in 1964;[11] the authors observed that the γ-Na_2CO_3 single crystal diffraction pattern consists of two series of reflections, of which the first can be indexed with a monoclinic structure that leaves un-indexed the second ones. The indexing the entire diffraction pattern was possible only by using three irrational indices or a four-integer indexing scheme given by:

$$\begin{aligned} H &= ha^* + kb^* + lc^* + mq^* \\ q^* &= \alpha a^* + \beta b^* + \gamma c^* \end{aligned} \qquad (8$$

where $\boldsymbol{q}$ is a modulation vector defined as a linear combination of the reciprocal lattice vectors. In this way all the diffraction pattern is indexed by four indices (h k l m).

The physical evidence of diffraction in similar cases indicates that the lattice periodicity is maintained even in aperiodic crystal. This periodicity is, in fact, preserved if a higher dimensional space is taken into account in which $\boldsymbol{a}^*$ $\boldsymbol{b}^*$ $\boldsymbol{c}^*$ and $\boldsymbol{q}^*$ define a reciprocal lattice.

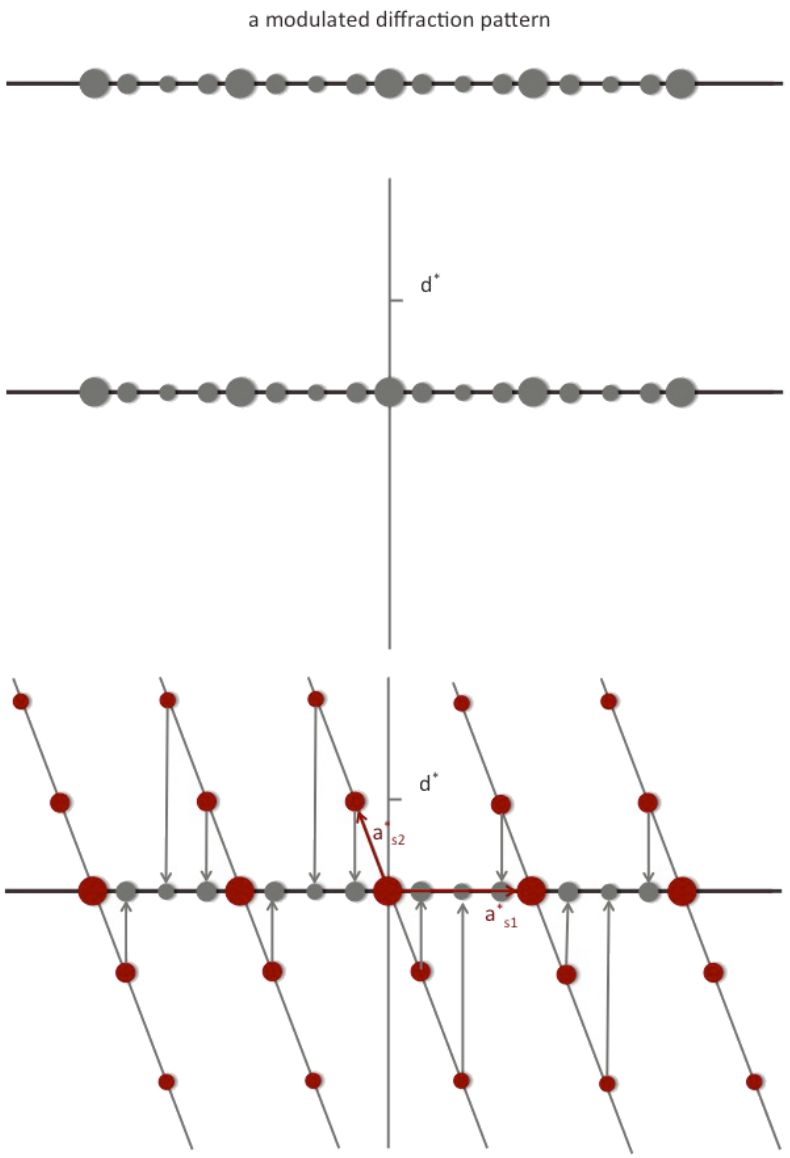

Figure 3-3 Geometrical construction of a (1+1)D reciprocal lattice starting from a one-dimensional modulated structure (see text for details).

The mathematical formalism to describe the diffraction from modulated and composite crystals is called superspace and was formulated for the first time

by Janner and Janssen[12-13-15] and by de Wolf[14-15] in the '80. The formalism is based on the definition of a (3+n)D space in which the additional n-dimensions describe the modulation functions. In the aim of this thesis only 1-dimensional modulated structure will be take into account. The (3+1)D reciprocal space is constructed by adding a 4th dimension $\boldsymbol{d}^*$ perpendicular to the 3D space. A simple example of the superspace construction is given in figure 3-3 where, starting from a 1D row of reflections with incommensurate modulation satellites, the (1+1)D reciprocal space is constructed by introducing a $\boldsymbol{d}^*$ direction perpendicular to the 1D space. We can now define a (1+1)D reciprocal lattice by choosing $\boldsymbol{a}^*_{S1}$ and $\boldsymbol{a}^*_{S2}$ and we can reconstruct the experimental pattern as the projection of the (1+1)D reciprocal lattice on the 1D space. The generalization of this procedure in three dimensions allow to construct a (3+1)D reciprocal space of an incommensurate crystal, whose experimental diffraction pattern is the projection of the (3+1)D reciprocal lattice on the real 3D space.

In the superspace formalism a modulated structure is described by an average 3D structure (the basic or fundamental structure) characterized by a standard crystallographic space group and defined by the (h k l 0) family of reflections, coupled with a modulation function $\boldsymbol{u}^{\mu}(x_4)$ that indicates the deviation of the modulated atomic parameter $\boldsymbol{u}$ (position, occupancy, thermal parameters etc.) from the average value defined in the basic structure. The modulation functions are wave functions characterized from the modulation vector $\boldsymbol{q}$ that determines the direction and periodicity of the modulation. The $\boldsymbol{q}$ vector is defined as a linear combination of the lattice generators of the basic structure: if one of the components of $\boldsymbol{q}$ $(\alpha\ \beta\ \gamma)$ is irrational, the modulation is incommensurate and the perfect 3D periodicity is lost. The argument of the modulation function represents the x_4 fractional coordinate in the (3+1)D space along the fourth axis. The x_4 coordinate of the μ^{th} atoms in $\boldsymbol{x}_{\mu}$ position is given by:

$$x_4 = t + \vec{q} \cdot \vec{x}_{\mu} \qquad (9$$

where t is the choice of the fourth axis origin. The modulation function can have any mathematical form and the unique requirement is the periodicity along the x_4 coordinate:

$$u^{\mu}(x_4) = u^{\mu}(x_4 + 1) \tag{10}$$

This is necessary because otherwise the translational periodicity is lost also in the (3+1)D space, producing in diffraction streaks instead of sharp satellites. Owing to the periodicity of the modulation function, is possible to express it in a Fourier series:

$$u^{\mu}(x_4) = \sum_{n=1}^{\infty} A^n(\mu)\sin(2\pi n x_4) + B^n(\mu)\cos(2\pi n x_4) \tag{11}$$

where the Fourier coefficient $A^n(\mu)$ and $B^n(\mu)$ are the refinable variables of the modulation function. Fortunately, it is not necessary to use all the infinite terms of the Fourier series since the amplitudes decay fast and usually only the first few orders must be taken into account.

After defining the modulation function $\boldsymbol{u}^{\mu}(x_4)$, it is possible to explicit the direct superspace and its relation with the real 3D space. A simple geometrical construction, shown in figure 3-4, allows the visualization of the direct superspace. Let us take a 1D chain of atom and apply a sinusoidal modulation wave to the atom positions. The equivalent direct (1+1)D space is obtained by rotating the sinusoidal wave by 90° degree, using the atom positions as fulcrum. This operation defines a direction perpendicular to the atoms chain and the period of the modulation function define the periodicity $\boldsymbol{d}$ along this direction. Now is possible to define a (1+1)D lattice by choosing as generator $\boldsymbol{a}_{s1}$ and $\boldsymbol{a}_{s2}$, that define also a unit cell in the super-space. The displacement of each atom in the chain can be reported in the first unit cell by an integer number of

translation of the two lattice generators. This implies that all the information to reconstruct the whole modulated crystal is present in the defined unit cell.

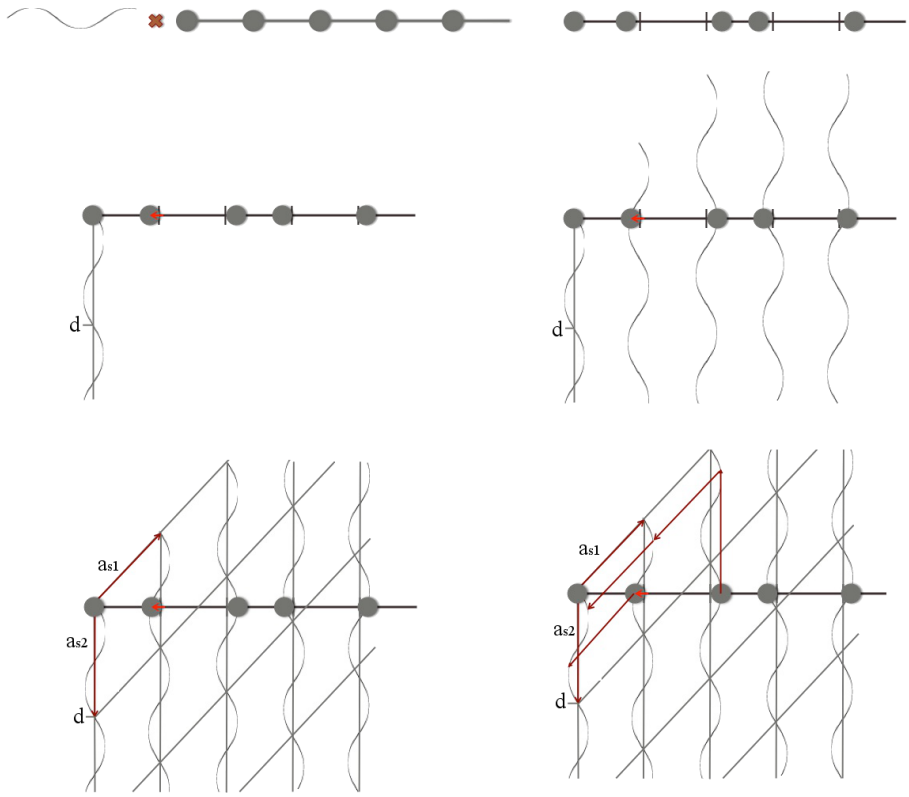

Figure 3-3 Geometrical construction of the direct superspace starting from a linear modulated chain of atoms (see text for details).

In particular is evident from the construction that the real space is obtained by a section of the direct super-space perpendicular to the fourth axis; any section perpendicular to this is a 3D space and the position of the section is defined by the value of the *t* parameter defined in equation 9. In case of an incommensurate structure any *t* section gives equivalent structure since all the point of the modulation function are present in the crystal. This is not the case for a commensurate structure, where the choice of the *t* section is fundamental

and the topic will be discussed in detail later, on the basis of experimental data. Since in incommensurate structures each value of the modulation function $u^{\mu}(x_4)$ is present in the crystal, the use of the so call *t*-plot is convenient to evaluate the evolution of the modulated parameters within the structure. The t-plot is the graphical representation of the modulation function values as function of x_4 or *t*. Owing to the periodicity of the modulation function along this direction, all the information is contained in the range $0 \leq t \leq 1$.

In the case of a commensurate modulated structure always exist an integer number N_s for which $\vec{H}_0 = N_s\vec{q}$ where $\boldsymbol{H_0}$ is a reciprocal lattice vector of the basic structure. In this case, the components of the modulation vector are rational numbers and is always possible to construct an N_s-fold superstructure that allows to index all the reflections with three integer numbers. Generally in these cases is hard to analyse the superstructure with classical crystallographic methods because of the strong increase of free parameters and of the correlations among them, in particular if the variations from the average structure are tiny, reducing the intensity of the satellites and consequently the already low number of estimations. The superspace formalism reduces the refinable parameters and the correlations. The main difference with the incommensurate case is that only discrete values of the modulation function are present in the crystal even if all the $\boldsymbol{u}^{\mu}$ function values are permitted. In particular these values are exactly N_s and are related by:

$$x_4^{\mu} = t_0 + \frac{l}{N_s} + \vec{q}\cdot\vec{x}_0^{\mu} \qquad l = 1,2,...,N_s \tag{12}$$

where $\vec{x}_0^{\mu}$ is the position of the $\boldsymbol{\mu}^{th}$ atom in the average structure, and $\boldsymbol{t_0}$ is the origin choice for the *t*-section. This relation implies that the positions along the fourth axis of the μ^{th} atom are finite and equal to N_s. In this conditions the choice of the initial phase of the modulation function, the t_0 parameter, changes the modulation values for the atoms in the structure, giving rise to different

space group for the N_s-fold superstructure. To find the correct value of the t_0 parameter represents the main problem for the solution of commensurate structure by the superspace formalism.

As suggested by the observation that the diffraction pattern generated from aperiodic crystals possesses point symmetry similar to that of periodic crystals, the symmetry elements characteristic of the 3D space groups could be generalized in a higher dimensional space. The main reflections, which are indexed on the basis of the lattice generators of the basic cell, must obey to the point group of the basic structure. It follows that the point group of the satellite reflections must be the same. In fact, a point group operator transforms a main reflection in an equivalent main reflection and must do the same on a satellite one. This is a fundamental point and defines that the additional dimension is ancillary respect to the real space, and as consequence no symmetry operator can mix the real space coordinates with the additional ones. In particular the action of R on the modulation vector follows the relation:

$$qR = \varepsilon q + H_R \tag{13}$$

where $\varepsilon = \pm 1$ and $\boldsymbol{H_R}$ is a reciprocal lattice vector that depends on R and is different from zero only if the modulation vector possesses some commensurate coefficient. Now it is possible to define the R_s matrix form of the operator R in the (3+1)D space. This operator transforms the basic structure lattice generators according to:

$$\begin{pmatrix} a' \\ b' \\ c' \end{pmatrix} = R \begin{pmatrix} a \\ b \\ c \end{pmatrix} \tag{14}$$

from equation 13 it is possible to obtain the action of R on the x_4 coordinate. By combining the two equations 13 and 14 one obtain the matrix form of R_s:

$$R_s = \begin{pmatrix} R_{11} & R_{12} & R_{13} & 0 \\ R_{21} & R_{22} & R_{23} & 0 \\ R_{31} & R_{32} & R_{33} & 0 \\ H_x & H_y & H_z & \varepsilon \end{pmatrix} \quad (15$$

where H_x, H_y, H_z are the components of the reciprocal vector $\boldsymbol{H_R}$ defined in 10, and $\varepsilon=\pm1$. This is the matrix form of the **R** point operator in the (3+1)D space. The symmetry element $\{R_s|\mathbf{t}\}$, where **t** is a non-integer translation, operates on the atomic coordinates as follow:

$$\begin{pmatrix} x' \\ y' \\ z' \\ x'_4 \end{pmatrix} = R_s \begin{pmatrix} x \\ y \\ z \\ x_4 \end{pmatrix} + \begin{pmatrix} t_1 \\ t_2 \\ t_3 \\ t_4 \end{pmatrix} \quad (16$$

After defining the symmetry operators, is possible to combine them to construct the superspace symmetry groups. The superspace group symbol is composed by the classical symbol of the 3D space group of the average structure, followed by the permitted components of the modulation vector (in brackets) and by the non-integer values of the translation along the fourth axis. The translations are indicate by a lowercase letter following the coding: s=1/2 t=1/3 q=1/4 and h=1/6. Let us take, for example, the superspace group *Pnma(00γ)0s0;* this indicates that the symmetry space group of the basic structure is *Pnma* and that only the γ component of the modulation vector differs from zero. The generator operators of the superspace group are: $\{m_x|0\ ½\ ½\ 0\}$ (n glide), $\{m_y|\ 0\ 0\ 0\ ½\}$ (mirror plane with a non integer translation along the fourth axis) and $\{m_z|\ ½\ 0\ 0\ 0\}$ (*a* glide); among these only the mirror plane along ***b*** have a non-integer translation along the fourth axis of the (3+1)D space.

The definition of the structure factor in the superspace is analogue to its definition in 3D. In the case of the X-ray diffraction for example is possible to define a generalized electronic density $\boldsymbol{\rho}_s(\boldsymbol{x}_s)$ in the (3+n)D space. This function is periodic in the superspace coordinate $\boldsymbol{x}_s$ and the direct superspace lattice defines the period of $\boldsymbol{\rho}_s(\boldsymbol{x}_s)$. The generalized density has maxima in string that are, in average, perpendicular to real 3D space and the average position represents the atom position in the basic structure. The structure factors are defined as the (3+n)D Fourier transform of the $\boldsymbol{\rho}_s(\boldsymbol{x}_s)$ electron density as for conventional periodic crystals. The experimental intensity of the (*h k l m)* reflection is then the modulus of the structure factor in the (3+n) dimension. It follows that the structure solution and refinement in the superspace take place in a manner that is similar to the one used for classical crystallographic structures. In particular the relation between the direct and reciprocal superspace is governed by the (3+n)D Fourier transform and the main problem for the solution of modulated structures is the phase determination. Since the structure is solved in the (3+n)D space, the real structure is obtained from a section of the generalize electronic density $\boldsymbol{\rho}_s(\boldsymbol{x}_s)$ perpendicular to the n additional dimensions.

In the figure 3-4 all the relations between the 3D and the (3+n)D direct and reciprocal space are schematized. First the experimental diffraction pattern is the projection on the 3D space of the reciprocal (3+n)D lattice of the structure. By operating the inverse (3+n)D Fourier transform on the superspace reciprocal lattice, assuming as known the phase of each reflection, the generalized electronic density is obtained and the (3+n)D structure is solved. The real modulated structure is then obtained by a *t*-section of the generalized electron density perpendicular to the 3D space, taking particular attention in case of commensurate structure.

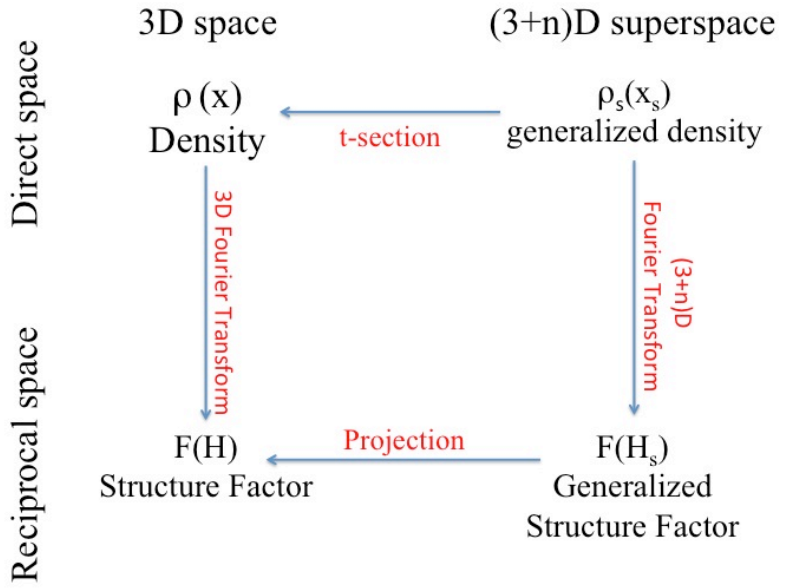

Figure 3-4 Schematic relations between the direct and reciprocal space in 3D and in the superspace.

3.6 Application of magnetic symmetry to the superspace formalism

The magnetic space groups we discussed previously can describe magnetic structures related to special points of the first Brillouin zone. However, from the experimental point of view, magnetic structures are observed whose propagation vectors are related to symmetry lines and planes of the first Brillouin zone. If the propagation vector is commensurate, is always possible to construct a superstructure and work with the coloured space group as described earlier. This methodology presents the advantage of a more simple approach, but also disadvantages, in particular it increases the number of refinable parameters leading in some case to the instability of the refinement. Besides, the neutron magnetic form factor decay fast with the scattering vector**,** owing to the wide spatial distribution of the unpaired electrons, limiting the observable reflections and consequently the ratio between parameters and observed data, in particular

in case of powder diffraction. In these cases, as well as in presence of an incommensurate propagation vector, the application of magnetic symmetry to the superspace formalism can give good results and supplies a useful description of the magnetic structure.

To introduce the "coloured" superspace, let us define the generalized magnetic density of the crystal $\boldsymbol{\rho}_{s,mag}$. In analogy with the modulated crystal it is possible to define it as an average magnetic structure $\boldsymbol{\rho}_{0,mag}$ and a modulation function $\boldsymbol{m}(x_4)$ that describe the deviation of $\boldsymbol{\rho}_{0,mag}$ with x_4. Considering the atomicity of the structure and the periodicity of $\boldsymbol{m}(x_4)$, the generalized magnetic density can be written as:

$$\rho_{s,mag}(\vec{r}) = \sum_{\mu}^{N_{cell}} \left[\rho_{\mu,0}(r - r_\mu) + \sum_{n=1}^{\infty} m_{n,s}^{\mu} \sin(2\pi n\vec{k} \cdot (\vec{r} - \vec{r}_\mu)) + m_{n,c}^{\mu} \cos(2\pi n\vec{k} \cdot (\vec{r} - \vec{r}_\mu)) \right] \quad (17$$

where $\rho_{\mu,0}(r - r_\mu)$ is the average magnetic density of the μ[th] atom in the structure and $m_{n,s}^{\mu}$, $m_{n,c}^{\mu}$ are the Fourier coefficients of the $\boldsymbol{m}(x_4)$ modulation function. By applying the kinematic theory of diffraction to the so defined magnetic density, one can obtain the structure factor for any reflection by means of the Fourier transform:

$$\begin{aligned}
&FT[\rho_{s,mag}(\vec{r})] = \\
&= p\int \sum_{\mu}^{N_{cell}} \left[\rho_{\mu,0}(r - r_\mu) + \sum_{n=1}^{\infty} m_{n,s}^{\mu} \sin(2\pi n\vec{k} \cdot (\vec{r} - \vec{r}_\mu)) + m_{n,c}^{\mu} \cos(2\pi n\vec{k} \cdot (\vec{r} - \vec{r}_\mu)) \right] \exp[2\pi i\vec{H} \cdot \vec{r}]dr = \\
&= p\int \sum_{\mu}^{N_{cell}} \left[\rho_{\mu,0}(\vec{R}_\mu) + \sum_{n=1}^{\infty} m_{n,s}^{\mu} \sin(2\pi n\vec{k} \cdot \vec{R}_\mu) + m_{n,c}^{\mu} \cos(2\pi n\vec{k} \cdot \vec{R}_\mu) \right] \exp[2\pi i\vec{H} \cdot (\vec{R}_\mu + \vec{r}_\mu)]d\vec{R}_\mu = \\
&= p\sum_{\mu}^{N_{cell}} \exp[2\pi i\vec{H} \cdot \vec{r}_\mu] \left[\begin{array}{l} \int \rho_{\mu,0}(\vec{R}_\mu)\exp[2\pi i\vec{H} \cdot \vec{R}_\mu]d\vec{R}_\mu + \\ + \int \sum_{n=1}^{\infty} [m_{n,s}^{\mu} \sin(2\pi n\vec{k} \cdot \vec{R}_\mu) + m_{n,c}^{\mu} \cos(2\pi n\vec{k} \cdot \vec{R}_\mu)]\exp[2\pi i\vec{H} \cdot \vec{R}_\mu]d\vec{R}_\mu \end{array} \right]
\end{aligned} \quad (18$$

The first integral part of the last expression is the structure factor of the basic structure as defined in the equations 5 and 6. The second part gives as

result two delta functions $\delta(\vec{H} \pm n\vec{k})$ indicating the generation of the satellite reflections caused by the modulation of the basic magnetic structure with propagation vector κ. By solving the two integrals, one obtain:

$$FT[\rho_{s,mag}] = p\sum_{\mu}^{N_{cell}} M_{\mu,\perp} f_\mu(H)\exp[2\pi i\vec{H}\cdot\vec{r}_\mu] + p\sum_{\mu}^{N_{cell}}\sum_{n}^{\infty} f_\mu(H \pm nk)\frac{m^\mu_{n,c\perp} \pm i m^\mu_{n,s\perp}}{2}\exp[2\pi i\vec{H}\cdot\vec{r}_\mu] \quad (19$$

where f_μ represent the form factor of the μ[th] atom, $p = r_e\gamma/2$ (r_e is the classical electron radii and γ the magnetic moment of the neutron) is the conversion factor of the magnetic density from Bohr magnetons to scattering length units, and the other factor have the same meaning as in equation 6. This expression gives the structure factor for main and satellite reflections as:

$$\begin{aligned} F(\vec{H}) &= p\sum_{\mu}^{N_{cell}} \vec{M}_{\mu,\perp} f_\mu(\vec{H})\exp[2\pi i\vec{H}\cdot\vec{r}_\mu] \\ F(\vec{H} \pm n\vec{k}) &= p\sum_{\mu}^{N_{cell}} f_\mu(\vec{H} \pm n\vec{k})\frac{m^\mu_{n,c\perp} \pm i m^\mu_{n,s\perp}}{2}\exp[2\pi i\vec{H}\cdot\vec{r}_\mu] \end{aligned} \quad (20$$

Also in this case the intensity of the fundamental and satellite magnetic reflections is obtained as the modulus of the structure factors and are affected from the same corrections of the nuclear crystal reflections, like thermal factor, Lorenz correction, etc….

Now, it is possible to treat the problem within the superspace formalism in the same way used for the aperiodic crystals, defining a direct and reciprocal superspace and moving between the two spaces through the Fourier transform. Clearly, the magnetic structure possesses rotational and translational symmetry in the superspace; the generalization of the symmetry previously described is quite straightforward. Starting from the R_s matrix defined in equation 15 and taking into account the time inversion operator, the coloured superspace groups

are defined as the set of $\{R_s, \delta| \mathbf{t}\}$ operators that leaves the magnetic structure invariant, where δ is the time inversion operator and **t** is the four dimensions non integer translation. This acts on the magnetic moment of the j-th atoms as described in equation 3, remembering that now the magnetic moment have four components and the matrix is R_s instead of R.

Summarizing, a magnetic structure with a propagation vector $\kappa=(\alpha\ \beta\ \gamma)$ is described by a magnetic superspace group, an average magnetic structure defined in the nuclear unit cell and a series of modulation functions that describes the evolution of the magnetic moment with the propagation vector. The superspace magnetic group symbol is defined in the same way as for the nuclear superspace group, clearly taking into account the presence of primed elements. The fact that the average magnetic structure is described within the nuclear unit cell reduces the possible magnetic space group to the ones of type I, II and III. In fact, the use of the primed lattice translations typical of the type IV groups is meaningless in case of the superspace treatment of a modulated structure, in which the lattice periodicity is substituted by the periodicity of the modulation functions.

In most cases the average magnetic structure for incommensurate systems is a paramagnetic space group; however this does not mean that the system is paramagnetic but, instead, indicates that the average summation of the spins within the whole crystal give zero as result (it is basically a perfect antiferromagnetic structure). In this case, since the average magnetic space group is the paramagnetic ones, the magnetic structure factor of the main reflections is zero for symmetry, and the magnetic intensity is present only on the satellite reflections (figure 3-5). An example could be represented by the *Pnma1'(0 0 γ)0s0s* superspace group. The magnetic space group of the average magnetic structure is the grey group *Pnma1'* and the $\rho_{\mu,0}(r)$ terms of the generalized magnetization is constrained to zero by symmetry; as a consequence, the **F**(**H**) magnetic terms are zero as schematically represented in figure 3-5. These types of coloured superspace groups are very similar to the type IV

magnetic space groups; both possess a grey point group and the primed elements are part of the translations group of the system. In particular for the considered *Pnma1'(0 0 γ)0s0s* superspace group, the fourth direction of the (3+1)D space is primed because of the presence of the {1'| 0 0 0 ½ } operator.

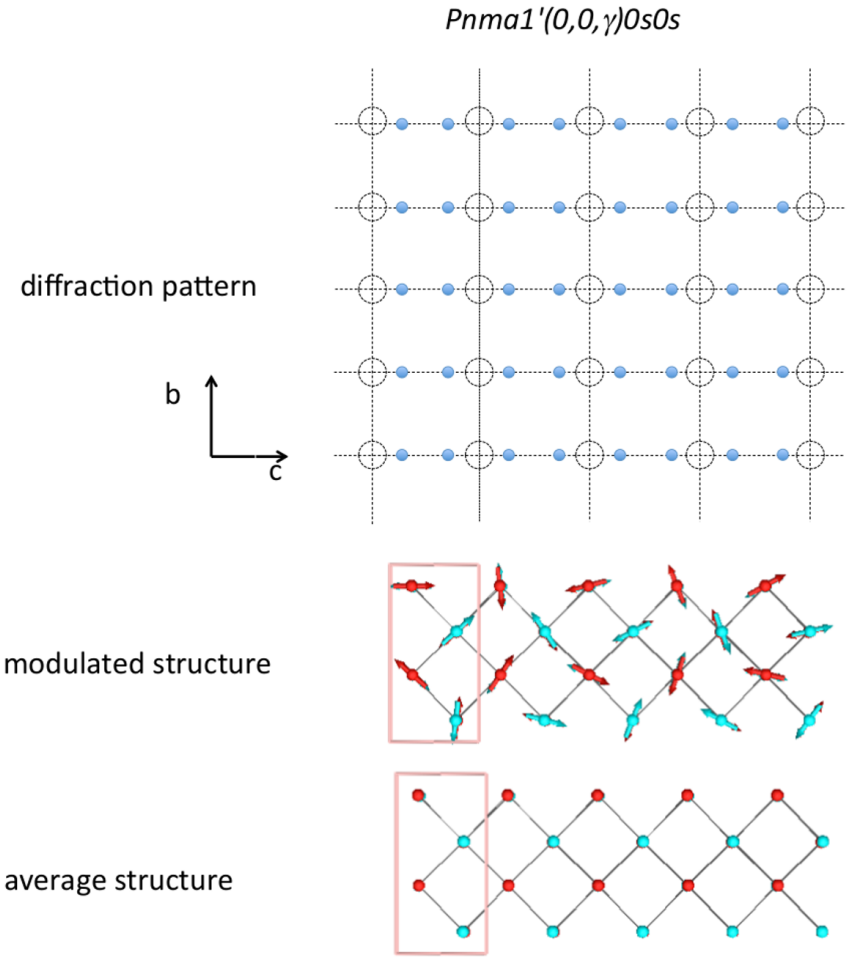

Figure 3-5 Schematization of magnetic diffraction intensities for a *Pnma1'(0,0,γ)0s0s* magnetic structure. The grey character of the average magnetic structure is highlighted by the absence of magnetic intensity on the main reflections,

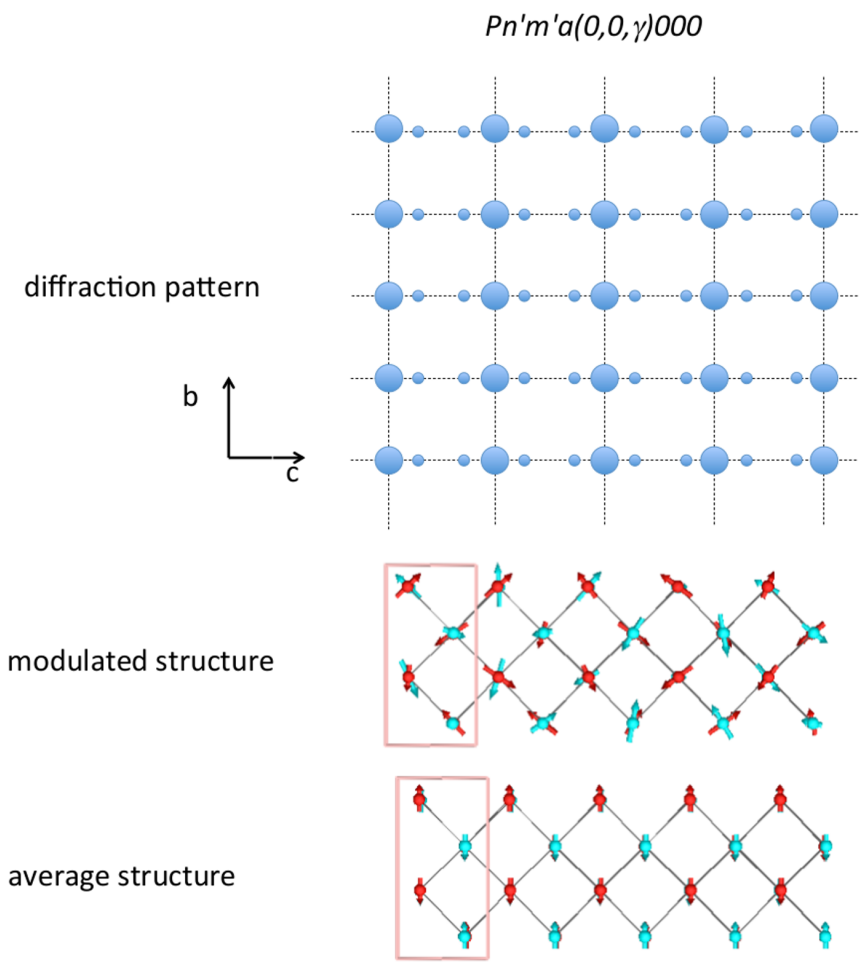

Figure 3-6 Schematization of magnetic diffraction intensities for a *Pn'm'a(0,0,γ)000* magnetic structure. The *Pn'm'a* space group of the basic magnetic structure groups allows the presence of magnetization within the nuclear cell and as consequence of magnetic intensity on the main reflections.

On the other hand, in more rare cases, the experimental diffraction pattern of incommensurate structures presents magnetic intensity on the main reflections, indicating the presence of an additional propagation vector κ=(0 0 0). This indicates, from a symmetry point of view, that the $\rho_{\mu,0}(r)$ term is different from zero. The superspace formalism allows the description of this type

of structure in a simple way, just by using a coloured group for the magnetic basic structure. For example let us take the *Pn'm'a(0 0 γ)000* superspace group. In this case the magnetic space group of the basic structure is *Pn'm'a;* the magnetic ordering within the nuclear cell, given by κ=(0 0 0), is governed by this space group and the magnetic structure factors are constrained by the symmetry operators. This implies that, at least for the main reflections, we have the same characteristic presented in section 3-3, like for example the presence of systematic absences. On the other hand, as schematically shown in figure 3-6, the diffraction pattern presents magnetic intensity on both main and satellite reflections.

3.7 Conclusion

In this chapter was described the magnetic symmetry and in particular the application of the coloured space groups to the description of the magnetic ordered systems. This formalism, on the contrary to the representation analysis formulated by Bertaut,[16] immediately gives in an explicit way the magnetic point group that rules most of the physical properties of the system. Nevertheless, the combined use of representation analysis and magnetic symmetry complete each other;[17-18] the implementation of the group theory analysis in the latest version of Jana2006[19] permits to find the possible space and superspace magnetic groups thought the Isotropy routine.

The use of the magnetic space groups and their generalization to the superspace formalism allow the study of any magnetic structure with general propagation vectors. Moreover, the study of both nuclear and magnetic modulations, if simultaneously present, is permitted. In this particular case both modulations must be described within the same asymmetric unit and constrained by the same superspace groups, finding a fundamental importance in the analysis of multifunctional materials, in which the various degree of freedom are intimately related. For example in type II multiferroics, were the magnetic

transition breaks both the time and spatial inversion symmetry, the magnetic superspace group must describe also the lattice distortion that generates the induced electrical polarization. Finally, yet importantly, the superspace formalism generalized to the magnetic symmetry offer the possibility to describe magnetic transition from incommensurate to commensurate structure by following the symmetry evolution.

3.8 Reference

[1] Shubnikov, A.V., Belov, N.V. & others, Colored Symmetry, (Oxford: Pergamon Press (1964)).

[2] the BNS setting refers to the formalism to indicate the magnetic space group introduced by N. V. Belov, N. N. Neronova and T. S. Smirnova, that referrer the indication of the magnetic space group on the G groups. This is in contrast with the OG setting, introduced by W. Opechowski and R. Guccione that referee the symbol on the H subgroups of G. The symbols are the same for type I,II,III but are different for the type IV.

[3] Bradley, C. J. & Cracknell, A. P. "T*he Mathematical Theory of Symmetry in Solids*" Oxford: Clarendon (1972).

[4] Stokes H. T. & Hatch, D. M. "*Isotropy Subgroups of the 230 Crystallographic Space Group.*" Singapore: World Scientific. (1987)

[5] Campbell B. J., Stokes H. T., Tanner D. E. and Hatch D. M., "*ISODISPLACE: An Internet Tool for Exploring Structural Distortions*" J. Appl. Cryst. (2006) 39, 607-614.

[6] Litvin D.B. "*1-, 2- and 3-Dimensional Magnetic Subperiodic Groups and Magnetic Space Groups*" IUCr ISBN 978-0-9553602-2-0 doi:10.1107/9780955360220001.

[7] Aroyo, M. I.; Perez-Mato, J. M.; Orobengoa, D.; Tasci, E.; de la Flor, G.; Kirov, A. "*Crystallography online: Bilbao Crystallographic Server*" Bulg. Chem. Commun. 2011, 43(2), 183.

[8] Aroyo, M. I.; Perez-Mato, J. M.; Capillas, C.; Kroumova, E.; Ivantchev, S.; Madariaga, G.; Kirov, A.; Wondratschek, H. "*Bilbao Crystallographic Server I: Databases and crystallographic computing programs*" Z. Krist. 2006 221, 15.

[9] Aroyo, M. I.; Kirov, A.; Capillas, C.; Perez-Mato, J. M.; Wondratschek, H. "*Bilbao Crystallographic Server II: Representations of crystallographic point groups and space groups*" Acta Cryst. 2006, A62, 115.

[10] Gallego, S. V.; Tasci, E. S.; de la Flor, G.; Perez-Mato, J. M.; Aroyo, M. I. "*Magnetic symmetry in the Bilbao Crystallographic Server: a computer program to provide systematic absences of magnetic neutron diffraction*" J. Appl. Cryst. 2012, 45, 1236.

[11] Brouns, E., Visser, J. W. & de Wolff, P. M. "*An anomaly in the crystal structure of Na_2CO_3*" Acta Cryst. (1964), 17, 614.

[12] Janner A. and Janssen T. "*Symmetry of incommensurate crystal phases. I. Commensurate basic structures*" Acta Cryst. (1980), A36, 399-408.

[13] Janner A. and Janssen T. "*Symmetry of incommensurate crystal phases. II. Incommensurate basic structure*" Acta Cryst. (1980), A36, 408-415.

[14] de Wolff P. M. "*The Pseudo-Symmetry of Modulated Crystal Structures*" Acta Cryst. (1974). A30, 777-785.

[15] de Wolff P. M., Janssen T. and Janner A. "*The superspace groups for incommensurate crystal structures with a one-dimensional modulation*" Acta Cryst. (1981), A37, 625-636.

[16] Bertaut E. F. "*Representation analysis of magnetic structures*" Acta Cryst. (1968). A24, 217-23.

[17] Petricek V, Fuksa J. and Dusek M. "*Magnetic space and superspace groups, representation analysis: competing or friendly concepts?*" Acta Cryst. (2010), A66, 649–655.

[18] Perez-Mato J.M., Ribeiro J.L., Petricek V. and Aroyo M.I. "*Magnetic superspace groups and symmetry constraints in incommensurate magnetic phases*" J. Phys.: Condens. Matter (2012), 24, 163201.

[19] Petricek, V.; Dusek, M.; Palatinus, L. "*Crystallographic Computing System JANA2006: General features*" Z. Kristallogr. (2014), 229, 345– 352.

4 Experimental

4.1 Synthesis

The synthesis of the $Pb_2(Mn,Co)WO_6$ compounds was performed via solid state reaction. Stoichiometric amount of PbO, $MnCO_3$, CoO and WO_3 were ground, heated at 800°C with a heating rate of 3°C/min and fired for two hours at this temperature. The reaction product was reground, pressed into pellets and sintered at 850°C for four hours obtaining a brownish polycrystalline ceramic sample. The synthesis of all compounds containing Mn^{2+} was performed in Argon atmosphere to prevent oxidation. In most of the samples a minor impurity phase was detected and identified as lead tungstate $PbWO_4$. The synthesis of the Mn-free end member of the solid solution, Pb_2CoWO_6 (PCW), was performed in air and the resulting powder was reground and sintered until the diffraction pattern shows only traces of a spurious phase, identified as Pb_2WO_5.

4.2 Diffraction experiments

Preliminary Powder X-ray Diffraction (PXRD) analysis, systematically used to check the solid state reaction progress, were performed on a Thermo ARL X'tra diffractometer equipped with Cu Kα radiation and a Si(Li) solid-state

detector to eliminate the fluorescence of manganese and cobalt. Temperature-dependent patterns were collected on the same diffractometer by using an Anton Paar TTK-450 chamber in the temperature range RT - 500 K.

Synchrotron single crystal X-ray diffraction data were collected on the ID09A beam line at ERSF in Grenoble at room temperature (RT). This beam line is mainly devoted to high-pressure experiment limiting the accessible portion of the Ewald's sphere. Nevertheless the small beam size, the use of a small wavelength λ = 0.41456 Å and the medium resolution of the data allowed to access important information, especially concerning the space group symmetry. The white X-ray beam is focused vertically by a spherical mirror and horizontally by a bent Silicon (111) monochromator obtaining a spot size of the 30x30 μm^2 on the sample. Diffraction data were collected on a Mar555 image-plate detector with a 430 x 350 mm (555mm diagonal) active area. The intensity integration was performed with the Oxford Diffraction software CrysalisRed-171.32.29 (Oxford Diffraction Ltd., Abingdon, England), using the profile fitting algorithm and no model refinement. Empirical rescaling and absorption correction were applied. Synchrotron Powder X-ray Diffraction (SPXRD) experiments were performed on the same beam line at RT, with the sample close in a fine capillary. The diffraction patterns were integrated using the Fit2D software. Temperature-dependent SPXRD patterns were collected on the ID15B beam line of ESRF, by using a liquid-helium-cooled cryostat in the temperature range from 4 K to RT. The used wavelength was λ = 0.1427 Å and the diffracted intensity was collected by means of a 2D CCD detector. The images were integrated using the fit2D software.

Constant Wavelength (CW) Neutron Powder Diffraction (NPD) patterns were collected at the Laue-Langevin Institute (ILL) in Grenoble on the D2B and D20 instruments. The D2B is a high-resolution diffractometer, thanks to the high take off angle (135°), operating with monochromatic neutron (λ = 1.594 Å). The detector banks are composed by 128 ^{3}He-counting tubes. The diffraction patterns were collected at selected temperatures. The D20 instrument is a high flux

instrument designed for the study of magnetic structure. The temperature-dependence experiment in the range 2 - 300 K were carried out with monochromatic neutron of λ = 2.41 Å. The diffracted intensity is recorded by ^{3}He microstrip gas-detector that covers 153.6° in 2-θ.

Time of Flight (ToF) neutron diffraction experiments were carried out at the ISIS facility, Didcot, UK. In this type of diffraction experiment the sample is irradiated by a short white neutron pulse obtained by a spallation source. From the measurement of the time of flight of the diffracted neutron on a fixed flight path and at a fixed scattering angle, is possible to obtain the diffraction pattern of the sample. The resolution in a time of flight diffraction experiment is influenced principally by three factors: the form and the time width of the neutron pulse that is dictate by the type of target and by the moderator; the length of the flight path that influence the separation of neutron with similar wavelength; the uncertainty in the scattering angle that is a consequence of the neutron beam divergence and that is minimized for backscattering geometry. The experiments at the ISIS facility were carried out on two instruments: HRPD and WISH.

HRPD is a High Resolution Powder Diffractometer on the ISIS target one station. The instrument is positioned at the end of a 100 m neutron guide, with a liquid methane (100 K) moderator that determine a incident flux with wavelength in the range 0.5 - 12 Å with peak flux at λ = 2 Å. The diffracted beam is collected in three banks with 2θ = 168, 90 and 30° and in the backscattering geometry the Δd/d is $4*10^{-4}$. The diffraction patterns were collected at different temperatures in the range 1.5 - 300 K, thanks to a helium cryostat.

The WISH (Wide angle In a Single Histogram)[1] instrument is located on ISIS target station two. This instrument has a dedicated solid methane (40 K) moderator giving a neutron pulse with wavelength in the 1.5 – 15 Å range, and a flight path of 40m constituted by a ballistic elliptic supermirror guide. The instrument has a 160° 2θ covering of 8 mm diameter ^{3}He gas tubes detector on both sides as shown in figure 4-1. The full coverage in 2-θ allows exploring a

wide d-spacing range (0.7 – 50 Å) with different resolutions. The detectors are coupled in 5 banks for each side with medium 2θ = 152.8°, 121.6°, 90°, 58.3° and 27.0°. The high neutron flux of the instrument, guaranteed from the high brilliance solid methane moderator, the high d-spacing range and the very low background of the instrument joined with the good resolution make WISH a world leader instrument for the magnetic structure determination and for the study of large unit cell systems. The diffraction data were collected on powdered samples, using a thin vanadium can sample holder, in the temperature range 1.5 K – RT thanks to a helium cryostat.

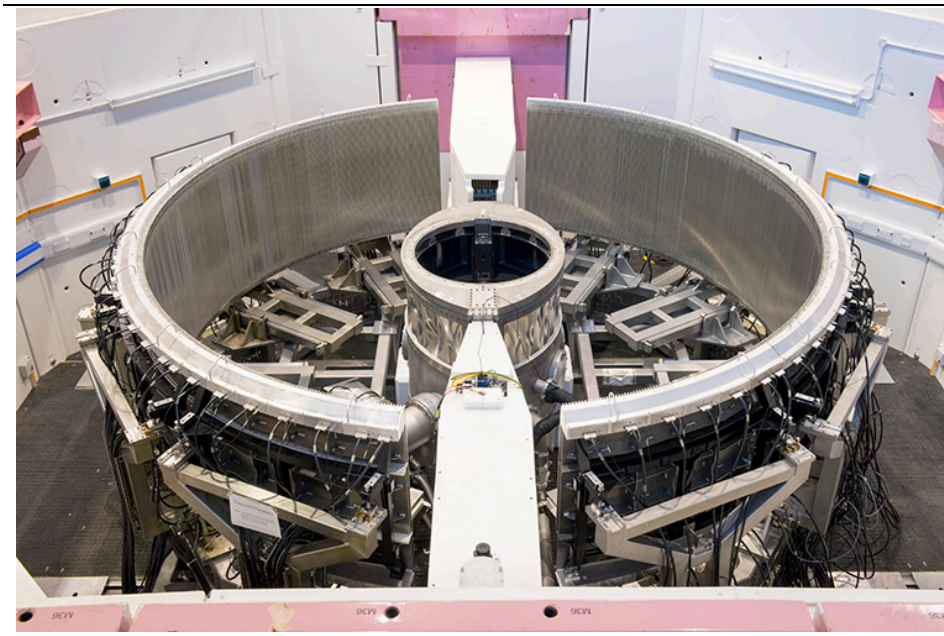

Figure 4-1 View of the WISH instrument detector and sample tanks.

Transmission electron microscopy (TEM) experiments were carried out on a Philips TECNAI F20 instrument operating at 200 kV at the CNR-IMM Institute (Bologna, Italy). The powder sample was ground in isopropanol and the suspension was deposited on a copper grid covered with a holey carbon film.

High-resolution image HREM and selected area electron diffraction (SAED) experiments were performed at RT.

4.3 Electric measurements

The electric measurements were carried out in collaboration with the IMEM-CNR Institute in Parma.

The DC electrical resistivity ρ was measured in a two contacts configuration in the temperature range 5 – 300 K. The dielectric constant was measured with a LCR meter HP4824A covering the frequency range from 20 Hz to 1 MHz applying a sinusoidal signal of 50 mV. In order to avoid contact effects the sample was covered by mica linings and measured according to Cabassi *et al*.[2]

Pyroelectric currents[3-5] were measured on a metalized sample using a Keithley electrometer 6517B for electric current detection and a Keithley 2400 Source Meter Unit for sample poling. In the measurements the sample is polarized at a poling temperature T_p by the application of an electric field E_p, and it is cooled down to T_0 keeping the electric field on. Subsequently the electric field is switched off and the sample is slowly heated at a linear heating rate up to T_p or higher. During the heating process, a pyroelectric current is released by the sample and by its integration the electric polarization of the sample originated by the action of E_p can be obtained.

Electric hysteresis loops were obtained by a AIXACCT TF-Analyzer 2000E ferroelectric tester at the Physics Department of the University of Parma. The measurements were performed following a Positive Up Negative Down (PUND) procedure.[6] A thin sintered pellet of the sample was lapped and metalized with a 20 nm layer of platinum, approximating a parallel plate capacitor. The PUND measurement is performed as follow. After a pre-polarization pulse, four pulses are applied to the sample two with positive direction and two with negative. During each pulse the polarization change in

the sample is recorded and, by subtraction between the two positive curves, the P(E) loop for the positive part is obtained. In the same way, using the two negative curve, the complete P(E) loop is reconstructed.

4.4 Magnetization measurements

The magnetization measurements were performed in collaboration with the Physics department of the University of Parma. Zero field cooling (ZFC) and Field Cooling (FC) magnetization measurement and hysteresis loops for all the samples were measured on a sintered pellet by means of a SQuiD MPMS XL Quantum Design magnetometer.

Electric field Magnetization Measurements (EMM) were carried out thin samples, metallized by sputtering in order to obtain a planar capacitor. To perform the measurements the sample, put in the SQuiD magnetometer, is cooled to the lowest temperature with an applied electric field. Then the electric field is released and a classical magnetization measurement (ZFC or FC) is performed.

4.5 Reference

[1] Chapon L.C. , Manuel P., Radaelli P.G. , Benson C., Perott L., Ansell S., Rhodes N.J. , Raspino D., Duxbury D., Spill E., and Norris J. "*Wish: The New Powder and Single Crystal Magnetic Diffractometer on the Second Target Station*" Neutron News (2011), 22, 22-25.

[2] Cabassi, R.; Bolzoni, F.; Gauzzi, A.; Gilioli, E.; Prodi, A.; Licci, F. "*Dielectric properties of doping-free $NaMn_7O_{12}$: Origin of the observed colossal dielectric constant*" Phys. Rev. B 2006, *74*, 045212.

[3] Muller, P. " *Phys. Status Solidi A*" (1981), 67, 11– 60.

[4] Bucci, C.; Fieschi, R.; Guidi, G. "*Ionic thermocurrents in dielectrics*" Phys. Rev. (1966), 148, 816– 823.

[5] Riva, S. C.; Bucci, C. A. "*Evidence for space charge polarization in pure KC1 at low temperatures*" J. Phys. Chem. Solids (1965), 26, 363– 371.

[6] Scott J F, Kammerdiner L, Parris M, Traynor S, Ottenbacher V, Shawabkeh A and Oliver W F "*Switching kinetics of lead zirconate titanate submicron thin‐film memories*" J. Appl. Phys. (1988) 64 787.

5 Pb_2MnWO_6 (PMW)

5.1 Room Temperature Crystal Structure

The PXRD pattern was indexed on the basis of a perovskite superstructure related to the primitive cell by the relations $\mathbf{a} = 2\mathbf{a}_p$, $\mathbf{b} = \sqrt{2}\mathbf{a}_p$, and $\mathbf{c} = 2\sqrt{2}\mathbf{a}_p$ ($\mathbf{a}_p \approx 3.9$ Å) and a minor impurity phase was detected and identified as lead tungstate $PbWO_4$.[1] The sintering time was increased to reduce the impurity phase and to increase the crystal size but the attempt resulted in a better-sintered sample with an increased $PbWO_4$ fraction, suggesting a kinetic control of the PMW growing. Selected area electron diffraction (SAED) patterns, taken in different zone axes, are reported in figure 5-1 and, by indexing the main reflections on the basis of the primitive cubic perovskite cell $\mathbf{a}_p \approx 3.9$Å, reveal the presence of a superstructure consistent with that previously found by PXRD and reported by Blasco et al.[2] In particular: a) the presence of (*h/2 k/2 0*) spots in both the [110] and [-110] directions is consistent with a rotation of the unit cell along the diagonal of the primitive perovskite cell; b) the cell doubling in the perpendicular direction is indicated by the presence of (*0 0 l/2*) reflections; (*h/4 k/4 0*) reflections along the [110] direction indicated the further doubling of the lattice parameter in one of the diagonal directions.

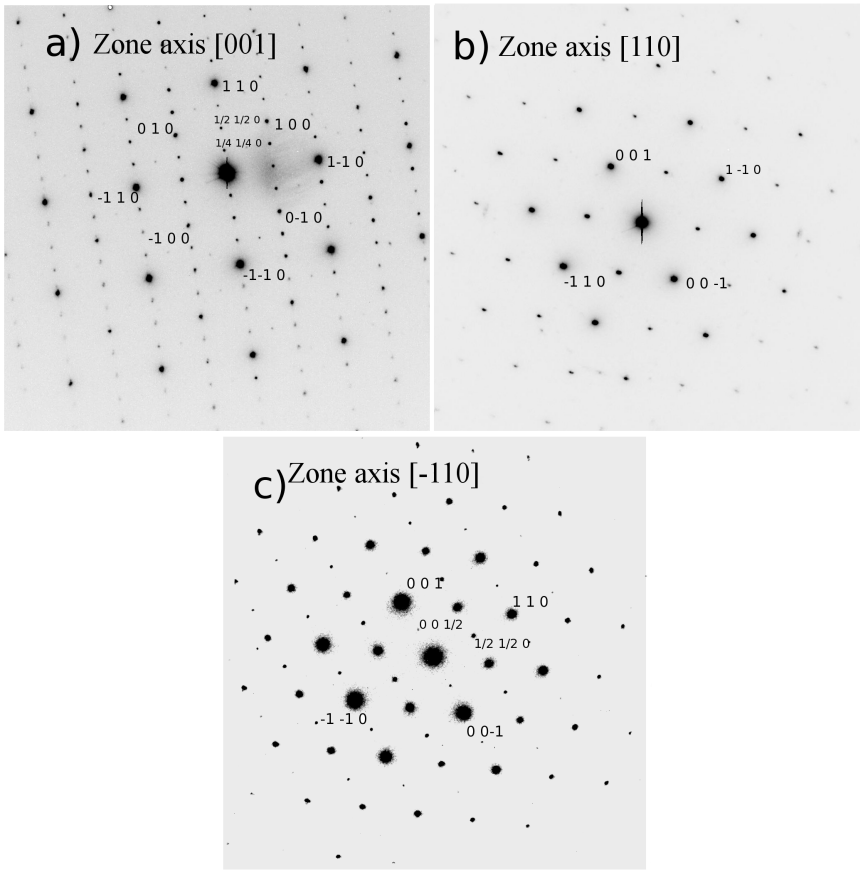

Figure 5-1 SAED patterns of PMW indexed on the basis of the fundamental perovskite.

Figure 5-2 shows some HREM images taken along different directions (clearly identified by the diffraction patterns calculated via fast Fourier transform of the images) on a long time sintered sample (850°C for 10h). The images reveal the presence of nanometric droplets segregated on the examined crystals, identified as lead by EDX analyses. They probably derived by sample decomposition of the grain surface, owing to the prolonged thermal treatment coupled with the low melting point and the high vapour pressure of the lead oxide. The occurring of partial sample decomposition in these conditions agrees with the observed increase of $PbWO_4$ phase. However it is worthy to underline

that the electron beam could in some extent, promote it also during the TEM experiment.

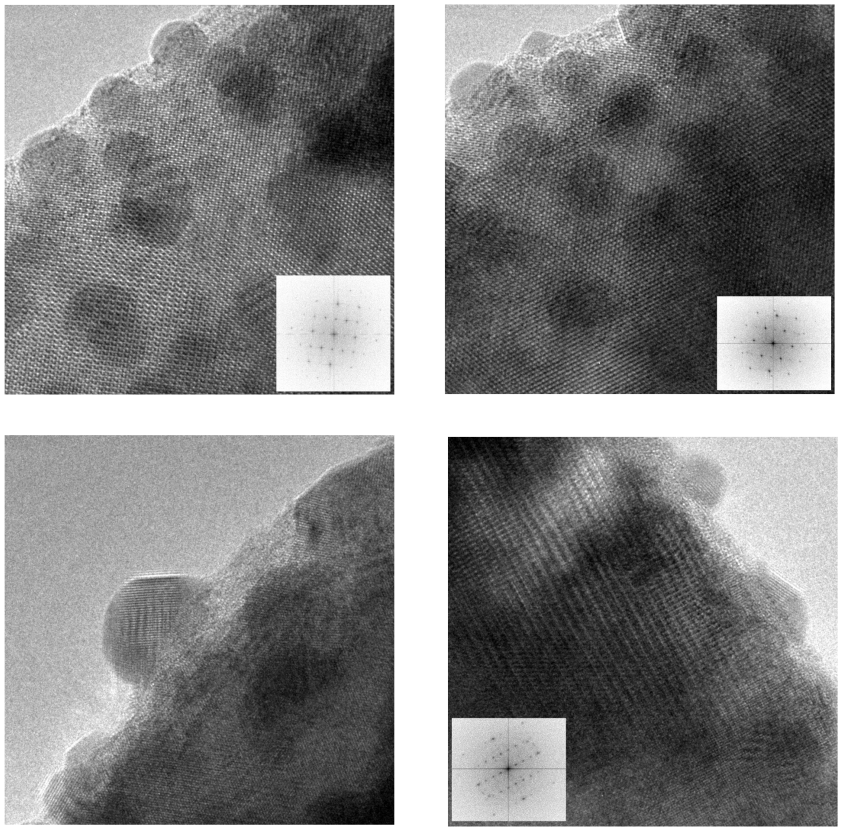

Figure 5-2 HREM images of the PMW sample with the corresponding Fast Fourier Transform in the insets. The images reveal the presence of segregate nanometric droplets, mainly consisting of lead by EDX analyses.

The crystal structure at RT was solved *ab-initio* by single crystal synchrotron X-Ray diffraction data collected at the ID09A beam line on a single crystal of dimension 2x2x2 μm^3 isolated from the powder sample. According to the systematic absences (*h0l* with *l* = 2n+1) observed for the experimental data, the possible space groups are restricted to *Pmcm*, *Pmc2* or $Pmc2_1$. These are in contrast with the *Pmna* space group previously reported in literature by powder

diffraction,[2] but it must be noticed that owing to the weak intensity of the superstructure reflections and to their superimposition in powder pattern, the correct identification of the space group is in this case possible only through the analysis of the systematic absences in single crystal data. The structure solution was attempted in all the possible space groups by direct method using the SIR2011 software.[3] The unique reasonable solution was found in the non centrosymmetric *Pmc2₁* space group. Unfortunately the ID09A beam line is suitable for high-pressure experiment and consequently only a portion of the Edward sphere was made accessible during the experiment, reducing the reflections/parameters ratio in the structure refinement. Therefore the structural refinement was carried out simultaneously by using single crystal synchrotron data, SPXRD and CW-NPD data by means of the Jana2006 software.[4] The SPXRD data were collected on the same beam line whereas the CW-NPD data were collected at the ILL on the D2B diffractometer. Atomic displacement parameters (ADP's) were refined anisotropically for Pb atoms, while a unique isotropic ADP was used for all the oxygen atoms, in order to stabilize the refinement. Crystal data and refinement parameters are reported in table 5-1 and atomic parameters in table 5-2. The Rietveld plots, showing a good agreement between observed and calculated data, are reported in figure 5-3.

Table 5-1 Crystal data and refinement parameters.

	Chemical formula	Pb_2MnWO_6	
	Space group	*Pmc2₁*	
	a (Å)	8.0370(2)	
	b (Å)	5.7857(2)	
	c (Å)	11.6378(4)	
	V (Å^3)	541.15(3)	
	Z	4	
	d(g cm^{-3})	9.19	
	single crystal SXRD	**SPXRD**	**CW-NPD**
λ(Å)	0.414556	0.414556	1.5943
GOF	1.51	0.66	1.50
R	0.0245	0.0294	0.0512
R_w	0.0245	0.0465	0.0600
Overall GOF		1.14	

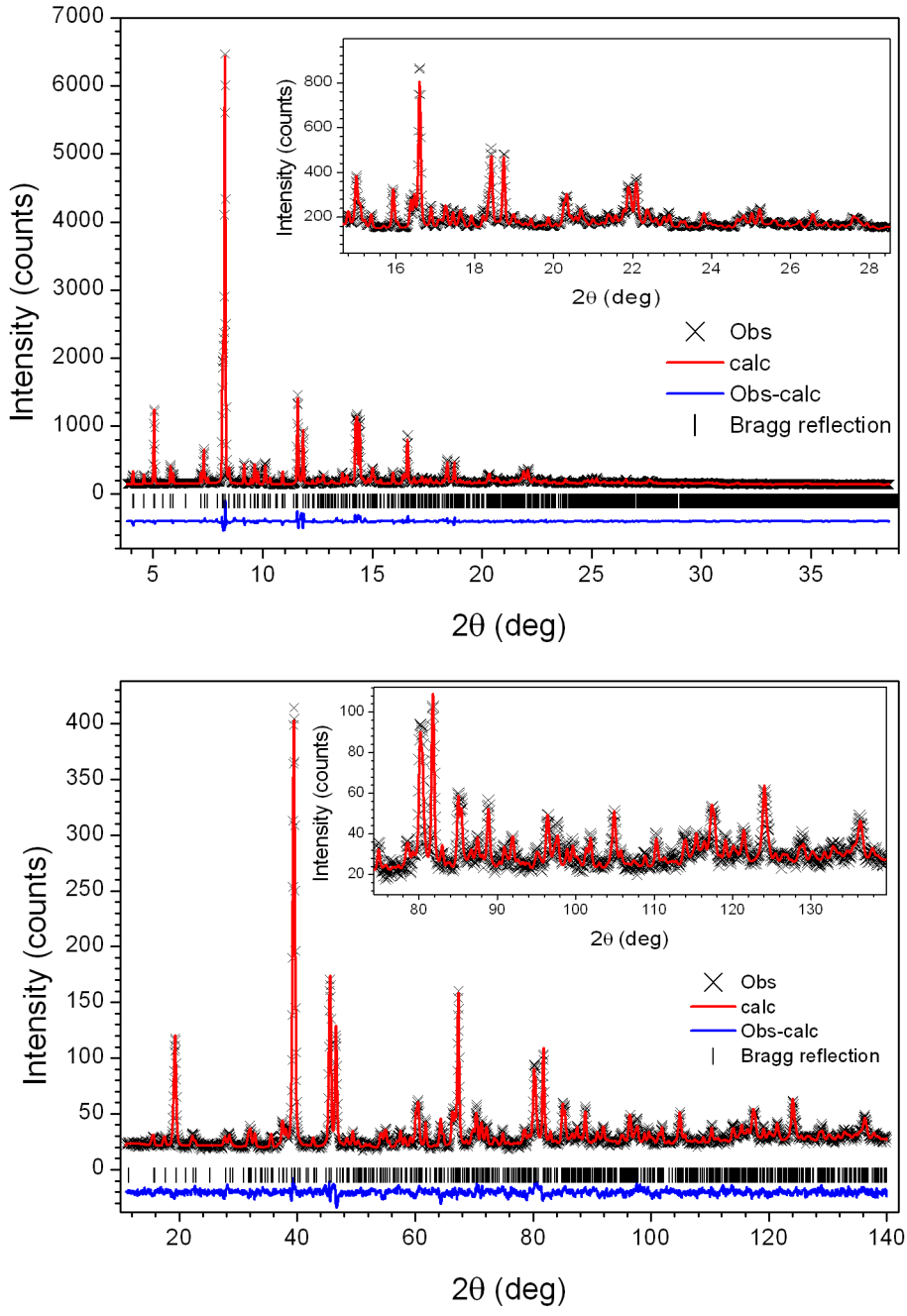

Figure 5-3 Rietveld plot of the PMW sample. (Top) SPXRD data and (bottom) NPD data. Observed (x, black), calculated (line, red), and difference (line, blue) patterns are reported. The tick marks indicate the Bragg reflections of the main PMW phase.

Table 5-2 Refined atomic positions and ADP's parameters at room temperature

Atom	x	y	z	U_{iso}/U_{eq} (Å^2)
Pb1	0.75589(18)	0.9628(2)	0.86685(16)	0.0230(6)
Pb2	0.74318(16)	0.5350(2)	0.58052(16)	0.0206(6)
W1	0	0.4970(4)	0.8449(2)	0.0097(3)
W2	0.5	0.0016(4)	0.6082(2)	0.0093(3)
Mn1	0.5	0.4860(13)	0.8459(9)	0.0130(11)
Mn2	0	-0.0055(18)	0.1034(11)	0.0129(15)
O1	0	0.7178(17)	0.7260(14)	0.0229(5)
O2	0	0.2999(19)	0.9806(15)	0.0229(5)
O3	0.5	0.750(2)	0.7118(13)	0.0229(5)
O4	0.5	0.243(2)	0.7064(14)	0.0229(5)
O5	0	0.2741(18)	0.7368(11)	0.0229(5)
O6	0.5	0.199(2)	0.4746(14)	0.0229(5)
O7	0.7331(10)	-0.0169(18)	0.5853(9)	0.0229(5)
O8	0.5	0.2982(18)	0.0015(11)	0.0229(5)
O9	0.7631(10)	0.5334(17)	0.8505(8)	0.0229(5)
O10	0	0.7595(17)	0.9685(12)	0.0229(5)

Atom	U_{11} (Å^2)	U_{22} (Å^2)	U_{33} (Å^2)	U_{12} (Å^2)	U_{13} (Å^2)	U_{23} (Å^2)
Pb1	0.0309(5)	0.0163(6)	0.0220(17)	0.0002(5)	-0.0016(8)	0.0083(5)
Pb2	0.0203(3)	0.0180(7)	0.0237(16)	0.0035(5)	0.0044(6)	-0.0033(5)

The RT structure of PMW is an orthorhombic double perovskite with the B site of the structure completely ordered in a rock-salt arrangement of the Mn and W atoms. The different volume of their coordination octahedra, joined to the large valence gap, represents the driving force for the ordering. Valence sum calculations performed with the CHARDIS99[5] software indicate values close to the theoretical ones expected for this composition. The octahedral network presents a very limited tilting in the ***bc*** plane, as pointed out by the value of the W-O-Mn bond angles ranging from 170 to 180°. Nevertheless the strongly stereoactive lead atoms[6] influence the B site coordination polyhedra in particular along the ***a*** direction, where they induce an important bending of the apical oxygen and a decrease the W-O-Mn angles, in one case to about 164°. The coordination polyhedra of the two independent lead atoms are strongly asymmetric and present two different types of coordination schematically drawn in figure 5-4. Pb1 form four almost equivalent short bonds (figure 5-4c), ranging from 2.49(1) to 2.583(9) Å, and create a PbO_4E coordination polyhedra, in which E stand for the hybridized lone pair. On the contrary the Pb2 site give rise

to three shorter bonds ranging from 2.366(7) to 2.595(10) Å, generating a PbO_3E environment as shown in figure 5-4b. These two types of coordination are typical of the post-transition metal oxides,[7] and are due to the stereoactivity of $6s^2$ lone pair of the lead atoms trough Second-Order Jahn-Teller (SOJT) instability.[6]

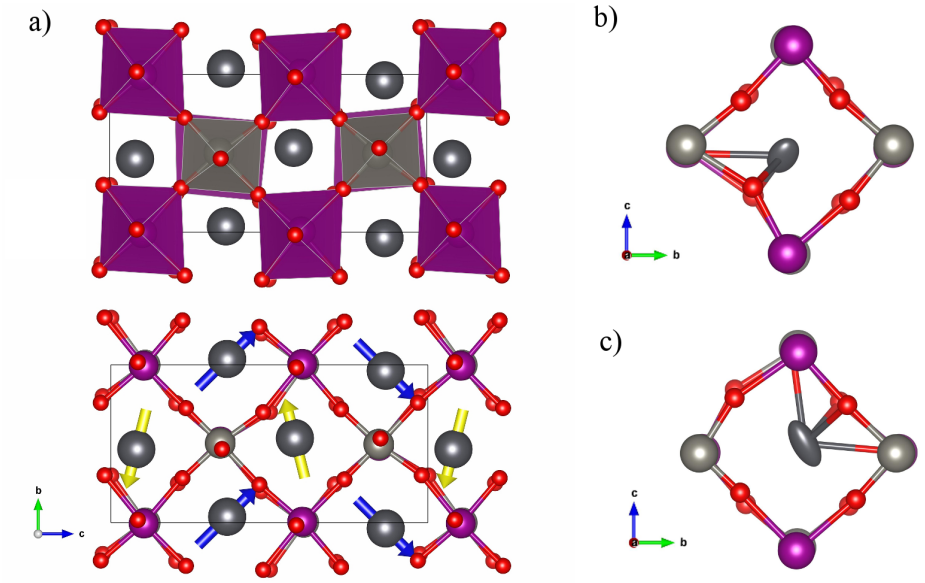

Figure 5-4 Graphic representation of the PMW structure at RT: a) projection of the structure in the ***bc*** plane, where violet and grey spheres refer to Mn and W atoms, whereas the black ones to lead; the arrows indicate the direction of the local displacement of the two lead sublattices, giving rise to a net dipolar moment along ***c***; b, c) graphical representation of the coordination, in the perovskite cage, of the two independent lead atoms Pb1 and Pb2.

The magnitude of the octahedral distortion of the B sites, Δd, could be calculated according to Halasyamani[7]

$$\Delta d = \frac{|(B-O1)-(B-04)|}{\cos(O1-B-O4)} + \frac{|(B-O2)-(B-05)|}{\cos(O2-B-O5)} + \frac{|(B-O3)-(B-06)|}{\cos(O3-B-O6)} \qquad (1$$

where the pairs (O1-O4) etc. are opposite oxygen atoms respect the B cation. By applying equation 1, the Mn ions are in the range of a week distortion, with Δd =0.29 and 0.19 Å for Mn1 and Mn2 respectively, whereas the W ions present a larger distortion, with Δd =0.35Å for W1 and Δd =0.37 Å for W2. The possible mechanisms to explain the distortion are Second-Order Jann Teller (SOJT) effect (or pseudo Jahn-Teller effect)[8] and Secondary Distortive Effects,[7] generated by the presence of the strongly stereo-active Pb^{2+}. The former is characteristic of d^0 cation, like W^{6+}, but it has been shown by I. B. Bersuker[8] that a SOJT effect is theoretically possible also for the Mn^{2+} in d^5 high spin configuration. The second is a secondary effect on the BO_6 octahedra due to asymmetric bond networks and to the lattice stress generated by the distorted Pb environment. In the present case, both contributions are present and is quite difficult to distinguish between them.

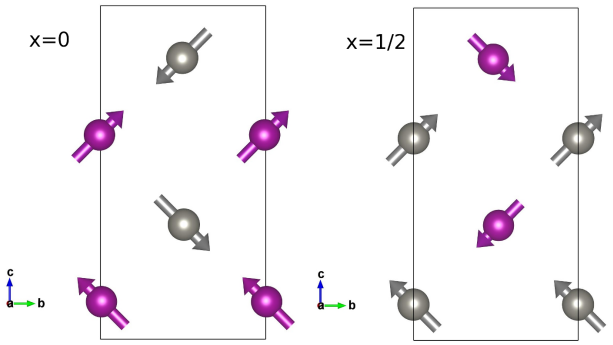

Figure 5-5 Schematic representation of the Mn (violet) and W(grey) displacements from the center of the oxygen polyhedra, indicated by arrows in the displacement direction; both sublattices are unbalanced, giving rise to an electrical polarization along the ***c*** direction.

In order to analyse the off-centre arrangement of the different species in the structure, six sub-lattices, two for each cation in the system, are taken into account. The two sublattices generated by the lead atoms, organized in row parallel to the ***c*** axis, are shown in Fig. 5-4a, in which the arrows indicate the

direction of the displacements. Both the sublattices produce non-zero resultants that are coupled antiferroelectrically but, being unbalanced, they give rise to a net dipolar moment along the ***c*** direction of the structure. A similar situation involves the B sites (figure 5-5); the displacements of Mn and W atoms are coupled in an anti-polar way in the x = 0 and x = 0.5 plane; however, also in this case the localized distortion are not balanced and a net dipolar moment is generated along the ***c*** axis. Therefore the PMW structure can be considered a complex ferrielectric structure, in which ***c*** represents the polar axis of the structure.

5.2 Thermal evolution of the structure

The thermal evolution of the structure was followed from RT to 500 K by PXRD measurements whereas low temperature region, from 2 K to RT, was monitored by CW-NPD data collected at the D20 beam line. The evolution of the lattice parameters of the fundamental perovskite and the trend of the volume as function of the temperature are reported in figure 5-6. The measurements point out a transition from the orthorhombic RT structure to a cubic high temperature phase, already reported by Blasco et al.[2] This transition was identified as a antiferroelectric to paraelectric transition characterized by an order to disorder mechanism.[9] It's worthy to underline that the transition is characterized by a decrease of the cell volume by increasing the temperature. Moreover, the analysis of the lattice parameters reveals, at the transition, a contraction of the ***bc*** plane and an expansion in the perpendicular direction, caused by the release of the bending of the O-B-O angle. This behaviour is anticipated in the orthorhombic phase, where it becomes particularly evident above RT, and is in agreement with the ferrielectric nature at RT revealed by the structure analysis.

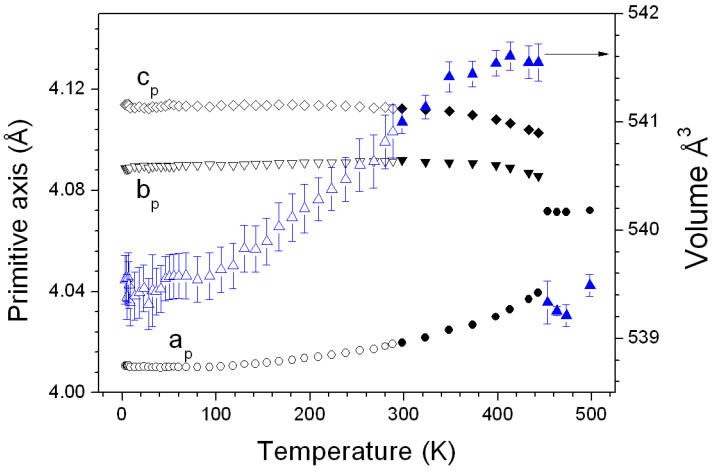

Figure 5-6 Left axis) Lattice parameters of PMW (black symbols) as a function of temperature, reported in terms of fundamental perovskite cell. Right axis) Unit cell volume (blue symbols) as function of the temperature. Empty and filled symbols refer to neutron and XRD data, respectively.

For what concerns the low temperature behaviour, the analysis evidenced a series of weak anomalies. By decreasing the temperature, the first anomaly is observed below 200 K and consists in a change in the slope of the thermal evolution of the ***c*** axis (figure 5-7). Being this the polar direction of the system, the anomaly may be an indication of a change in the electrical order of the system. However, no symmetry change or appreciable variation of the structure was revealed by the refinement of NPD data collected at 200 and 140 K, using the RT structure as starting model for the Rietveld refinement (figure 5-8). Further anomalies in the trend of the lattice parameters are observed at 45 and 10 K, as shown in figure 5-7. It is interesting to note that the ***a*** parameter, which is related to the major distortion of the octahedral tilting, becomes almost constant below 80 K, indicating a freezing of the deformation.

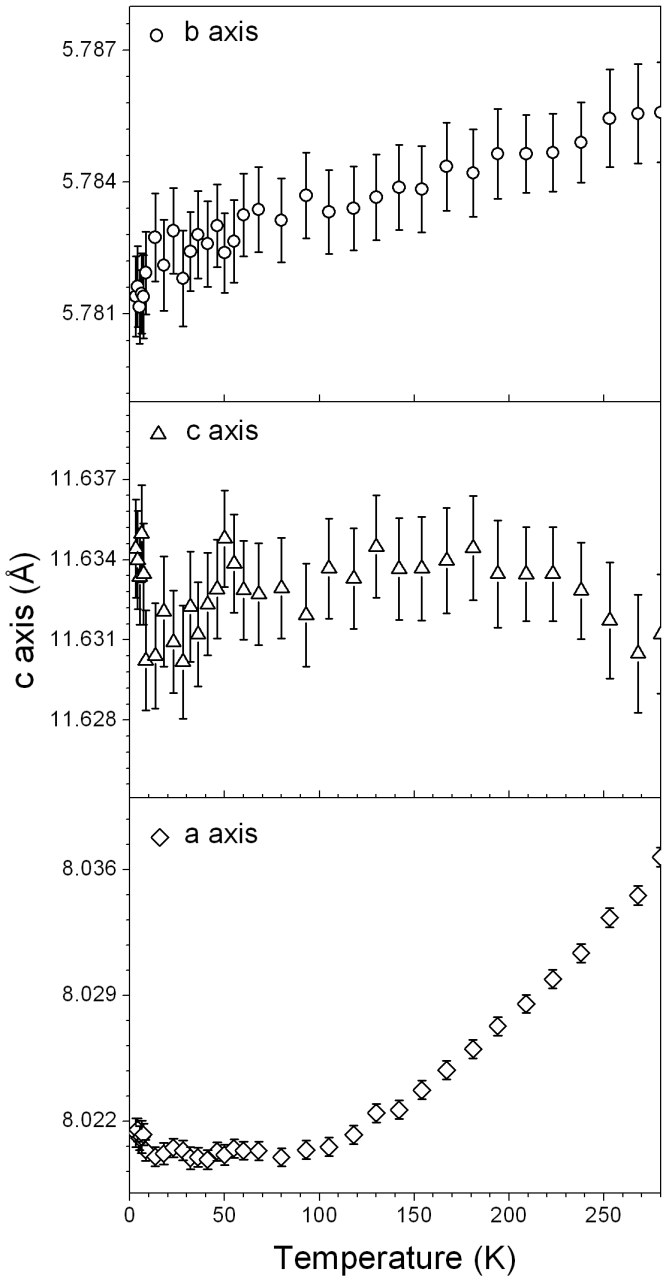

Figure 5-7 Thermal evolution of the lattice parameters as function of the temperature for PMW.

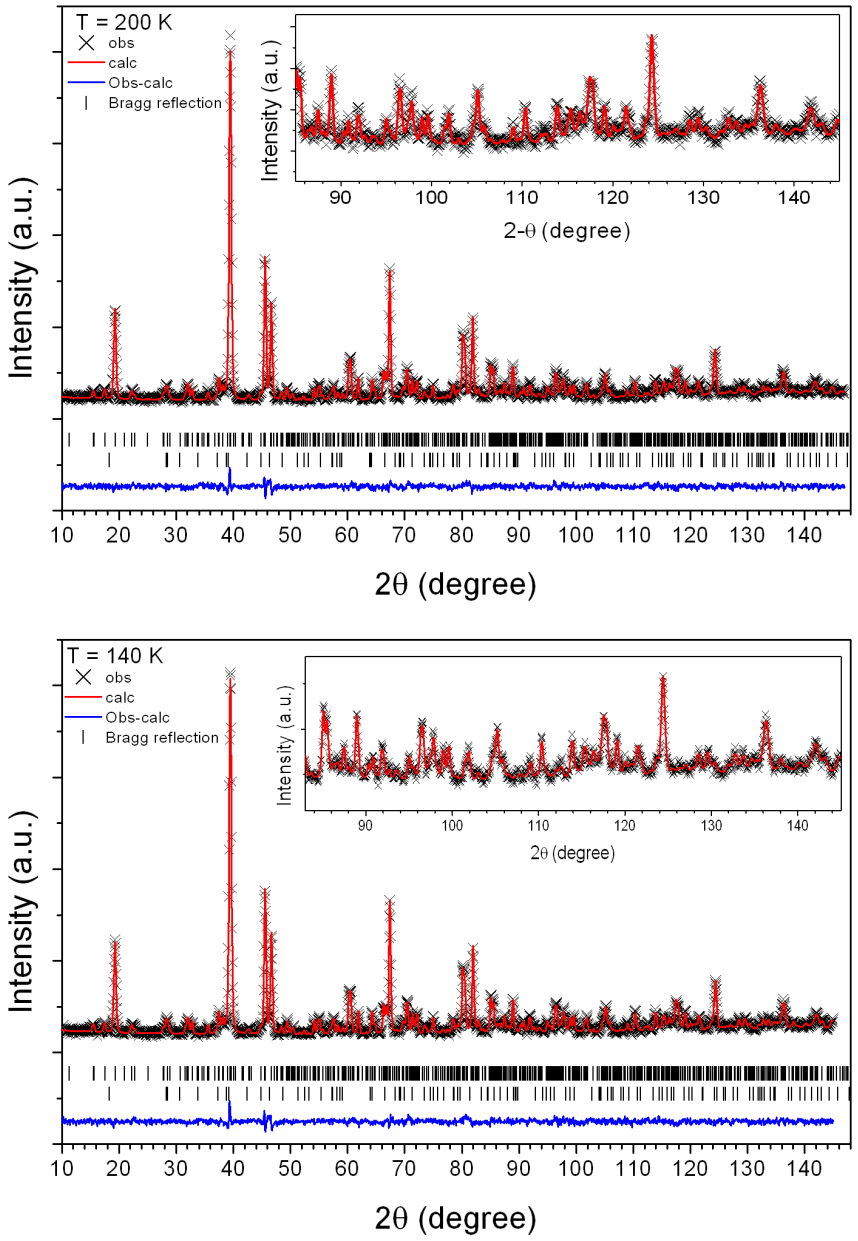

Figure 5-8 Rietveld plot of the 200 and 140 K NPD data. Observed (×, black), calculated (line, red), and difference (line, blue) patterns are reported. The upper tick marks indicate the reflections of the main PMW phase, whereas the bottom ones those of the impurity phase $PbWO_4$.

5.3 Electrical characterization

The DC electrical resistivity ρ was measured from T = 380 K to T = 90 K (Figure 5-9); below this temperature the insulating properties of Pb_2MnWO_6 exceeded the instrumental sensitivity, making the measurement meaningless. In the whole temperature range ρ was found to be independent of the applied voltage, at least in the range ±150 V, as shown in the inset of figure 5-9. Measurements were carried out with applied voltages ranging from 10 V to 200 V. The resistivity follows a semiconducting behaviour given by $\rho=\rho_0 \exp(E_\rho/kT)$, at least down to T = 230 K, with activation energy E_ρ = 0.53 eV; a drastic change is observed around 170 K and could be related with that anomaly observed in the thermal evolution of the polar axis of the structure at the same temperature.

The sample is characterized by high values of the dielectric constant, whose evolution with the temperature, is reported in figure 5-9, and shows the existence of an electric transition with a large thermal hysteresis. The transition, consisting in a sudden jump, occurs at 90 K if the measurement is performed on cooling, but it is shifted around 170 K on warming. The transition, not affected by the frequency of the AC electric field, could be related with the change in the resistivity, which occurs at the same temperature, and with the one observed in the evolution of the cell parameters, recalling that the measurements were performed in that case on warming. The large hysteresis is a possible indication of a first order transition; nevertheless no change in the crystal symmetry or discontinuity in the cell volume were detected from the high-resolution diffraction data collected at the D2B instrument.

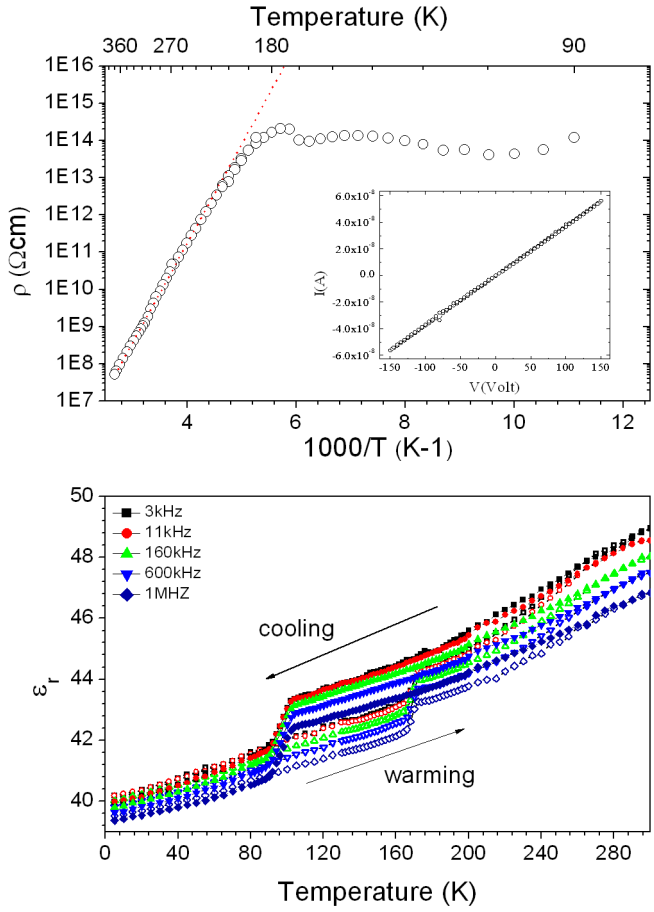

Figure 5-9 Top) Electrical resistivity in the temperature range 90 - 380 K; the dashed line corresponds to the Arrhenius fit with an activation energy of 0.53 eV. The I(V) characteristic, measured at T = 290 K, is shown in the inset. Bottom) Dielectric constant measured at different frequencies; the full and empty symbols indicate measurements performed on cooling and warming, respectively.

The behaviour of both electrical resistivity and permittivity near 170 K indicates a change in the transport properties of the system. The transition from a thermally activated conduction mechanism to a nearly constant value of the resistivity may be attributed to a possible localization or freezing of the conduction charges. Moreover the concurrence between the thermal expansion

change of the polar axis of the structure and the dielectric anomaly could be reasonably attributed to some electronic and transport transition that do not induce any evident crystal transformation.

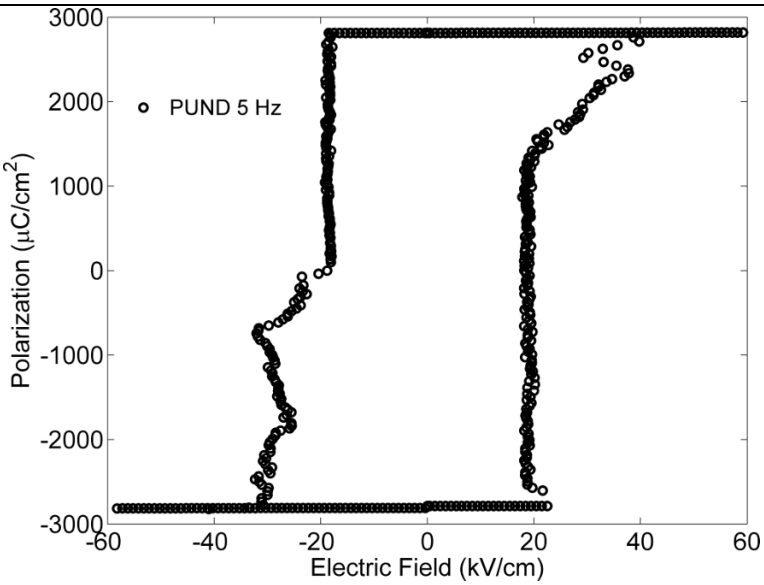

Figure 5-10 Ferroelectric hysteresis measurement performed with a Positive Up Negative Down (PUND) technique with pulse frequency of 5 Hz and 2 kV of amplitude.

The electrical polarization of the system was studied both in continue and alternate condition. The AC hysteresis loop of the PMW sample is shown in figure 5-10. The measurement was performed following a PUND procedure[10] using pulses with intensity V = 2000 V and frequency f = 5 Hz. The sample presents a hard hysteresis loop with a symmetric coercive electric field E_C =20 kV/cm and a saturation polarization P_S = 2.85 μC/cm^2. The value of the coercive field is close to the standard values obtained for lead zirconate titanate (PZT).[20] However we must take into account that in a polycrystalline sample the observed coercive electric field could be overestimated, due to the presence of morphological defects and grain boundary.

Some features of the loop deserve some discussion. The structural characterization indicates a ferrielectric configuration, in agreement with the

square form of the loop that represents another indication of the ferrielectric nature of the sample. The phenomenology of polarization reversal of ferrielectrics has been investigated by C.F. Pulvari by analysing the electric behaviour of mixed niobates[11] and bismuth titanates.[12] Pulvari's observations indicate that an electric field higher than the coercive force of the system is required to open a ferrielectric hysteresis loop. The presence of a threshold is emphasized by the fact that below a certain field the hysteresis loop does not appear: the material, in these conditions, shows the behaviour of a linear dielectric (as shown later) in contrast to the classical ferroelectric phenomenology in which the saturation is gained by a smoothed evolution. This sudden onset of the polarization gives to the P-E loop the particular square shape even in presence of a polycrystalline ceramic.

The noisy region of the hysteresis detected between 20 and 40 kV/cm has two principal causes. First the zig-zag feature, present in particular in the $E<0$ part of the loop, are artificially introduced by the instrument. Instead, the long tails of the loop are due to the metastable antipolar states of the sample that are not converted when the critical switching field is achieved. Generally in ferrielectrics this process is not completed and part of the sample is likely locked to the antiferro dipole condition. In earlier studies[12] this stage is recognized as an intermediate dynamical situation, which is quickly suppressed by increasing the maximal limit of the applied electric field. The presence of these regions is probably related to the microstructural defect that could act as pinning point for the electric domains.

The DC electric polarization as a function of the temperature was studied by means of pyrocurrent measurements.[13-15] In figure 5-11a are shown typical pyrocurrent measurements of the PMW sample polarized at T_p = 380 K with E_p = 3125 V/cm, that represents the maximal electric field provided by the available equipment. The measurements present two broad peaks at T_1 = 80 K, T_2 = 217 K and a narrow peak at 165 K. The three anomalies are reproduced with unchanged characteristic temperatures in different measurements,

performed by changing the poling field E_p and by applying an external magnetic field in the range 80 - 275 K.

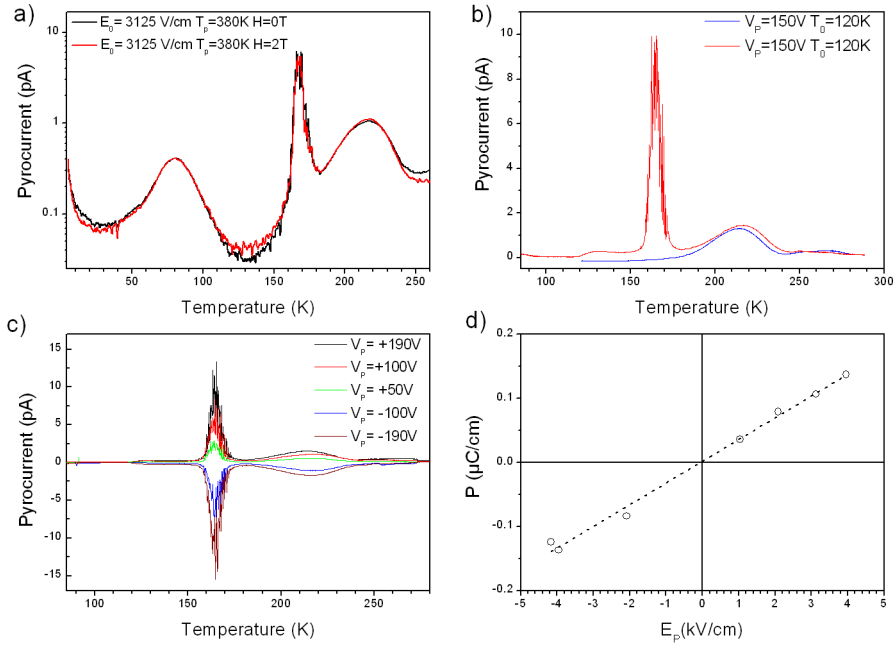

Figure 5-11 Pyrocurrent measurements of the PMW sample in different conditions. a) Pyrocurrent measurements in logarithmic scale with E_p = 3125 V/cm and T_p = 380 K performed in absence of magnetic field (black line) and in 2 T (red line). b) Pyrocurrent measurements performed by cooling the sample below (red line) and above (blue line) 90 K. c) Series of pyrocurrent measurements performed by poling the sample at different voltages. d) Static electric polarization at T_p = 273 K as a function of the poling field obtained by integration of the measurements shown in figure 5-11c.

The sharp peak at 165 K seems to be clearly associated to the phenomena observed in both resistivity and dielectric constant measurements. To corroborate this observation, different pyrocurrent measurements were performed by cooling the sample at different T_0 temperatures. The measurements show that the sharp pyrocurrent peak appears always at the same temperature (figure 5-11c), but only if the sample is cooled below 90 K (figure 5-11b); this is

consistent with the wide hysteresis observed in the dielectric constant temperature dependence. Figure 5-11c shows that the sign of the electric polarization developed around RT can be switched by the inversion of the poling voltage. The static electric polarization of the material at T_p = 273 K, obtained by the integration of the pyrocurrent, is reported in figure 5-11d as a function of the applied poling field. The linear behaviour and the null remanence are consistent with the ferrielectric nature of PMW, though the threshold field could not be reached in these cases by means of the available voltage.

5.4 Magnetic characterization

The sample shown two magnetic transitions by decreasing the temperature at T_{C1} = 44 K and T_{C2} = 9 K as shown in figure 5-12. The Curie-Weiss fit of the paramagnetic region of the inverse susceptibility reveals an antiferromagnetic (AF) nature of the interaction between the magnetic ions (Θ_{CW} = -24.3 ± 0.1 K) and a moment μ_{eff} = 5.7 μ_B in agreement with Mn^{2+} ions in high spin configuration with quenched orbital momentum. Despite the AF magnetic interaction, the system shows a weak ferromagnetism (FM) evidenced by the irreversibility between ZFC e FC measurements. Moreover the M(H) measurement at 3 K shown in figure 5-12 indicates an almost linear response confirming the AF nature of the sample; nevertheless a small opening of the cycle with a coercive field of 0.016 T was detected at 3 K (see inset figure 5-12) and at 25 K.

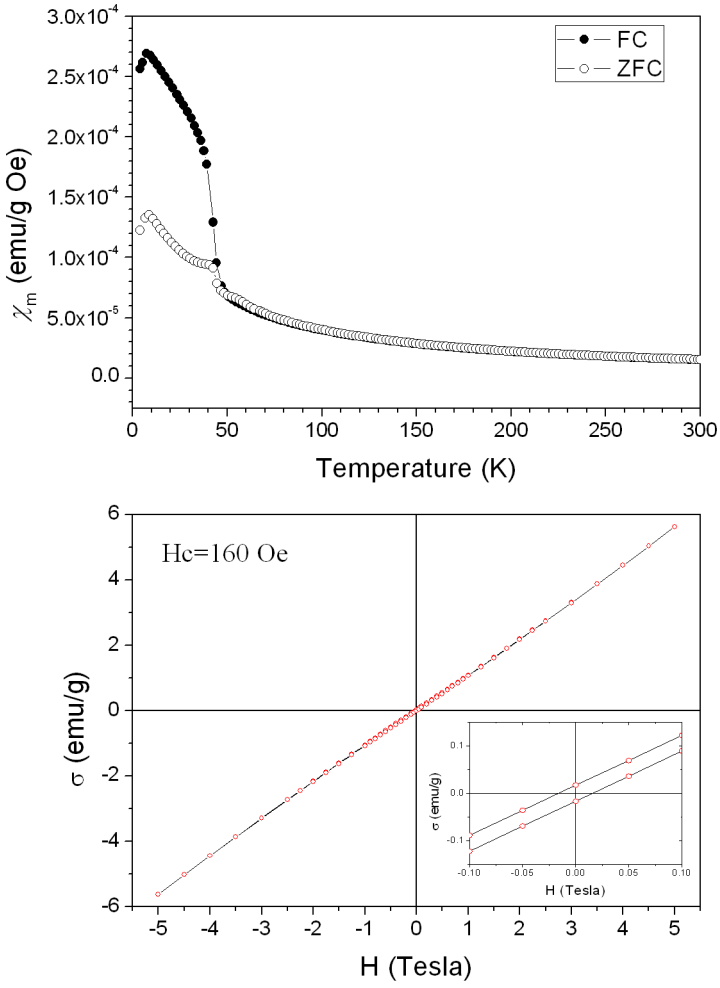

Figure 5-12. Top) ZFC and FC curves measured by applying H=50 Oe in the temperature range 4 - 300 K. Lower panel) Hysteresis loop of the PMW sample in the field range ±5 T; a zoom of the low field region that show the small coercive field of 160 Oe is shown in the inset.

In figure 5-13 are shown the zero field cooling (ZFC) and field cooling (FC) measurements at different applied fields. An interesting field dependence of the ZFC-FC curves is observed; in particular by increasing the applied field the 44 K transition is strongly reduced and disappears for field higher than 5

kOe. For the highest field, the irreversibility between ZFC and FC curve is suppressed. On the contrary the 9 K transition remains evident in all the measurements, in spite of a monotone decrease of the susceptibility with the applied field.

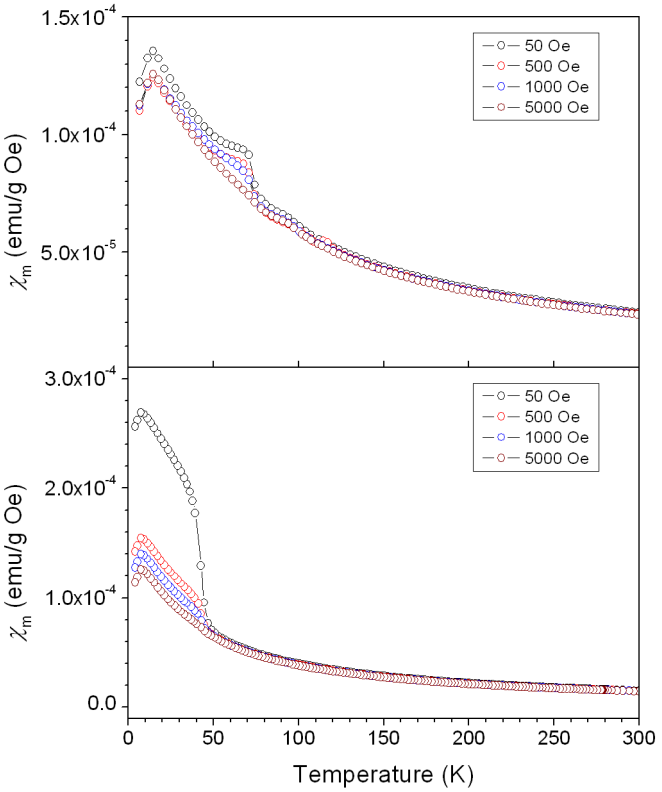

Figure 5-13 Field dependence of ZFC (top) and FC (lower panel) curves in the range 50 Oe – 5 kOe.

5.5 Magnetic structure analysis and discussion

To analyse the magnetic structure of the system, a series of CW-NPD experiments were carried out at the ILL institute on the D20 beam line and at the D2B. Some diffraction pattern are shown in figure 5-14 as function of

temperature, pointing out the appearing, below 10 K, of additional reflections connected to the long range magnetic ordering related to the second critical temperature T_{C2} observed in the magnetization measurements.

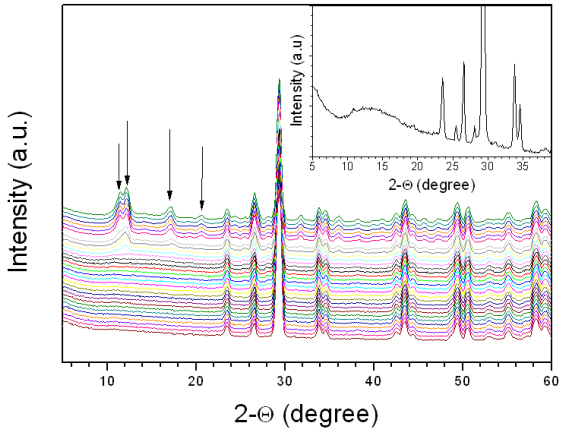

Figure 5-14 NPD data in temperature obtained at the D20 line with λ=2.41 Å, the arrows indicate the magnetic reflections. (Inset) zoom of the low angle region of the 10K diffraction pattern in which is clearly visible a diffuse scattering.

These reflections can be indexed with a propagation vector κ_1=(¼ 0 0) at 2 K. On the contrary no additional reflections appear below the magnetic transition at T_{C1} = 44 K, where only a diffuse scattering indicative of a short range ordering is observed (figure 5-14, inset). The diffuse scattering at low angle was fitted to obtain the average correlation length. Different models were used and it is interesting to note that the profile shape does not follow the characteristics of a Warren type function,[16] suggesting a 3D nature of the short range ordering. The best fit of the broad diffuse peak was obtained, after the background subtraction, with a Gaussian function. The average magnetic correlation length, calculated by the Sherrer formula (K=0.9) applied to the fitted profile, was found to be 19(1) Å.

The magnetic structure analysis was carried out with the superspace formalism.[17] In this methodology, described in details in chapter 3, the magnetic structure is described by a conventional structure related to the nuclear fundamental cell associated to a series of magnetic modulation functions, with propagation vector κ, that describe the variation of the momentum from the basic structure.[18,19] The magnetization of the j-th atom in the unit cell is therefore defined by the value on the basic structure $M_{j,0}$, described by a classical coloured Shubnikov groups,[20] and from a modulation function $M_j(x_4=t+\boldsymbol{\kappa}\bullet\boldsymbol{r}_{l,j})$ in which x_4 is the so called internal coordinate and $\boldsymbol{r}_{l,j}$ indicates the position of the j-th atom of the basic structure in the l-th unit cell. The modulation function can be expressed in a Fourier series:

$$\vec{M}_j(\vec{k}\cdot\vec{r}_{l,j}) = \vec{M}_{j,0} + \sum_{n=1}^{\infty}[\vec{M}_{j,ns}\sin(2\pi n\vec{k}\cdot\vec{r}_{l,j}) + \vec{M}_{j,nc}\cos(2\pi n\vec{k}\cdot\vec{r}_{l,j})] \qquad (1$$

The analysis of the diffraction pattern indicates the presence of magnetic intensity on the nuclear reflections, with propagation vector κ_2= (0 0 0), and consequently the $M_{j,0}$ terms differ from zero. The systematic absences of the magnetic pattern were analysed with the help of the Bilbao crystallographic server[21-23] and in particular with the program MAGNEXT.[24] The observed absences of 00l reflections with l=2n+1 indicate as possible magnetic space groups of the basic magnetic structure $Pmc2_1$ (Fedorov group) or alternatively $Pm'c'2_1$. The combination between this two space groups with the propagation vector κ_1=(1/4 0 0) produce four possible super-space groups: $Pmc2_1(\alpha00)000$, $Pmc2_1(\alpha00)0s0$, $Pm'c'2_1(\alpha00)000$, $Pm'c'2_1(\alpha00)0s0$.

The Rietveld refinement was attempted in all possible super-space groups by means of the Jana2006 software[4] and the best agreement between the observed and calculated model was found for the $Pmc2_1(\alpha00)0s0$ magnetic space group. Crystal data and parameters of the Rietveld refinement carried out on the D20 and D2B data at 2 K are reported in table 5-3. In the $Pmc2_1$ magnetic space

groups of the basic magnetic structure the two independent manganese sites lie on the mirror plane, forcing the magnetic moment of the basic structure along the ***a*** axis.

Table 5-3. Crystal data and refinement parameters at 2 K

Chemical formula		Pb_2MnWO_6
Super-space magnetic group		*$Pmc2_1(\alpha 00)0s0$*
a (Å)		8.01620(11)
b (Å)		5.78216(8)
c (Å)		11.63487(9)
V ($Å^3$)		541.10(16)
Z		4
	D2B	**D20**
λ(Å)	1.594	2.41
GOF	1.68	5.92
R_p	5.54%	2.28%
$_wR_p$	6.98%	3.26%
Overall GOF	3.41	
Overall R_p	2.37%	
Overall $_wR_p$	3.51%	

Table 5-4 Modulation functions for the magnetic moment of the manganese atoms

Site	**Magnetization expression**
Mn1	$M_{x,0}+ M_{y,c}\cos(2\pi x_4)+ M_{z,c}\cos(2\pi x_4)$
Mn2	$M_{x,0}+M_{y,c}\cos(2\pi x_4)+ M_{z,c}\cos(2\pi x_4)$

Owing to the presence in the diffraction pattern of the only first-order satellites, the symmetry permitted terms of the Fourier series, indicated in equation 1, was truncated at n=1. Moreover, further constraints, suggested by the behaviour of the refined parameters, were introduced in the last refinement cycles. On one side the $M_{x,s}$ terms, having negligible values within the e.s.d.'s, were imposed to zero, whereas the $M_{x,0}$ and $M_{z,c}$ terms of the two independent sites, having comparable opposite values, were forced to assume the same modulus and the opposite sign. The final terms of the modulation function are reported in table 5-4, whereas the atomic and magnetic parameters of the 2 K refinement are reported in table 5-5. Figure 5-15 shows the Rietveld plots of the

D2B and D20 data with both nuclear and magnetic contribution, whereas figure 5-16 shows the fit of the pure magnetic diffraction pattern obtained from the subtraction between the 2 K and 10 K D20 patterns. The agreement on the pure magnetic pattern is good ($_wR_B$=9%) and confirms the proposed model.

Table 5-5 Atoms positions and magnetic parameters of the structure at 2K

Site	x	y	z	U_{iso} (Å^2)
Pb1	0.7628(9)	0.9746(16)	0.8653(11)	0.015(2)
Pb2	0.7462(11)	0.5477(12)	0.5786(11)	0.011(2)
W1	0	0.522(4)	0.8644(12)	0.020(5)
W2	0.5	0.001(5)	0.6117(12)	0.018(5)
Mn1	0.5	0.492(6)	0.8646(16)	0.006(6)
Mn2	0	0.998(7)	0.1027(15)	0.011(6)
O1	0	0.724(3)	0.730(2)	0.0159(5)
O2	0	0.311(3)	0.973(2)	0.0159(5)
O3	0.5	0.767(4)	0.7103(18)	0.0159(5)
O4	0.5	0.222(3)	0.721(2)	0.0159(5)
O5	0	0.249(3)	0.7442(13)	0.0159(5)
O6	0.5	0.209(3)	0.477(3)	0.0159(5)
O7	0.7384(15)	0.0361(16)	0.5956(12)	0.0159(5)
O8	0.5	0.294(4)	0.9958(16)	0.0159(5)
O9	0.7667(15)	0.520(2)	0.8655(12)	0.0159(5)
O10	0	0.786(4)	0.9568(17)	0.0159(5)

Site	$M_{x,0}$ (μ_B)	$M_{y,c}$ (μ_B)	$M_{z,c}$ (μ_B)
Mn1	-2.31(3)	-3.26(15)	1.57(7)
Mn2	2.31(3)	5.06(13)	1.57(7)

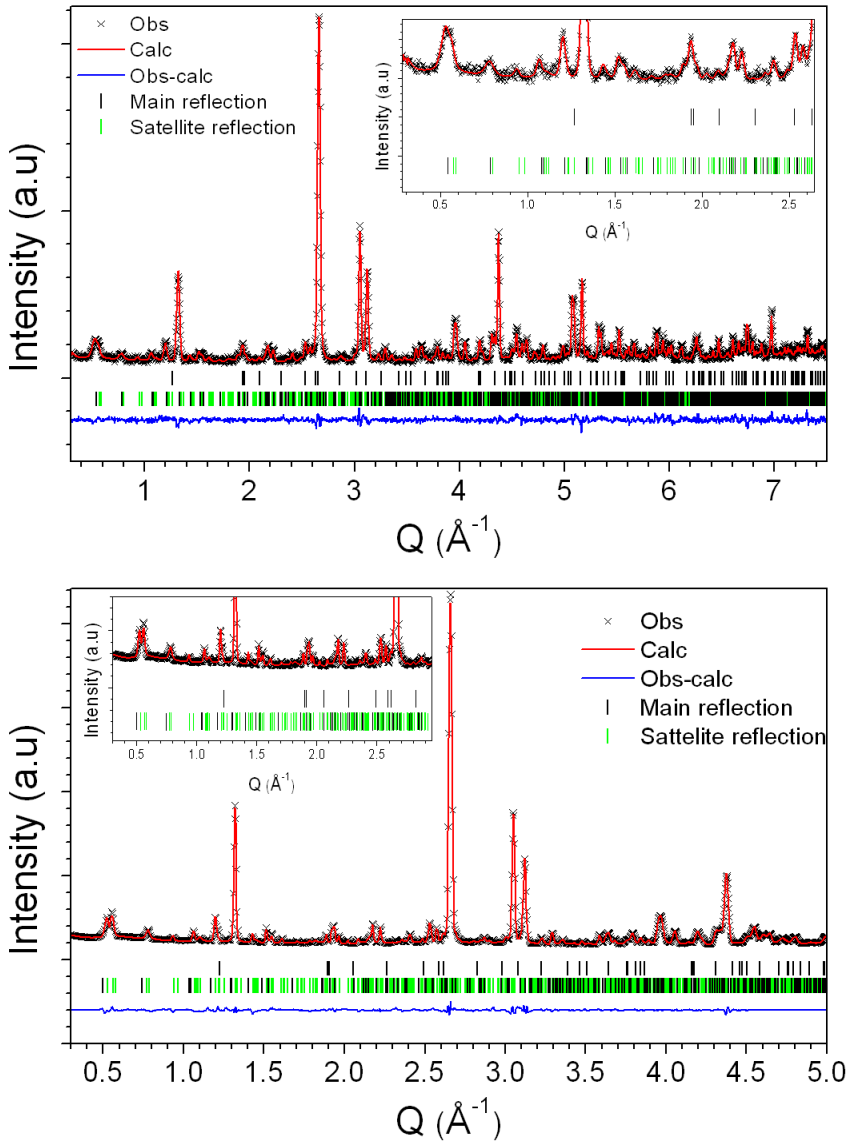

Figure 5-15 Rietveld refinement plots of the neutron powder diffraction data taken at 2 K on D20 (top) and D2B (bottom): observed (black crosses), calculated (red line) and difference (blue line) patterns are shown; the black tick marks indicate the calculated position of the main phase (bottom) and of the secondary phase $PbWO_4$ (top), whereas the green tick marks indicate the magnetic satellite reflections of the main phase.

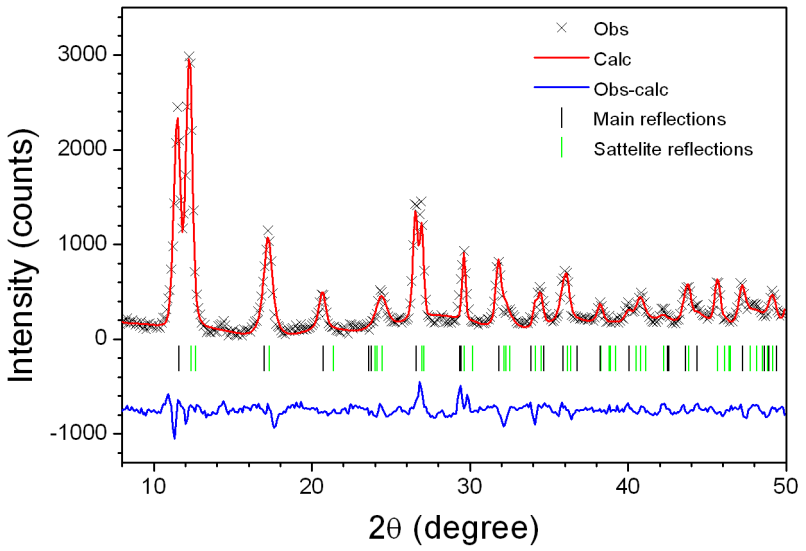

Figure 5-16) Rietveld refinement plot of the pure magnetic pattern obtained by the difference of the 2 and 10 K D20 diffraction patterns: observed (black crosses), calculated (red line) and difference (blue line) patterns are shown; the black tick marks indicate the calculated position of the main magnetic reflections, whereas the green tick marks indicate the magnetic satellite reflections.

As described in chapter 3, in the superspace formalism the reconstruction of the 3D structure is done by a t-section of the (3+1)D space perpendicular to the 3D space, recalling that the value of the magnetization along the forth axis is:

$$\vec{M}_{l,j} = \vec{M}_{l,j}(t + \vec{k} \cdot \vec{r}_{l,j}) \qquad (2$$

where t in case of a N_s-fold commensurate structure is $t = n/N_s - t_0$ (n=0,1,.., N_s-1).

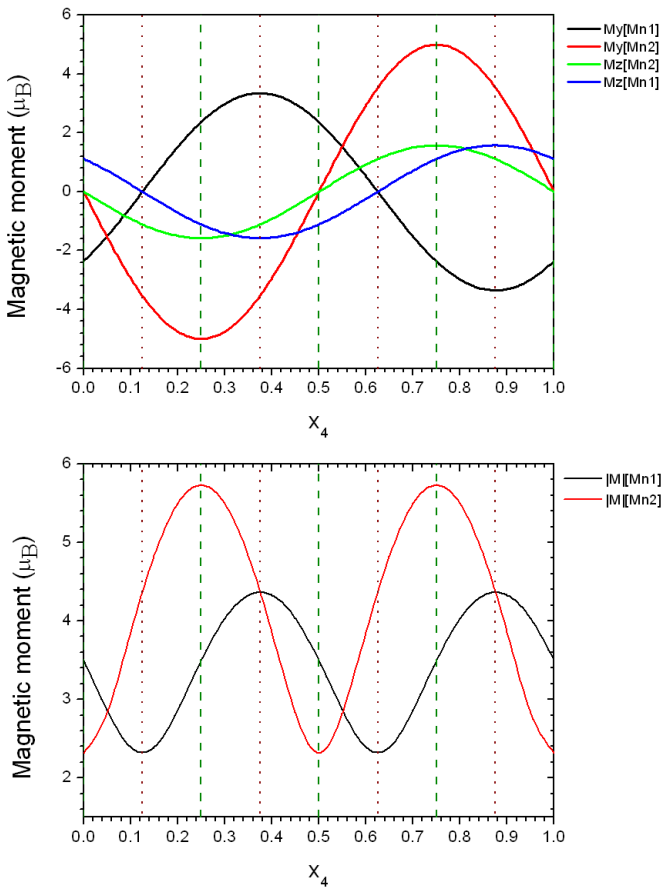

Figure 5-17 t-plot of the magnetic components (top) and of the moduli (bottom) of the two independent Mn atoms obtained from the refinement at 2 K. The dashed and the dotted lines represent the position of the manganese atoms with the different choice of the t-section respectively t_0=0 and 1/8. The position of the manganese atoms in the t-space are obtained by the relation $t_{l,j}=t_0+\boldsymbol{k}\bullet\boldsymbol{r}_{l,j}$

The choice of the origin of the t-section, the t_0 parameters, is a crucial point in case of a commensurate structure (see chapter 3). In fact, in this frame, different choices of the t_0 parameter can give different magnetic components and even different magnetic space groups for the N_s-fold superstructure. Among the possible t_0 sets, both the conditions $t_0=0+n/4$ and $t_0=⅛+n/4$ give rise to

superstructures with orthorhombic *Pmn2₁* magnetic symmetry whereas any other value of t_0, defines a superstructure with monoclinic *Pn* magnetic symmetry. Figure 5-17 shows the evolution of the magnetization along the fourth axis of the (3+1)D space whereas the positions of the Mn atoms with the two different choices of the t_0 parameters are indicated by the heavy and light dashed lines.

The solution with $t_0=0+n/4$ leads to a magnetic moment |M| = 5.73 μ_B, exceeding what expected for Mn^{2+} at 2 K, for two atoms and therefore it has been rejected. On the contrary $t_0=⅛+n/4$ represents the most convenient solution, not only for symmetry reasons, but also for the plausible values of the three unconstrained magnetic moments, that are similar to each other as shown in table 5-6.

Table 5-6 Value of the magnetic moment for each atoms in the fourfold superstructure with $t_0=1/8$. The atoms label, according to table 5-5, indicates the position in the nuclear unit cell.

Atom	x_4	M_x (μ_B)	M_y (μ_B)	M_z (μ_B)	|M| (μ_B)
Mn1	0	2.30(3)	0.000(0)	0.000(0)	2.30(3)
Mn1	0.25	2.30(3)	3.19(15)	-1.58(7)	4.24(17)
Mn1	0.5	2.30(3)	0.000(0)	0.000(0)	2.3063)
Mn1	0.75	2.30(3)	3.19(15)	1.58(7)	4.24(17)
Mn2	0	2.30(3)	-3.61(6)	1.11(5)	4.43(8)
Mn2	0.25	2.30(3)	3.61(6)	1.11(5)	4.43(8)
Mn2	0.5	2.30(3)	-3.61(6)	1.11(5)	4.43(8)
Mn2	0.75	2.30(3)	3.61(6)	1.11(5)	4.43(8)

The commensurate fourth-fold structure with *Pmc2₁* magnetic symmetry is shown in figure 5-18. The model is formed by blocks separated by mirror planes perpendicular to the ***a*** axis, producing the inversion of the M_y component sign; the manganese atoms lying on the mirror plane are constrained by the symmetry to assume magnetic moment collinear to the ***a*** axis. The magnetic interaction gives rise to zig-zag chains of FM alignments (blues straight lines) in the ***ac*** plane (see figure 5-18 bottom), which are stacked along the ***c*** axis with an E-type AF coupling (green straight lines giving rise to a perfect AF configuration).

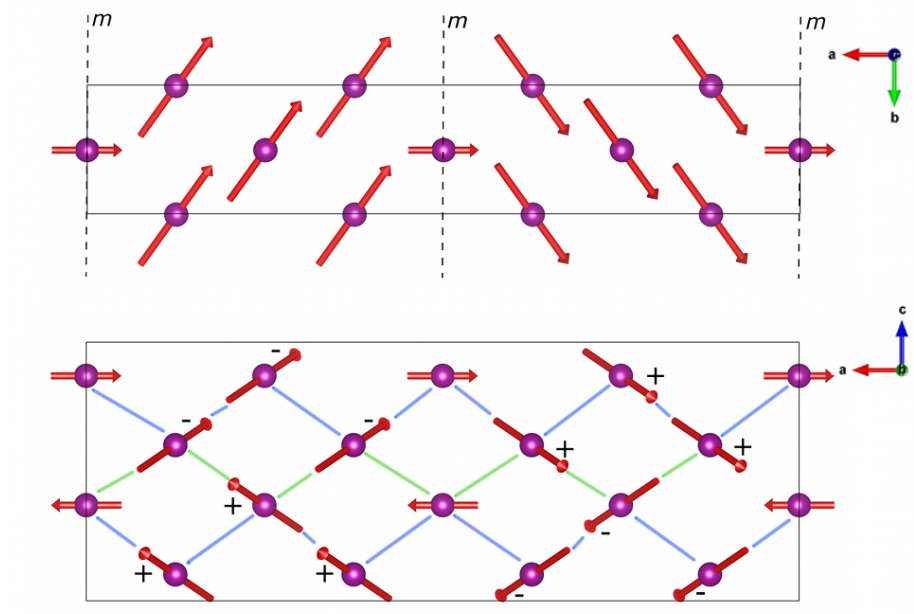

Figure 5-18 Projection of the refined magnetic model in the ***ab*** (top) and ***ac*** planes (bottom); the blue and green lines indicate ferromagnetic and antiferromagnetic interactions of the M_x components respectively; the + and - symbols indicate the direction of the magnetic moment component normal to the ***ac*** plane.

The evolution of the magnetic structure with the temperature is quite interesting. From figure 5-19, showing the evolution of the (001), (0011), and (101-1) reflections in the temperature range between 12 and 2 K, it can be noticed that the main magnetic reflections disappears before the satellites ones that vanish around 10 K in agreement with the magnetization measurements. Moreover the progressive shift of the satellite reflections suggest a reduction of the ***a*** component of the propagation vector from the commensurate value. To determine the evolution of the propagation vector as function of the temperature a series of Le Bail fit were performed on the D20 data. The result are summarized in the bottom panel of figure 5-19, were the deviation δ of the propagation vector κ_1 from the commensurate value is plotted as function of the

temperature. The propagation vector became clearly incommensurate above 7 K, temperature at which the magnetic intensity on the main reflections disappear, indicating the presence of a magnetic phase transition at this temperature.

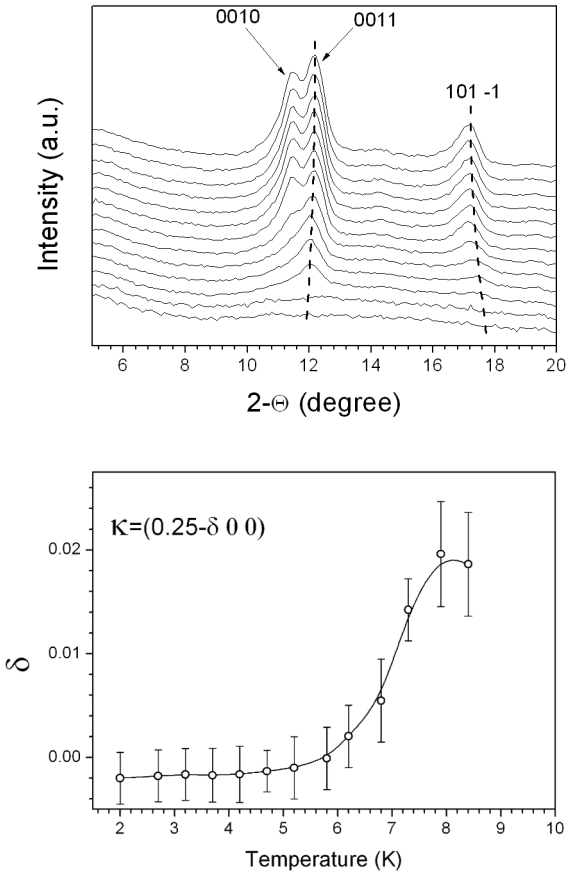

Figure 5-19 Top) Thermal evolution of selected magnetic reflections at low angle; the dashed lines are guides for the eyes to underline the different trend of the main and satellite reflections. Bottom) Thermal evolution of the propagation vector in terms of its deviation from the commensurate value.

The incommensurate magnetic structure was solved from the CW-NPD pattern collected at 8 K. Since the magnetic intensity on the nuclear reflection is zero the magnetic space groups of the basic magnetic structure is the grey group

Pmc2$_1$1'*. It follows that the possible magnetic superspace groups are *Pmc2$_1$1'(a00)0s0s or *Pmc2$_1$1'(a00)000s*. Owing to the limited number and to the weakness of the magnetic reflections, the Rietveld refinement was performed on the pure magnetic diffraction pattern obtained by the subtraction of the 13 K pattern from the 8 K one using the Jana2006 software.[4] The best agreement was found in the *Pmc2$_1$1'(a00)0s0s* superspace groups and the Rietveld plot is shown in figure 5-20, together with the resultant t-plot. Also in this case some constrains on the Fourier amplitudes of the two Mn sites were introduced in the last cycles to stabilize the refinement; in particular, by taking into account the obtained values the $M_{y,c}$ terms of the two independent sites were constrained in an AF configuration, whereas the $M_{z,c}$ terms were imposed to be equivalent. Refinement and magnetic parameters are summarized in table 5-7.

Table 5-7 Crystal data and refinement parameters of the incommensurate magnetic structure at 7.9K

Chemical formula	**Pb_2MnWO_6**
Super-space magnetic group	*Pmc2$_1$1'(α00)0s0s*
a (Å)	8.0206(8)
b (Å)	5.7813(8)
c (Å)	11.6316(18)
α	0.230(7)
V (Å^3)	539.36(16)
Z	4
GOF	1.67
R_P	8.97%
$_wR_P$	11%

Magnetic parameters	
$M_{y,c}$ (μ_B)	**$M_{z,c}$ (μ_B)**
2.11(5)	1.99(8)

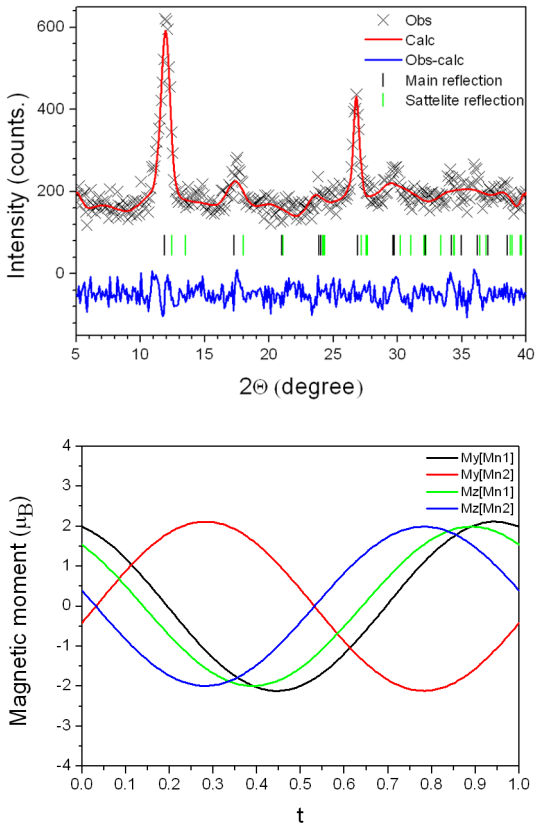

Figure 5-20 Top) Rietveld refinement of the incommensurate magnetic structure at 8 K on the pure magnetic diffraction pattern obtained from the subtraction between the 8 K and 13 K diffraction patterns. Bottom) t-plot of the incommensurate magnetic structure at 8 K.

In this case, thanks to the incommensurate character of the structure, any t-section give equivalent representation of the magnetic system. The obtained model in shown in figure 5-21; is constituted by a spin density wave propagating along the ***a*** axis with the spin lying in the ***bc*** plane.

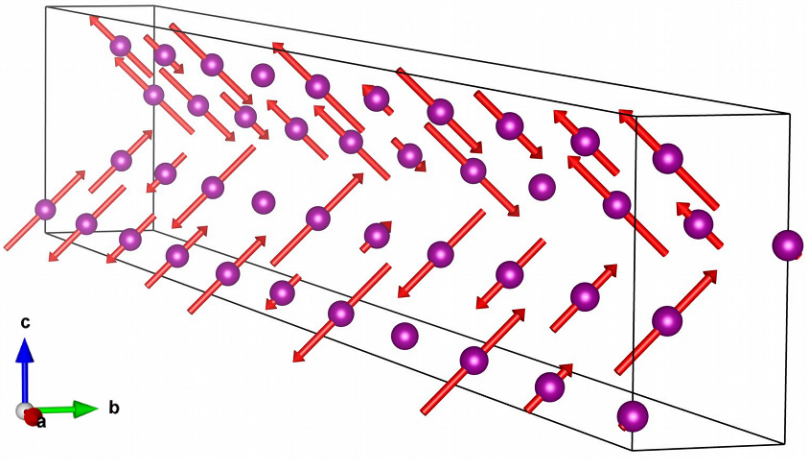

Figure 5-21 Representation of 10 unit cells of the incommensurate magnetic structure of PMW.

The acquired knowledge of the two magnetic structures allows to describe the evolution of the magnetic ordered moment as function of the temperature. The M_x component of the magnetic moment arises from the basic magnetic structure, whereas M_{yz}, calculated as $M_{yz} = \sqrt{M_{y,c}^2 + M_{z,c}^2}$, is connected to the modulated part of the magnetic structure. The data obtained from the two independent Mn sites were averaged and fitted with a classical power law:

$$M(T) = M_0 \left(1 - \frac{T}{T_c}\right)^{\beta} \quad (3$$

The fit of the experimental data is reported in figure 5-22, and it was extended also to total magnetic moment. The calculated value at 0 K, with a critical exponent β conform to the classical model of 3D Heisenberg magnet,[25] is in agreement with a Mn(II) in the *hs* configuration. It is worthy to underline that the equation 3 is correct for temperature close to the magnetic transition, nevertheless the obtained value of the magnetic moment at 0 K is a good approximation.

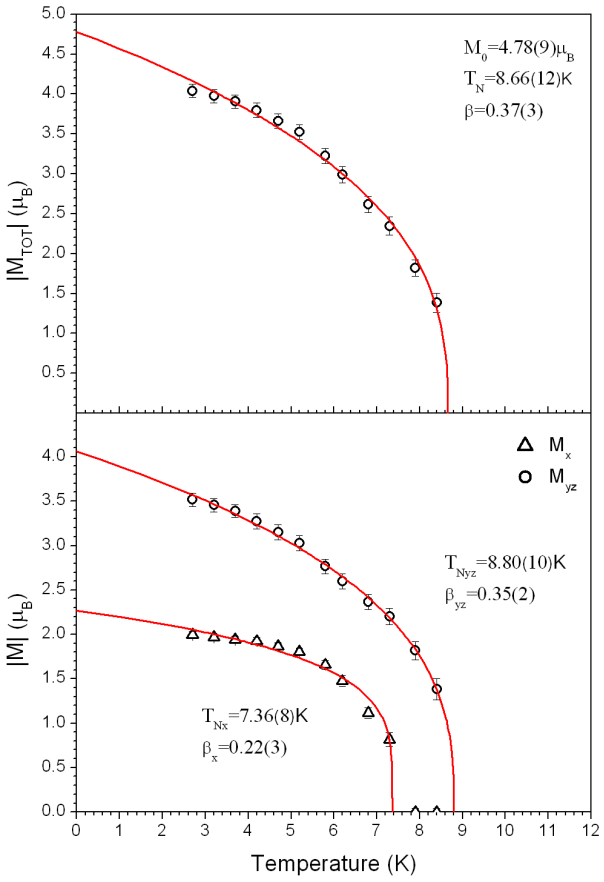

Figure 5-22 Thermal evolution of the magnetic moment of the Mn atoms as function of temperature. The red line is the best fit using the classical power law. (see text)

Below 10 K the long range magnetic order develops in the ***bc*** plane with an incommensurate propagation vector $\kappa_1 = (¼-\delta\ 0\ 0)$, superspace group *Pmc2₁1'(a00)0s0s*, and involve a spin density wave with the spin lying in the same plane. By further cooling, the propagation vector lock-in to the commensurate value at 7 K: the rise of the magnetic component along the ***a*** axis of the structure (see figure 5-22) with propagation vector $\kappa_2 = (000)$ is observed, and the magnetic superspace group of the commensurate structure transforms in *Pmc2₁(α00)0s0*. By analysing the symmetry of the two magnetic phases the

incommensurate-commensurate (IC-C) transition may be describe as the removing of the (1'|0 0 0 ½) symmetry operator, indicated in Seitz notation, from the *Pmc2$_1$1'(a00)0s0s* space group, and by the lock-in of the propagation vector to the commensurate value. It is worthy to underline that the lock-in of the propagation vector in the *Pmc2$_1$1'(a00)0s0s* superspace group does not imply the removal of the (1'|0 0 0 ½) symmetry operation, but is produced by the appearance of the κ_2= (0 0 0) component. The actual data cannot discriminate if the two phenomena happen simultaneously in a first order transition or are independent.

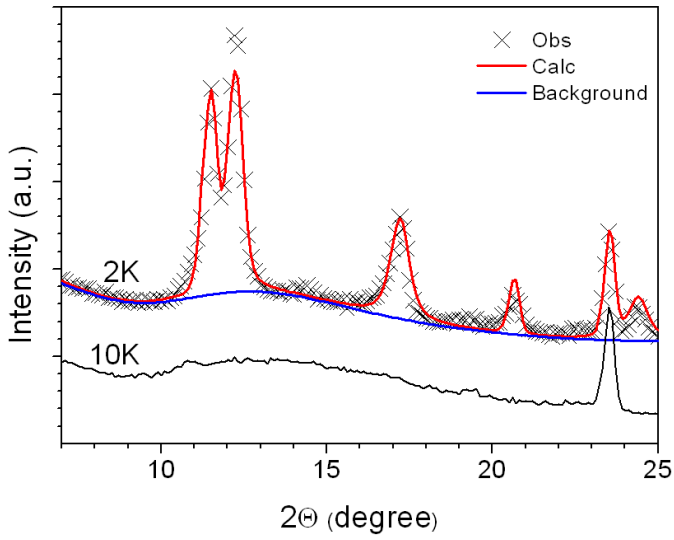

Figure 5-23 Zoom of the low angle region of the D20 Rietveld plot at 2 K. The blue line indicates the refined background that shows the same diffuse scatter seen in the diffraction pattern obtained at 10 K (shown for comparison).

It is interesting to note that the diffuse scattering appearing in connection with the first transition at T_1 = 44 K persists below the second magnetic transition, as pointed out in figure 5-23. This is a clear indication that the two phenomena, the long and short-range order, have a different nature. It is widely recognized in literature that point and line defect, like anti-site defect (AS) and

anti phase boundary (APB), deeply influence the magnetic proprieties of double perovskite systems.[26-29] The Rietveld refinement does not point out the presence of anti-site defect in the system, at least in the sensibility range offered by the diffraction techniques. The most plausible explanation of the diffuse scattering observed at the T_{C1} transition could be the presence in the polycrystalline sample of APB generating AF exchange paths with higher transition temperature but limited spatial distribution. The presence of this short-range order should be at the origin of the observed weak ferromagnetism, since the other possible option, i.e. canting of the long-range AF structure, is forbidden by the symmetry of both superspace groups, which do not allow a ferromagnetic component. In this scenario the APB generate AF domains that may be unbalanced owing to the reduced spatial extension, giving rise to a weak ferromagnetic contribution that reaches the saturation at low fields, but is masked by the linear response of the AF structure at higher applied fields (see figure 5-12).

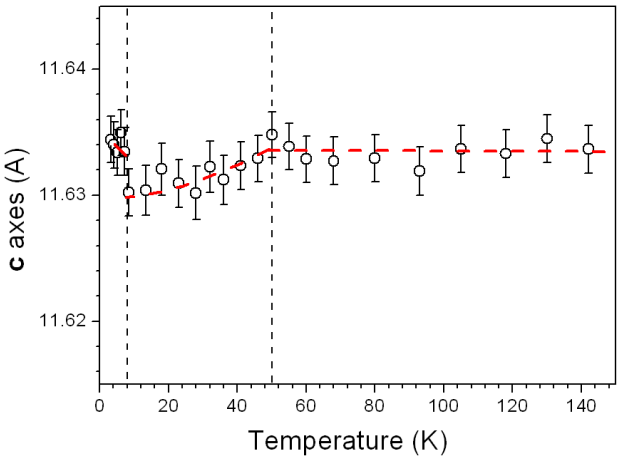

Figure 5-24 Thermal evolution of the low temperature region of the ***c*** axis of the structure. The dashed lines indicate the two magnetic transitions; the red line is a guide to the eye to underline the magnetostrictive effects.

Both the observed magnetic transition are connected to magnetostrictive effects, as indicated by the comparison of magnetization data with the thermal evolution of the polar axis ***c*** reported in figure 5-24. A weak magnetostrictive effect is observed in correspondence of T_{C1}, whereas a small jump at 10 K is detected in correspondence of the long-range magnetic ordering, as indication of a possible first order character of the transition. The correlation between the magnetic critical temperatures of the system and the anomalies observed in the cell parameters, particularly along the polar direction of the crystal (***c*** direction) are indications of a possible spin-lattice coupling in the system.

5.6 Poling effect on structural ad magnetic properties

In order to investigate the existence of a persisting effect of the application of a high electric field to the system, diffraction experiments were performed on a poled sample. A thin sintered sample (t = 200 μm) was metalized and poled at 2 kV in the same condition of the PUND measurement shown in figure 5-10. The poled sample was then used in a transmission diffraction experiment at the ID15B beam line (λ = 0.1427 Å) in the temperature range 2 - 300 K. In spite of the fact that the diffraction pattern does not show significant changes of the reflection intensities with respect to the un-poled sample, some new weak reflections rise up by cooling below 230 K as shown in figure 5-25. Even if these reflections are not present at room temperature, some diffuse scattering in the low angle region is observed, suggesting that domains of this nuclear modulation increase with the decreasing of the temperature.

The satellite reflections were indexed in the 4 K diffraction pattern with the use of the k-search software of the Fullprof suite[30] and the best R factor was obtained for the modulation vector κ=(0.44, 0.25, 0). It worthy to underline that the correct indexing of an incommensurate modulation vector with two components is tricky from powder data because of the strong superposition and overlap of the reflections. Nevertheless, the result of a Le-Bail fit of the 4 K data

with the proposed modulation vector performed with the Jana2006 software[4] is shown in figure 5-26. All the peaks in the diffraction pattern are indexed with the proposed model and the refined modulation vector is κ=(0.4388(2), 0.25, 0)

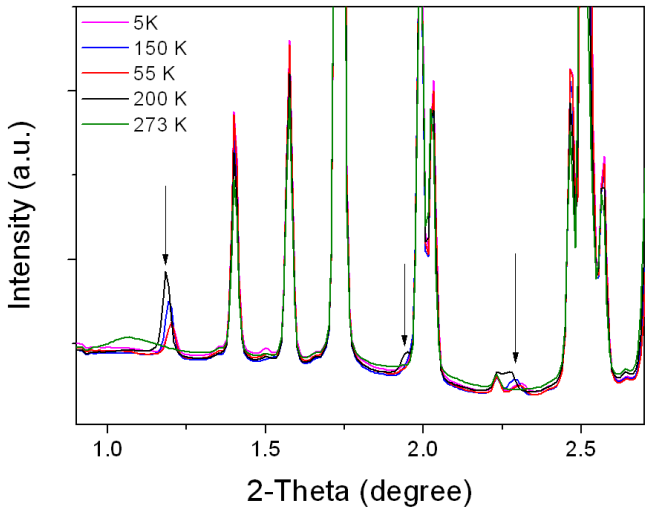

Figure 5-25 Selected low angle SPXRD patterns of the poled sample; the arrows indicate the satellite reflections arising below 230 K.

By considering the modulation vector and the space group of the parent structure, the possible superspace group for the modulated structure is $P2_1(\alpha\beta0)0$ (unique axis ***c***) corresponding to the V1 representation. Unfortunately, owing to the small number and to the weakness of intensity of the observed reflections and to the structure complexity (20 atoms in the asymmetric unit), it was not possible to obtain a plausible model for the incommensurate phase.

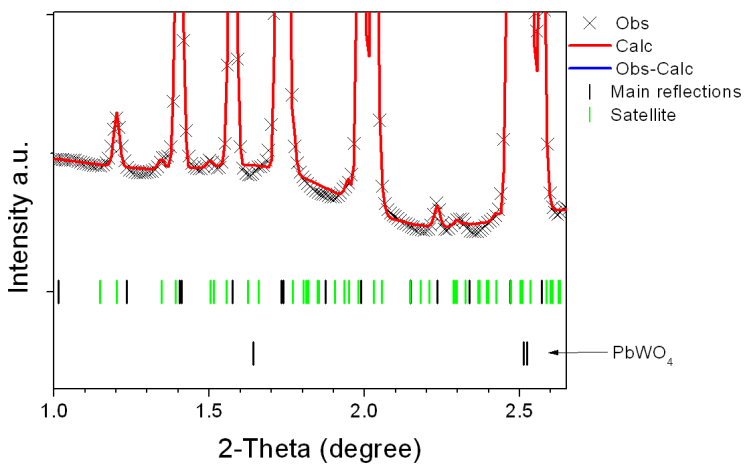

Figure 5-26 Le-Bail fit of the 4 K SPXRD pattern of the poled sample using the propagation vector κ=(0.4388(2), 0.25, 0). Observed (black, crosses), calculated (red, line), main (black, tick) and satellite (green, tick) reflections are shown.

The thermal behaviour of the average structure, expressed in terms of the fundamental perovskite cell and of the unit cell volume, is reported in figure 5-27. By comparison with the measurements carried out on the un-poled sample and shown in figure 5-6, strong differences can be noted. $\boldsymbol{b_p}$ and $\boldsymbol{c_p}$ at first increase and then decrease by decreasing T, showing both a maximum around 150 K. An opposite trend is observed for $\boldsymbol{a_p}$; at first it decreases significantly, determining the contraction of the unit cell volume in spite of the opposite trend of $\boldsymbol{b_p}$ and $\boldsymbol{c_p}$; then, below 150 K, the expansion coefficient at first decreases progressively and then changes sign at 80 K; below this temperature, $\boldsymbol{a_p}$ increases but the thermal trend is again upturned at 10 K. The complexity of the $\boldsymbol{a_p}$ behaviour contrast with the one of the un-poled sample, where only a freezing of the cell parameter was observed. It is interesting to note that all the lattice parameters of the poled sample show anomalies at 10 K, in correspondence to the magnetic long-range order transition. The magnetostrictive effect observed at T_{C2} = 44 K in the un-poled sample, seems translated in the poled one at a higher temperature (around 100 K).

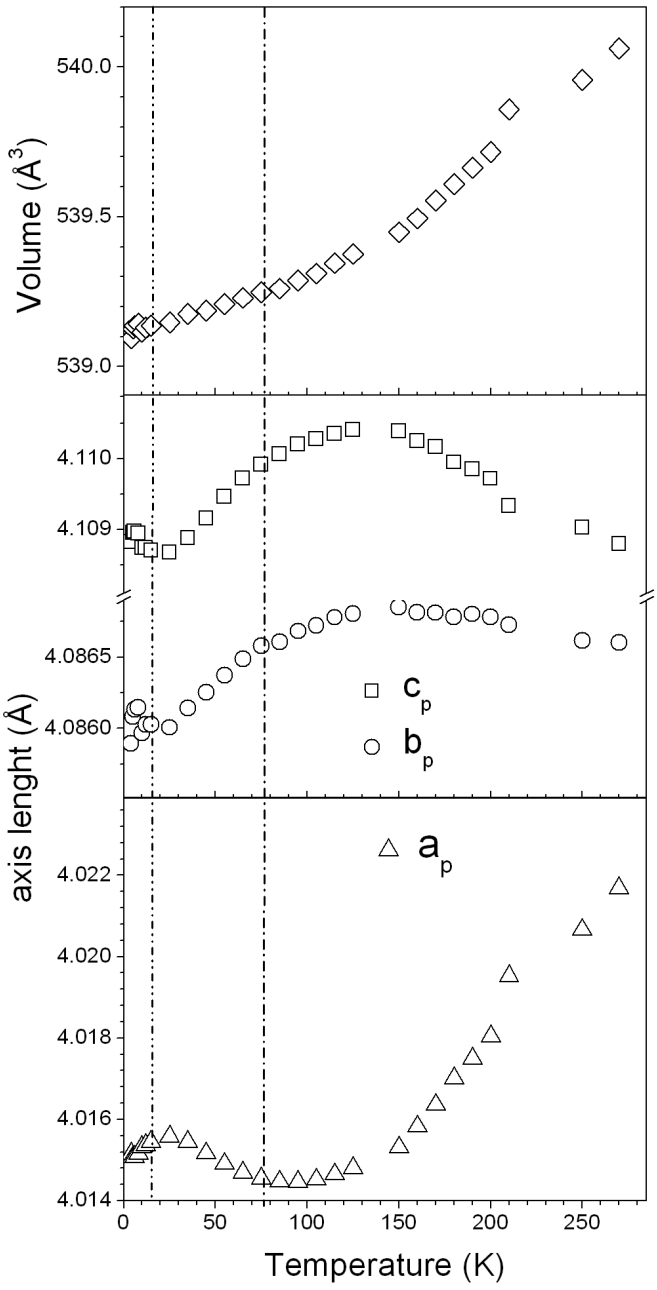

Figure 5-27 Thermal evolution of cell volume and cell parameters (expressed in terms of the fundamental perovskite cell) of the poled PMW sample; the dash-dot-dot line indicates the long-range magnetic transition temperature, whereas the dash-dot line indicates the upturning of the a_p thermal coefficient.

The observed anomalies for the poled sample seem in general to be related to the electric and magnetic characteristics of the system. First of all, the change in the thermal expansion coefficient of the ***bc*** plane observed around 170 K could be connected to the change in the transport properties of the sample at this temperature and in particular to the jump in the dielectric constant, the change in the resistivity mechanism and the strong pyrocurrent peak.

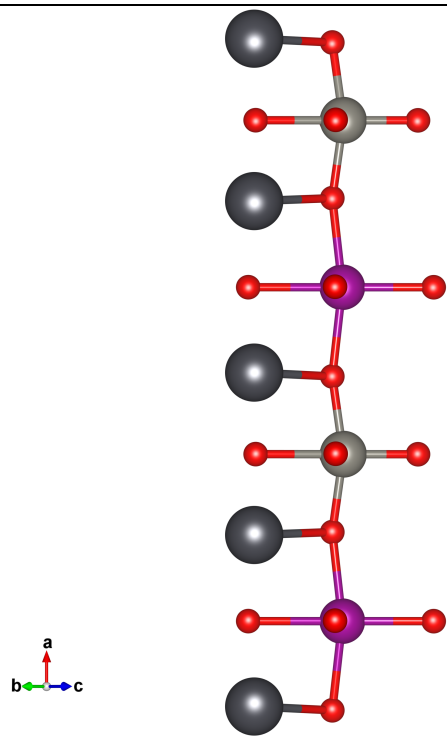

Figure 5-28 View of the O-B-O-B' chain along the ***a*** axis; violet and grey atoms refer to Mn and W, large black sphere to lead, wheres the oxygen atoms are represented in red. The connection between the O-B-O angle and the shortest bond of the lead atoms with the apical oxygen, indicated in figure, is evident.

The most interesting temperature of the poled systems is the anomaly observed in the thermal evolution of the ***a*** axis at 80 K. At this temperature in the pyrocurrent measurements is present a broad peak as shown in figure 5-11a indicating a contribution of the transition in the sample polarization. As already

point out the ***a*** direction is principally characterized by the bending of the O-B-O angle of the octahedral network, mainly caused by the distortion induced by the lead atoms as described in figure 5-28. Starting from RT and cooling the sample, the ***a*** direction start to decrease until to 100 K, where it reaches the lowest value and consequently the O-B-O angle reaches is lowest limit. By further cooling the sample, the structure relax the compression with a consequent increase of the ***a*** axis. These effects are evidenced also in the thermal evolution of the ***b*** and ***c*** axes; starting from RT and by cooling the sample, the lead distortion increases inducing an expansion of the ***bc*** plane as observed in correspondence of the para-ferrielectric transition at 450 K in the un-poled sample. At 100 K the lead distortion rich is maximum value and starts to decrease, and consequently the ***bc*** plane starts to compress and follow a classical behaviour by decreasing the temperature. Finally, the lead distortion seems to increase again below the magnetic transition at 10 K, as indicated by the sudden increase of the polar axis of the structure (figure 5-27) connected to the shortening of ***a*** .

The temperature dependence of the integrated intensities of selected reflections is shown in figure 5-29. The main reflections, connected to the average nuclear structure, follow a classical behaviour (increase the intensity by decreasing the temperature produced by the ADP's reduction). On the contrary, the intensities of the satellite reflections, after an initial rise by decreasing T, decrease monotonically below 230 K down to 80 K, where they start to rise again. The correspondence of these temperaturse with the changes in the thermal behaviour of the ***a*** axis, is a clear indication of a strict. Finally, it is worthy to underline the appearance of the satellite reflections at the temperature (T_2 = 217 K) at which a broad peak in the pyrocurrent is observed (figure 5-11a) suggesting the influence of the modulation on the ferrielectric properties of the system.

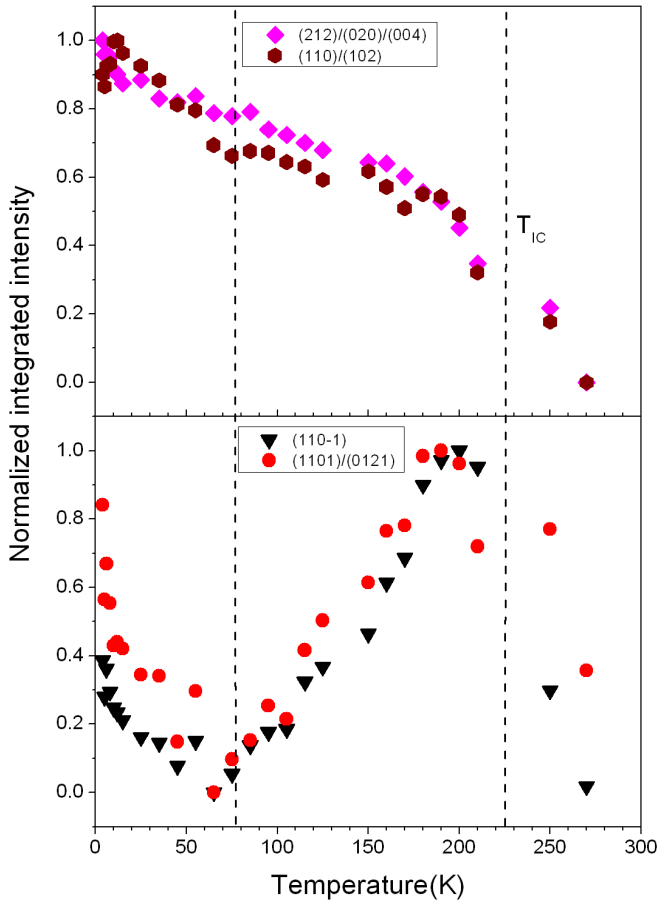

Figure 5-29 Integrated intensities of selected main (top) and satellite (bottom) reflections, indexed on the basis of the modulation vector determined at 4K. The dot lines indicate the appearing of the satellite reflection at 230 K and the change of the thermal coefficient of the ***a*** axis at 80 K.

To better correlate these new features of the system and to study the possible magneto-electric coupling, a series of Electric Field cooling magnetization measurement were performed on the poled sample. In figure 5-30(top) are shown the FCC and ZFC measurements of the poled sample performed without applying electric filed during the cooling of the sample, that

point out several differences with respect to the same measurements on the unpoled sample.

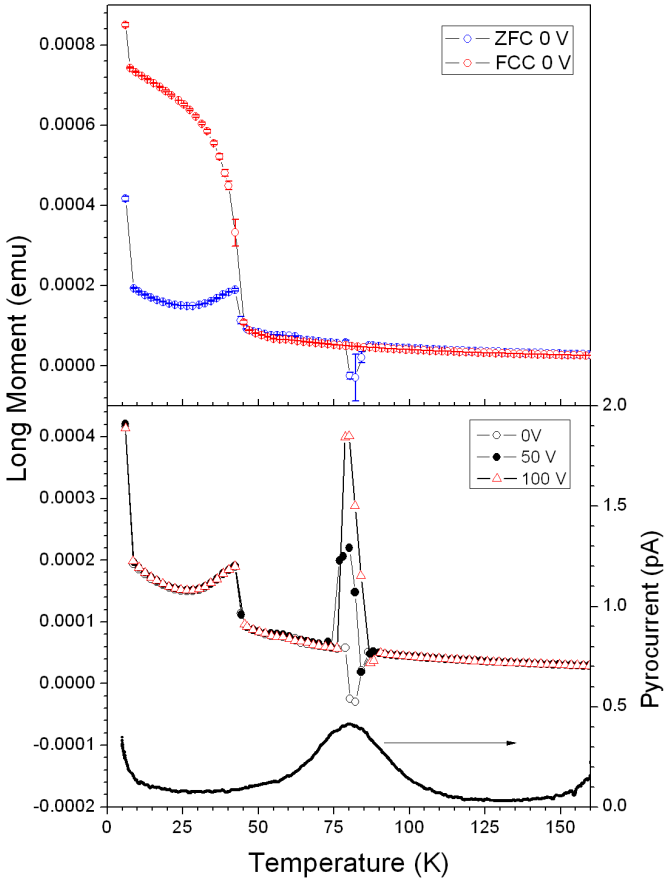

Figure 5-30 (Top) Electric Field cooling FCC and ZFC magnetization measurements on a thin (t = 200 µm) metalized PMW sample after 2 kV poling. (Bottom, left axis) Electric Field cooling ZFC magnetization measurements at different electric field showing the strong field dependence of the magnetization cusp observed at 80 K. (Bottom, rigth axis); pyrocurrent measurement showing a broad peak in correspondence of the magnetization cusp.

First, the two characteristic transition temperatures T_{C1} and T_{C2} are still present at the same temperatures, but they look more sharp than in figure 5-12.

Since the two measurements are performed on samples sintered for different time, they could be influenced by differences in microstructure, morphology, density and defects. Nevertheless, in the ZFC measurement, a strong anomaly with a small negative cusp (quenched in the FCC measurement) is evident around 80 K. As shown in figure 5-30 (bottom), this cusp shows a very interesting electric field dependence. In fact, if the measurement is performed with an applied electric field, the cusp increases almost linearly with the field, becoming positive above 50 V, indicating a strong spin lattice coupling in the system.

The nature of the observed magnetization cusp is actually far to be understood and a series of measurements are planned to better analyse the coupling. This type of cusp in the magnetization measurements is generally connected with the Hopkinson effect.[31] This effect is related to the motion of the domain walls that, in soft materials, became fast in proximity of the transition temperature. This can induce a sharp increase of the magnetization in the sample as observed in quadruple perovskites.[32] Another possible explanation for the Hopkinson effect, in particular for single domain particles, takes into account the magneto-crystalline anisotropy constant K_a and the magneto-elastic effect K_{me}.[33-34] In specific, the magnetization cusp is present when the K constants go to zero just before or at the magnetic transition temperature. The vanishing of the anisotropy terms close to the magnetic transition allow the thermal energy to change the direction of the magnetization from an easy direction to the other and consequently increase the system susceptibility. In the present case, the nature of the observed effect is difficult to attribute; nevertheless some consideration could be done. First, it is evident that whatever could be the cause of the observed cusp, it is strongly related to the ferrielectric degree of freedom of the system, since on one side the cusp intensity changes with the applied electric field and on the other a broad peak was observed at the same temperature in the pyrocurrent measurement. Moreover, a change of the thermal coefficient of the ***a*** axis, indicating a sort of inverse magneto-striction effect, is present at the same

temperature. In this picture, since the concerned direction is strongly related to the O-B-O angles and consequently to the crystal field acting on the magnetic atoms, we can imagine that the sudden change could be related to a change in the crystal field anisotropy of the system. The electric field dependence is easily explained by the influence of the ferrielectric arrangement of the lead atoms on the distortion of the oxygen sublattice.

The explanation of the Hopkinson effect in terms of anisotropy and magneto-elastic effect is based on the assumption of single domain particles non-or slightly interacting. It is reasonable to think that the anti-phase boundary regions, which are responsible of the short-range order in the sample, could be sufficiently far from each other to be considered as slightly interacting Clearly, further characterizations are needed to confirm this hypothesis .

5.7 Conclusions

PMW can be considered as a new type of multiferroic material, showing the presence of ferrielectric and antiferromagnetic ordering. The complete electrical characterization confirms the structural claim of ferrielectricity, formulated on the basis of uncompensated distortions of two lead sublattices coupled in an antiferroelectric way. The driving force of the distortion is the stereoactive lone-pair character of the Pb atoms that influences also the octahedral framework of the B site atoms. From the magnetic point of view, the system presents a AF structure, showing at 7K an incommensurate-commensurate transition leading to a propagation vector κ_1=(¼ 0 0) and to the superspace group *Pmc2$_1$(α00)0s0*. A strong spin-lattice coupling in the system via magneto-striction effect has been pointed out by the analysis of the cell parameters, showing anomalies in connection with the observed electric and magnetic phenomena. A series of measurements were performed on a poled sample, indicating a strong increase of the magneto-striction effects. Furthermore, SPXRD patterns showed that the electric poling induces the

appearing, below 230 K, of incommensurate satellite reflections; unfortunately, the small number and the weakness of satellite reflections prevented to solve the modulated structure. The poling also induces an electric field dependent cusp in the magnetization measurement at 80 K, pointing out the correspondence with the T_1 peak observed in the pyrocurrent measurements even for the un-poled sample. The cusp was tentatively explained by Hopkinson effect in terms of anisotropy and magneto-elastic effect enhanced by the electric poling.

5.8 Reference

[1] Orlandi F.; Righi L.; Cabassi R.; Delmonte D.; Pernechele C.; Bolzoni F.; Mezzadri F.; Solzi M.; Merlini M. and Calestani G. "*Structural and Electric Evidence of Ferrielectric State in Pb_2MnWO_6 Double Perovskite System*" Inorg. Chem. (2014) 53, 10283−10290.

[2] Blasco,J.; Merino,R.I.; García,J.; Sańchez,M.C. *"Properties and phase transition of the ordered perovskite Pb_2MnWO_6*" J.Phys.: Condens. Matter (2006), 18, 2261−2271.

[3] Burla, M. C.; Caliandro, R.; Camalli, M.; Carrozzini, B.; Cascarano, G. L.; Giacovazzo, C.; Mallamo, M.; Mazzone, A.; Polidori, G.; Spagna, R. "*SIR2011: a new package for crystal structure determination and refinement*" J. Appl. Crystallogr. (2012), 45, 357−361.

[4] Petricek, V.; Dusek, M.; Palatinus, L. "*Crystallographic Computing System JANA2006: General features*" Z. Kristallogr. (2014), 229, 345– 352

[5] Nespolo, M.; Ferraris, G.; Ohashi, H. "*Charge distribution as a tool to investigate structural details: meaning and application to pyroxenes*" Acta Crystallogr. (1999), B55, 902−916.

[6] Walsh, A.; Payne, D. J.; Egdellb, R. G.; Watsonc, G. W. "*Stereochemistry of post-transition metal oxides: revision of the classical lone pair model*" Chem. Soc. Rev. (2011), 40, 4455−4463.

[7] Halasyamani, P. S. "*Asymmetric Cation Coordination in Oxide Materials: Influence of Lone-Pair Cations on the Intra-octahedral Distortion in d^0 Transition Metals*" Chem. Mater. (2004), 16, 3586– 3592.

[8] Bersuker, I. B. "*Pseudo Jahn-Teller origin of perovskite multiferroics, magnetic-ferroelectric crossover, and magnetoelectric effects: the d^0-d^{10} problem*" Phys. Rev. Lett. 2012, 108, 137202.

[9] Subías, G.; Blasco, J.; García, J.; Herrero-Martín, J.; Sánchez, M. C. "*Order-disorder nature of the antiferroelectric transition in Pb_2MnWO_6*" Phys. Condens. Matter (2009), 21, 075903.

[10] Scott J F, Kammerdiner L, Parris M, Traynor S, Ottenbacher V, Shawabkeh A and Oliver W F "*Switching kinetics of lead zirconate titanate submicron thin‐film memories*" J. Appl. Phys. (1988) 64 787.

[11] Shmidt, N.A. "*Coercive force and 90° domain wall motion in ferroelectric PLZT ceramics with square hysteresis loops*" Ferroelectrics 1981, 31, 105-111.

[11] Pulvari, C. F. "*Ferrielectricity*" Phys. Rev. (1960), 120, 1670.

[12] Pulvari, C. F.; de la Paz, A. S. "*Phenomenological theory of polarization reversal in ferrielectric $Bi_4Ti_3O_{12}$ single crystals*" J. Appl. Phys. (1966), 37, 1754– 1763.

[13] Muller, P. " *Phys. Status Solidi A*" (1981), 67, 11– 60.

[14] Bucci, C.; Fieschi, R.; Guidi, G. "*Ionic thermocurrents in dielectrics*" Phys. Rev. (1966), 148, 816– 823.

[15] Riva, S. C.; Bucci, C. A. "*Evidence for space charge polarization in pure KC1 at low temperatures*" J. Phys. Chem. Solids (1965), 26, 363– 371.

[16] Warren, B. E. "*X-Ray Diffraction in Random Layer Lattices*" *Phys. Rev.* (1941), 59, 693.

[17] Janner, A; Janssen, T. "*Symmetry of incommensurate crystal phases. I. Commensurate basic structures*" Acta Cryst. 1980, A36, 399.

[18] Perez-Mato, J.M.; Ribeiro, J. L.; Petricek, V.; Aroyo, M. I. "*Magnetic superspace groups and symmetry constraints in incommensurate magnetic phases*" J. Phys.: Condens. Matter 2012, 24, 163201.

[19] Petrícek, V.; Fuksa, J.; Dusek, M. "*Magnetic space and superspace groups, representation analysis: competing or friendly concepts*?" Acta Cryst. 2010, A66, 649.

[20] Litvin, D.B. "*Tables of crystallographic properties of magnetic space groups*" Acta Cryst. (2008), A64, 419.

[21] Aroyo, M. I.; Perez-Mato, J. M.; Orobengoa, D.; Tasci, E.; de la Flor, G.; Kirov, A. "*Crystallography online: Bilbao Crystallographic Server*" Bulg. Chem. Commun. 2011, 43(2), 183.

[22] Aroyo, M. I.; Perez-Mato, J. M.; Capillas, C.; Kroumova, E.; Ivantchev, S.; Madariaga, G.; Kirov, A.; Wondratschek, H. "*Bilbao Crystallographic Server I: Databases and crystallographic computing programs*" Z. Krist. 2006 221, 15.

[23] Aroyo, M. I.; Kirov, A.; Capillas, C.; Perez-Mato, J. M.; Wondratschek, H. "*Bilbao Crystallographic Server II: Representations of crystallographic point groups and space groups*" Acta Cryst. 2006, A62, 115.

[24] Gallego, S. V.; Tasci, E. S.; de la Flor, G.; Perez-Mato, J. M.; Aroyo, M. I. "*Magnetic symmetry in the Bilbao Crystallographic Server: a computer program to provide systematic absences of magnetic neutron diffraction*" J. Appl. Cryst. 2012, 45, 1236.

[25] Holm, C. and Janke, W. "*Critical exponents of the classical three-dimensional Heisenberg model: A single-cluster Monte Carlo study*" Phys Rev B, 1993, 48, 936.

[26] Mandal T. K., Abakumov A. M., Lobanov M. V., Croft M. , Poltavets V. V. and Greenblatt M. "*Synthesis, Structure, and Magnetic Properties of $SrLaMnSbO_6$: A New B-Site Ordered Double Perovskite*" Chem. Mater. (2008), 20, 4653-4660.

[27] Blanco M. C., De Paoli J. M., Ceppi S., Tirao G., Nassif V. M., Guimpel J. and Carbonio R. E *"Synthesis, structural characterization and magnetic properties of the monoclinic ordered double perovskites $BaLaMSbO_6$, with M = Mn, Co and Ni*" J. of Alloys and Compounds (2014), 606, 139-148.

[28] Dass, R. I.; Goodenough, J. B. "*Multiple magnetic phases of $La_2CoMnO_{6-\delta}$ $(0<\sim\delta<\sim0.05)$"* Phys. Rev. B 2003, 67, 014401.

[29] Goodenough, J.B.; Dass R.I. "*Comment on the magnetic properties of the system $Sr_{2-x}Ca_xFeMoO_6$, $0\leq x\leq 2$*" Int. J. Inorg. Mater. 2000, 2, 3.

[30] Rodríguez-Carvajal J. *"Recent Advances in Magnetic Structure Determination by Neutron Powder Diffraction"* Physica B, (1993), 192, 55-69

[31] Hopkinson, J. "*Magnetic properties of alloys of Iron an Nickel*" Proc. R. Soc. London 48 (1890), 1.

[32] Locherer T., Dinnebier R., Kremer R.K., Greenblatt M. and Jansen M. *"Synthesis and properties of a new quadruple perovskite: A-site ordered* $PbMn_3Mn_4O_{12}$" J. Solid State Chem. (2012), 190, 277–284.

[33] Slàma J., Soka M., Gruskovà A., Gonzalez A., and Jancàrik V. "*Hopkinson effect study in spinel and hexagonal ferrites*" Journal of Electr. Eng. (2011), 62, 239–243.

[34] Zhukova V., Ipatov M., Talaat A., and Zhukov A. "*Hopkinson effect in Co-rich glass-coated microwires*" Phys. Status Solidi C, (2014),1, 3.

6 $Pb_2Mn_{0.6}Co_{0.4}WO_6$ (PMCW_50)

6.1 Room temperature crystal structure

PMCW_50 sample was prepared starting from an equimolar Mn/Co ratio. The PXRD patter of can be index with a perovskite superstructure related to the simple perovskite by the relation $\boldsymbol{a} = 2\boldsymbol{a}_p$, $\boldsymbol{b} = \sqrt{2}\boldsymbol{a}_p$, and $\boldsymbol{c} = 2\sqrt{2}\boldsymbol{a}_p$; a minor impurity phase, present at 4.5% in weight, was detected and identified as lead tungstate. The superstructure was confirmed by electron diffraction and SAED measurements taken in [100] and [010] zone axes are reported in figure 6-1, where the reflections are indexed according to the orthorhombic superstructure and no extra modulation reflections are present.

The crystal structure at RT was solved and refined from SPXRD collected at the ID15B beam line and from ToF-NPD collected at WISH. The best solution was found in the centrosymmetric *Pmcn* space group (standard setting *Pnma*). The refinement in the non-centrosymmetric $Pmc2_1$ space groups, characteristic of the PMW compound,[1] didn't improve the fit. The structure was refined simultaneously on the WISH instrument banks with 2θ=152.8°, 121.6°, 90° and on the ID15B SPXRD data using the Jana2006 software.[2] The Rietveld plots of the 90° NPD data of WISH and of the SPXRD data are reported, as

examples, in figure 6-2, whereas crystal data, refinement parameters and atomic parameters are reported in table 6-1 and 6-2 respectively.

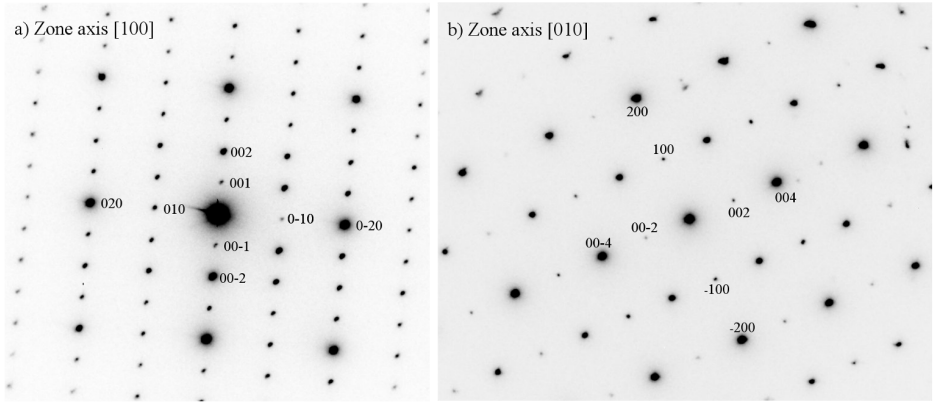

Figure 6-16 SAED patterns taken on PMCW_50, indexed accordingly to the superstructure $\boldsymbol{a} = 2\boldsymbol{a_p}$, $\boldsymbol{b} = \sqrt{2}\boldsymbol{a_p}$, and $\boldsymbol{c} = 2\sqrt{2}\boldsymbol{a_p}$ where $\mathbf{a_p} \approx 3.9$ Å is the fundamental perovskite cell parameter.

The refined structure represents the classical prototype of an ordered orthorhombic double perovskite, like Pb_2MgWO_6.[3] The B site results completely ordered in a NaCl-type arrangement and no anti-site defect was detected in the refinement. Despite this, the occupancy of the Mn/Co site deviates significantly from the expected 0.5/0.5 values indicating that the obtained phase is rich in Mn and its chemical formula, based on the diffraction data, can be expressed as $Pb_2Mn_{0.6}Co_{0.4}WO_6$. The missing cobalt is likely enclosed in the tungstate impurity, but the presence of a small amount of CoO, not detectable by diffraction measurement, cannot be excluded. The refined average bond lengths are in agreement with the expected values for Pb^{2+}, W^{6+} ions, as well as for Co^{2+} and Mn^{2+} in high spin (*hs)* configuration. Selected angles and bond lengths are reported in table A-2 in appendix. Charge distribution analysis performed with the CHARDIS99 software[4] return plausible oxidation state values for the cations in the system, in particular 2.02 for the Mn/Co site, 5.93 for W and 2.03 for Pb.

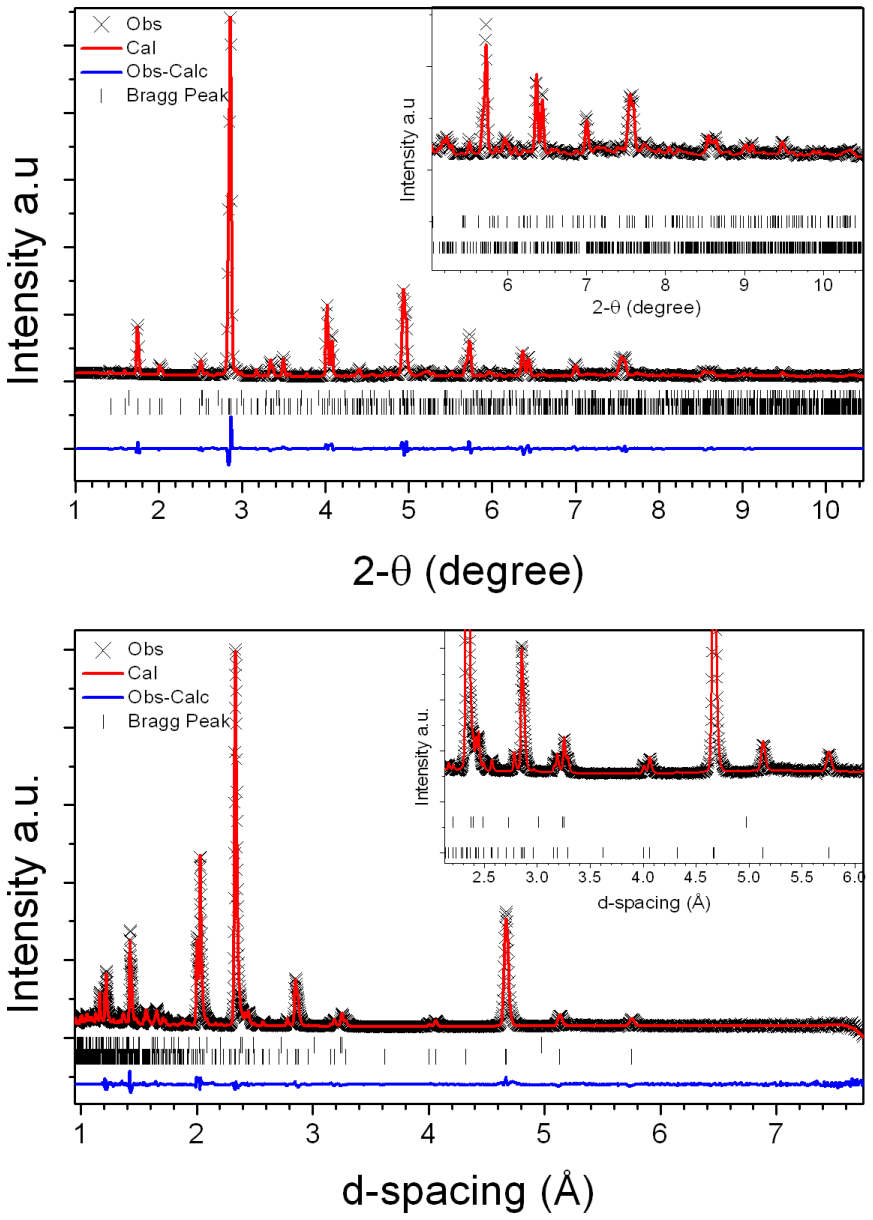

Figure 6-2 Rietveld plots of PMCW_50 data: SPXRD data (Top) and 90° bank of the WISH beam line (bottom). Observed (×, black), calculated (line, red), and difference (line, blue) patterns are reported. Upper tick marks indicate the Bragg positions of the lead tungstate impurity, and the lower tick marks the ones of the main PMCW_50 phase.

Table 6-1 Crystal data and refinement reliability factors for PMCW_50.

Chemical Formula	$Pb_2Mn_{0.6}Co_{0.4}WO_6$
Z	4
Space Group	*Pmcn*
a(Å)	8.01546(8)
b(Å)	5.73574(8)
c(Å)	11.51064(18)
Volume(Å^3)	529.197(12)
d (g cm^{-3})	9.42

	WISH 2θ=152.827°	**WISH 2θ=121.66°**	**WISH 2θ=90°**	**SPXRD λ=0.142Å**	**Overall**
Gof	3.13	2.76	2.46	3.99	2.93
R(F)obs	3.27	2.77	3.22	3.91	-
Rp	3.61	3.40	3.61	5.30	5.11
wRp	4.66	4.23	3.96	7.11	4.61

Table 6-2 Fractional atomic coordinates, atomic displacement parameters and occupancy factor of the PMCW_50 sample.

	x	**y**	**z**	**Occupancy**	**U_{iso} (Å^2)**
Pb	0.0061(3)	0.2773(3)	0.13717(9)	1	0.0260(4)
W	0.25	0.7544(7)	0.1200(3)	1	0.0063(5)
Mn	0.25	0.254(2)	-0.1227(9)	0.61(1)	0.0021(12)
Co	0.25	0.254(2)	-0.1227(9)	0.39(1)	0.0021(12)
O1	0.0089(2)	0.7339(6)	0.1319(2)	1	0.0438(8)
O2	0.25	-0.0196(15)	0.0157(5)	1	0.0352(15)
O3	0.25	0.5117(17)	-0.0022(5)	1	0.0285(11)
O4	0.25	-0.0333(13)	0.2542(5)	1	0.0194(19)
O5	0.25	0.4910(15)	0.2356(5)	1	0.044(2)

Although distorted from the stereoactivity of the lead atoms, the BO_6 octahedral framework does not show evident tilting. The asymmetric coordination of the lead atoms, resulting in short bonds (ranging from 2.571(5) to 2.672(3) Å) opposite to the lone pair, [5] is reported Figure 6-3b.

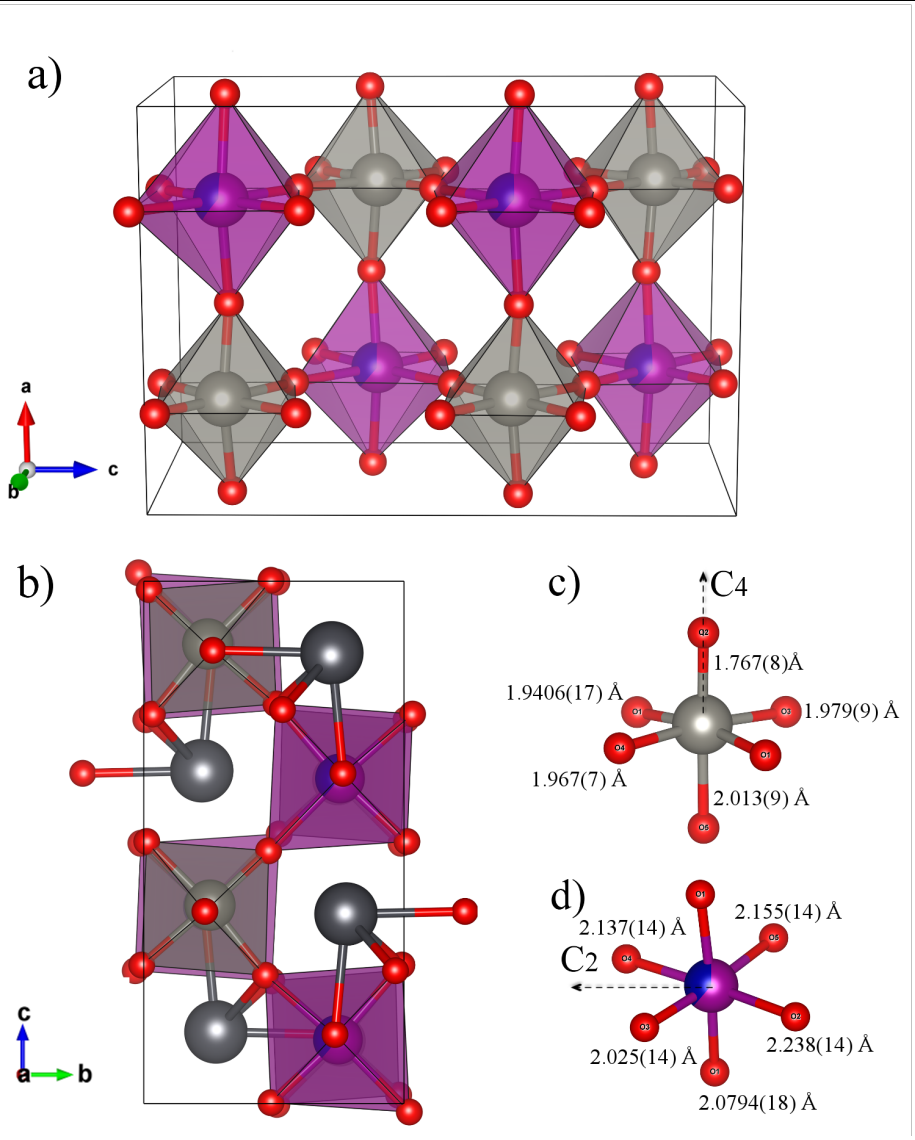

Figure 6-3 a) PMCW_50 crystal structure at room temperature: black and red spheres represent lead and oxygen atoms respectively, whereas tungsten and manganese/cobalt coordination octahedra are indicated in grey and violet. b) Projection of the structure on the ***bc*** plane, highlighting the four short Pb-O bonds. c, d) Graphical representation of the distorted octahedra of the tungsten (grey) and cobalt/manganese (blue/violet) atoms; the arrows indicate the direction of the local rotation pseudoaxis preserved in the distortion (see text).

The WO_6 polyhedra present a distortion typical of the d^0 cations, characteristic for example of Ti^{4+} in the tetragonal phase of $PbTiO_3$,[7] generally associated to a second order Jahn-Teller effect. The distortion, showing a pseudo C_4 type symmetry, consists in four almost equivalent basal bonds, ranging from 1.9406(17) to 1.979(9) Å, and in two apical bonds, one elongated (2.013(9) Å) and the other remarkably shortened (1.767(8) Å) as drawn in figure 6-3c. Nevertheless, the presence in the A site of the active lone pair influences the direction and the magnitude of the distortion, as shown in figure 6-3b. Particularly evident is the effect produced by the shift of the apical O1 oxygen on the deviation of the O1-W-O1 angle (169.3(3)°) from the ideal values (Figure 6-3a). The magnitude of the WO_6 distortion, calculated according to ref. 6, can be considered weak ($\Delta d = 0.25$ Å) and in particular results smaller than the one of PMW at the same temperature. This indicates that the isovalent substitution of Mn^{2+} with Co^{2+} determines the relaxation of WO_6 distortion.

The Mn/Co octahedron is less distorted ($\Delta d = 0.22$ Å) with respect to the tungsten one, but presents a pseudo C_2 type of distortion, moving from the centre of the octahedron towards a side, as indicated in figure 6-3d. The ADP's of the oxygen atoms are relatively high if compared with those of the other atoms; this is basically due to the static disorder accounted by considering the compositional disorder of the Mn/Co site. Indeed, the different ionic radius for the two cations (Mn^{2+} = 0.83 Å and Co^{2+} = 0.74 Å), leads to an expected local disordering of oxygen positions.

As pointed out by the structure analysis, all the coordination polyhedra are distorted and generate, locally, electrical dipoles. As shown in figure 6-4 the Pb dipoles are oriented along the [0 1 2] direction and are organized in rows parallel to the ***a*** axis and rotated of 90° respect to the neighbour one. In the same way, the sub-lattice of W dipoles is oriented along the same crystallographic direction and is organized with the same scheme. On the contrary, the Mn/Co dipoles are directed along the [0 1 0] direction and are arranged in stripes. Due to the presence of the inversion symmetry operation in the space group, the three

sub-lattices are perfectly balanced, suggesting a possible antiferroelectric character of the system, which however needs a deeper physical characterisation to be confirmed.

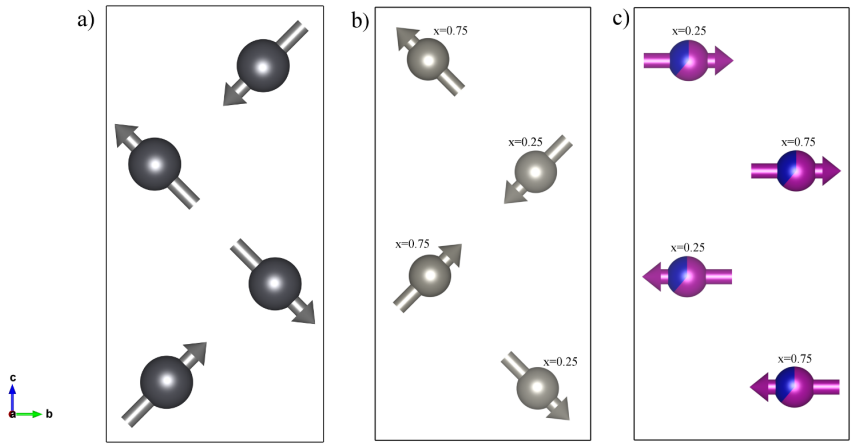

Figure 6-4 Schematic representation of the electrical dipole sub lattices of a) lead, b) tungsten and c) manganese\cobalt atoms. The arrows indicate the direction of the shifts from the centre of the respective coordination polyhedra.

6.2 Thermal evolution of the structure

The thermal evolution of the structure was studied by PXRD in the range RT - 400 K and by ToF-NPD on the WISH instrument in the low temperature range from RT to 2 K. The PXRD high temperature measurements show the occurrence of an orthorhombic-cubic transition around 345 K. Both phases coexist in a narrow temperature region (10 K), as can be noticed by the thermal evolution of the (0 2 4) and (4 0 0) reflections shown in figure 6-5. The high temperature cubic phase, like PMW, shows the *Fm-3m* space group symmetry and keeps the NaCl type B site cations arrangement of the RT phase, indicating the size and charge difference as the driving force of the ordering. The refinement of the cubic phase does not indicate the presence of anti-site defects,

but a high value of the ADP of the lead atom was found and interpreted as a strong indication of structural disorder. In fact, a statistical displacement from the coordination centre is required in a high symmetry system to preserve the lone pair character of the Pb atom.

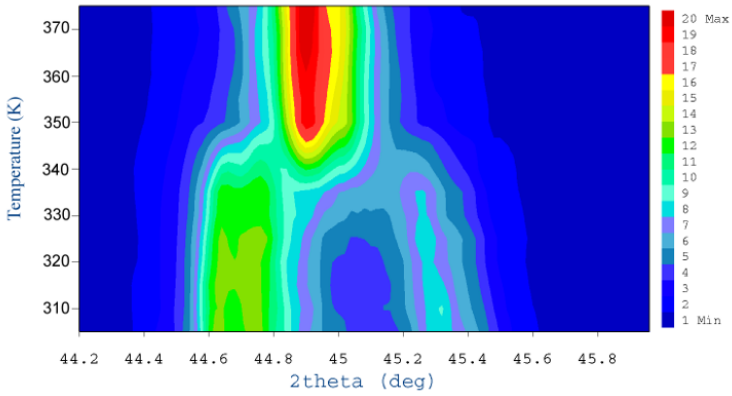

Figure 6-5 Thermal evolution of the (0 2 4) (2θ = 44.7°) and (4 0 0) (2θ = 45.3°) reflections of the orthorhombic structure, collapsing in a unique peak at 345 K, indicating a transition to cubic symmetry.

On the contrary, no structural transition was found by decreasing the temperature, where the initial behaviour of the lattice parameters is similar to PMW. Whereas the thermal behaviour of the ***a*** axis can be described by a typical phonon activate evolution, the ***b*** and ***c*** axes increase from RT to 200 K (figure 6-6), where the parameters stabilize and no further macroscopic change is observed down to 2 K. At very low temperatures, below 30 K, two additional phenomena are pointed out by NPD measurements in the behaviour of the cell volume. First, an inflection is observed around 20 K (T_{A1}), followed by a second change occurring nearby 10 K (T_{A2}), as shown in figure 6-6 top; at the same temperature a small anomaly occurrs in the ***c*** axis, evidenced in the inset of figure 6-6 bottom.

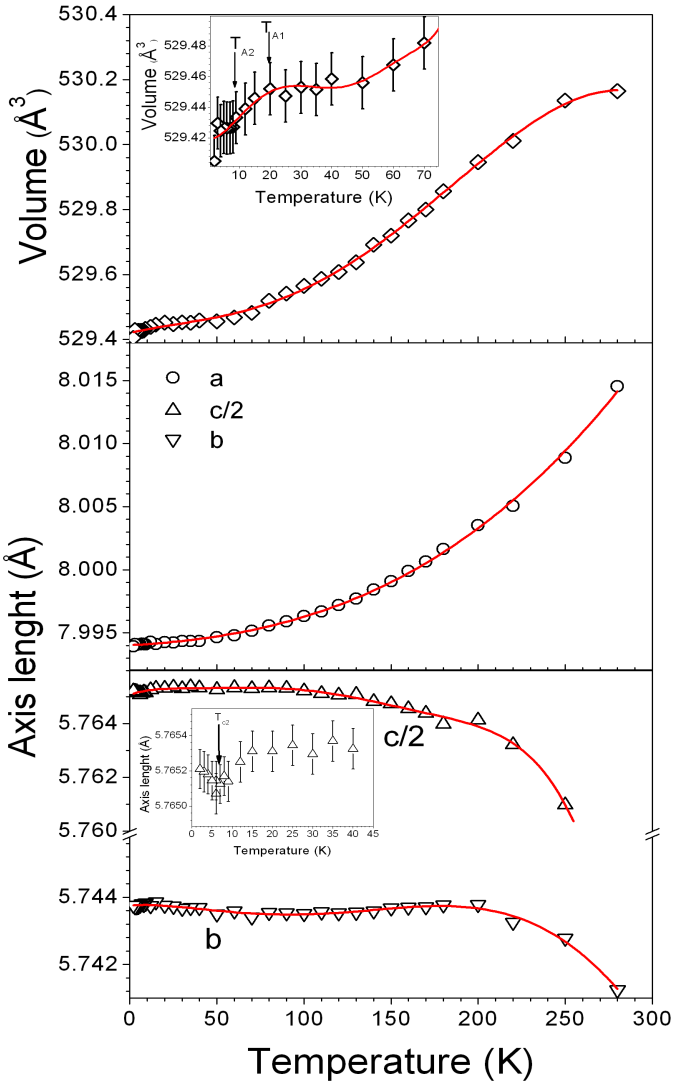

Figure 6-6 Thermal evolution of lattice parameters and cell volume of PMCW_50: top) thermal evolution of the cell volume: a zoom of the low temperature region showing two anomalies at T_{A1} and T_{A2} is shown in the inset. Middle) thermal evolution of the ***a*** axis; bottom) Thermal evolution of the ***b*** axis compared with ***c/2***: a zoom of the low temperature region, pointing out an anomaly for ***c/2***, is reported in the inset. In all cases, the error bars are smaller of the symbol size and the red line represents only a guide for the eyes.

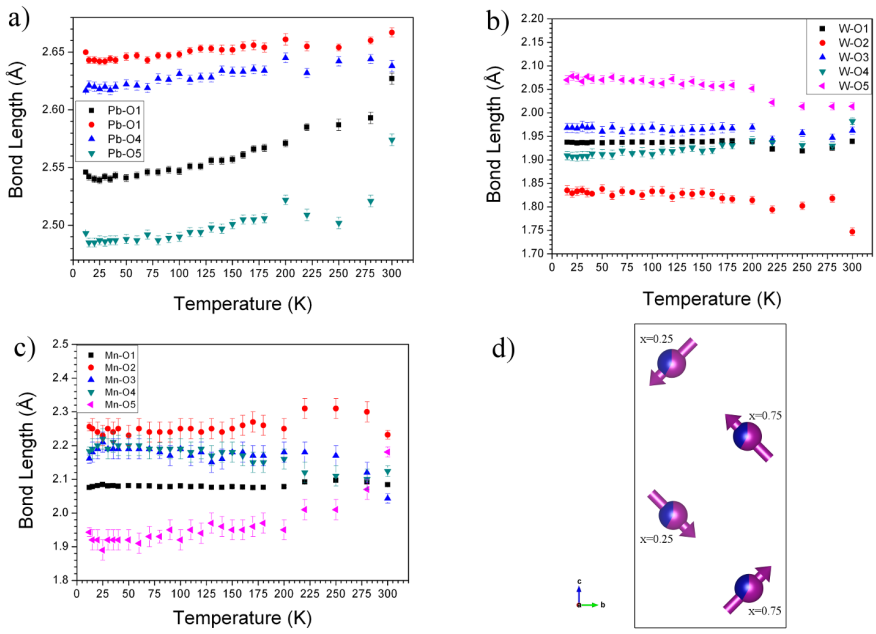

Figure 6-7 a,b,c) Thermal evolution of the metal-oxygen bond length in the structure; d) schematic representation of the Mn/Co electrical dipole sublattice below 200 K.

Figure 6-7 shows the thermal evolution of the bond lengths in the structure, as determined by the ToF-NPD data refinements. Differently from the case of lead and tungsten, whose coordination polyhedra do not shown significant changes with the temperature, the Mn/Co mixed site shows a modified distortion of the surrounding octahedron. On one side, the Mn-O5 bond distance decreases strongly in the temperature range RT - 200 K, becoming the shortest bond of the octahedron. On the other, with the exception of the Mn-O1 interaction that remains constant in all the temperature range, all the other bond lengths increase by decreasing the temperature in the same range; a comparable value is reached for the Mn-O3 and Mn-O4 bond, whereas Mn-O2 stabilizes as the longest bond. In this situation the local symmetry of the Mn/Co octahedron, that can be considered C_2 type at RT, becomes C_4 at 200 K, with a consequent rotation of the local Mn/Co dipole from the [010] to the [012] direction, as schematically drawn in figure 6-7d. Therefore, as indicated also by the

anomalous thermal behaviour of the ***b*** and ***c*** axes, the cubic to orthorhombic transition, occurring in the system at 345 K, is followed by an important structural re-arrangement that extends on a relevant range and is completed at 200 K. Accordingly no evident change in the crystal structure is observed below this temperature.

6.3 Magnetic characterization

The magnetic characterization of the sample was performed on a sintered pellet of mass 62.9 mg by means of a SQuiD magnetometer. ZFC and FC measurements, performed with different applied fields (H_a = 10, 500, 5000 Oe) are reported in figure 6-8. The measurements pointed out a first magnetic transition at T_{C1} = 188 K, strongly influenced by the applied field. By decreasing the temperature, a second magnetic transition, showing the characteristic cusp of an antiferromagnetic arrangement, was detected around T_{C2} = 9 K. Despite this, an irreversibility between ZFC and FC measurement observed for low applied field, indicates a weak ferromagnetic contribution. With the increase of the applied field the ZFC and FC curves tend to superimpose and the complete overlay is achieved for H_a > 5000 Oe. Simultaneously, the reduction of the susceptibility, particularly evident in the FC measurements, is observed in association with the disappearing of the first transition. This type of behaviour is observed in different double perovskites containing Mn^{2+} or Co^{2+} with diamagnetic atoms in the B' site,[1, 8-10] where these features are correlated with the presence of point and line defects or short range magnetic ordering. It is worthy to note that, with respect to PMW, the temperature of the first magnetic transition is increased to 190 K, suggesting that it could be strongly influence by the presence Mn-O-Co interactions in the APB's in mixed Mn-Co compounds.

The Curie-Weiss fit of the high temperature paramagnetic part of the inverse susceptibility indicates an antiferromagnetic character of the exchange interactions with $\Theta_{C\text{-}W}$ = -8.5(5) K and μ_{eff} = 5.5(2) μ_B.

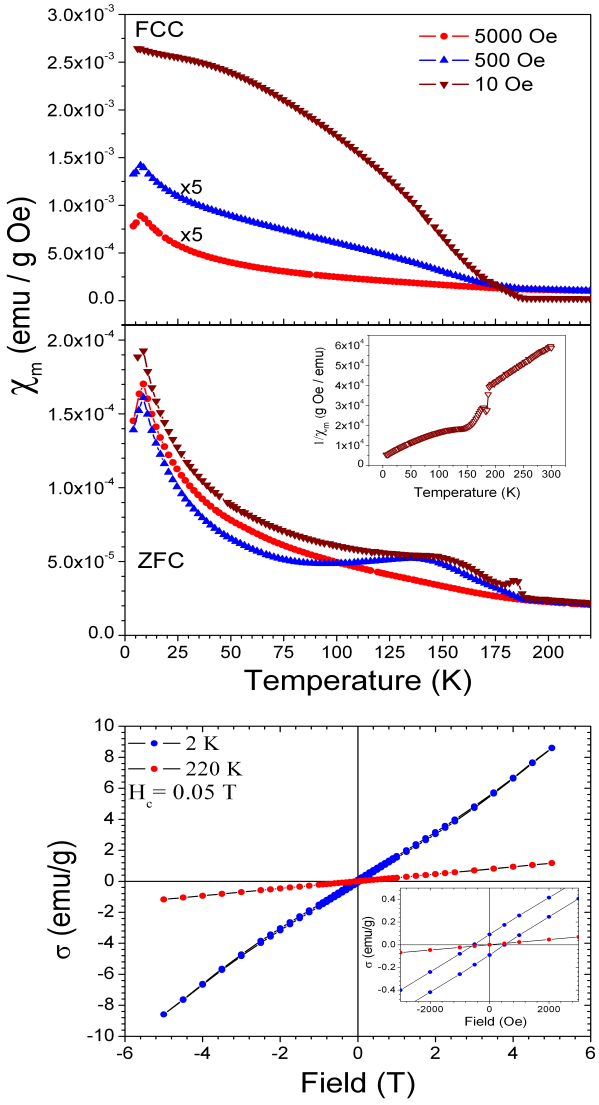

Figure 6-8 Field dependence of the FC and ZFC magnetization curves (top) measured at different applied field; the FC curves at 500 and 5000 Oe are scaled by a factor 5. Bottom) Hysteresis loops measured at 220 K and 2 K; as shown in the inset, a small coercive field H_C = 0.05 T is observed at 2 K.

The presence of Mn^{2+} (S = 5/2, μ_{eff} = 5.9 μ_B) and Co^{2+} (S = 3/2, μ_{eff} = 3.8 μ_B) in high spin configuration is not sufficient to provide explanation of the high value for μ_{eff}, therefore a contribution from the orbital momentum has to be

considered. Since the coordination octahedron is highly distorted, the crystal field removes completely the degeneracy of the *d*-orbitals and consequently the spin-orbit coupling is the sole possible source of orbital momentum. Several examples of Co^{2+} compounds, which exhibit μ_{eff} values exceeding 3.8 μ_B and indicating orbital contributions, are present in literature.[9-10] Moreover, by comparing Pb_2MnWO_6 and Pb_2CoWO_6, for which the μ_{eff} values are 5.7 and 4.5 μ_B respectively, a spin-orbit coupling contribution results evident for the cobalt compound. Consequently, it is plausible to consider the Co^{2+} ions as source of spin-orbit coupling even in PMCW_50.

It is interesting to note the peculiar evolution of the magnetization as a function of the temperature, recorded for the low field ZFC measurements in the region between 80 and 180 K (figure 6-8). In this range, by decreasing the temperature, the magnetization shows a broad peak that is suppressed by increasing the applied field. Figure 6-8 shows the hysteresis loops of the sample measured in the ±5 T field range at 220 K and 2 K. The small coercive field observed at 2 K (H_C = 0.05 T) is consistent with a weak ferromagnetism, as hypothesized on the basis of the M(T) measurement; furthermore the predominant linear character and the absence of saturation, at least in the field range examined, are indication of an AF nature of the sample.

6.4 Electrical characterization

Figure 6-9 shows the thermal behaviour of the DC resistivity. The sample shows high value of resistivity in all the temperature range and follows a thermally activated behaviour in the range from 200 to 350 K, with activation energy of 2.18(2) eV. For higher temperatures, the resistivity deviates from this trend and diverge at the orthorhombic to cubic transition. Below 200 K the curve presents three anomalies: two peaks, showing a maximum at 155 and 80 K, and a minimum at 12 K. The latter could be easily related with the AF magnetic transition highlighted in the M(T) measurement at 10 K, whereas the former

ones are not easy to understand at first sight. The resistivity measurements were also repeated with an applied magnetic field of a 2 T and such results are neglected since no appreciable variation connected to magnetoresistive effect was detected.

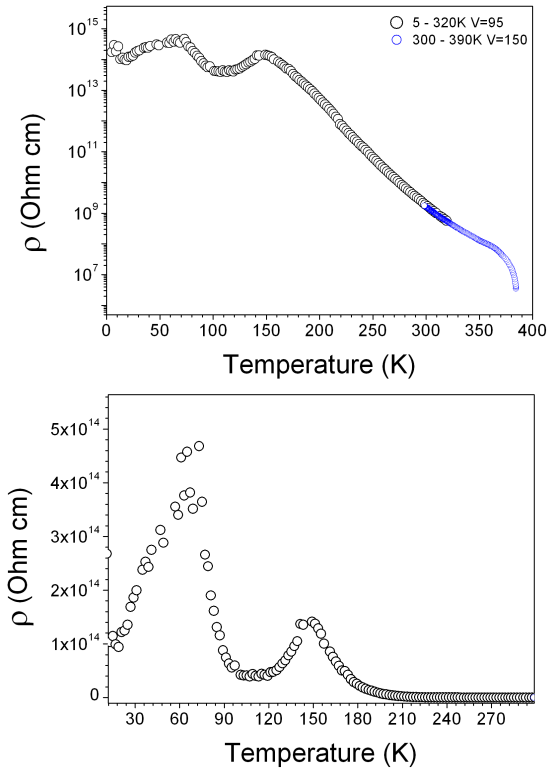

Figure 6-9 DC electrical resistivity of the PMCW_50 sample in the temperature range 2- 380 K. The resistivity peaks at 80 and 155 K are highlighted by the different scale choice on the bottom graph.

The dielectric constant was measured in the temperature range 2 – 300 K. The system shows high value of the dielectric constant in all the temperature range with negligible frequency dependence. The data point out a slope change at 190 K (for clarity see also the derivative in figure 6-10), the temperature of the first magnetic transition. A further change in the thermal behaviour (clearly

visible in the inset) occurs around 30 K. It is worth to note the existence of two minima in the $\partial\varepsilon/\partial T$ curve at 150 and 65 K, in correspondence of the two maxima in the resistivity curve shown in figure 6-9.

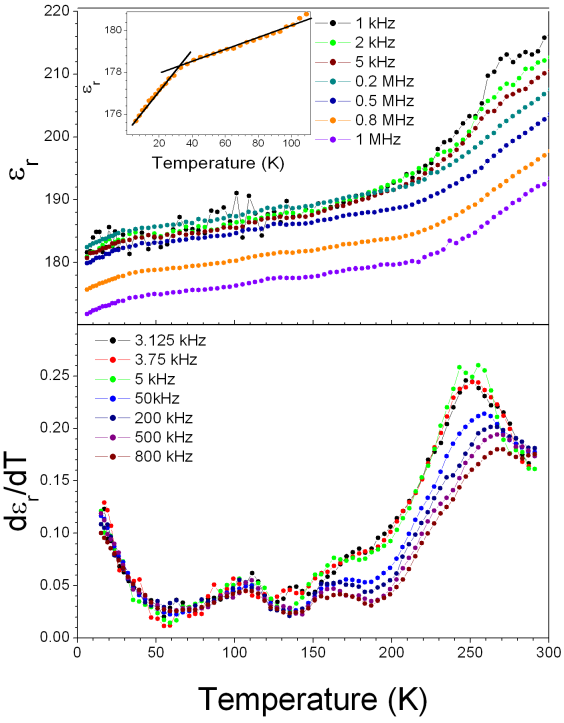

Figure 6-10. Dielectric constant measured in the temperature range 2-300 K at selected frequency; an enlargement of the low temperature region of the 0.8 MHz measurement is shown in the inset (top). Temperature derivative of the relative dielectric constant (bottom).

Pyroelectric measurements were performed on the same sample used for the resistive characterizations. The typical measurement of the PMCW_50 sample is shown in figure 6-11. The curve shows a complex behaviour of the DC polarization in the sample with the presence of three peaks. The most intense one at 340 K could be related to the cubic-orthorhombic transition observed at the same temperature in the PXRD measurements. The polarization change,

obtained by integrating the pyrocurrent and shown in figure 6-11, is indicative of the electrical nature of this transition, which could be identified as a para-antiferroelectric transition (PE-AFE) by the crystal symmetry analysis.

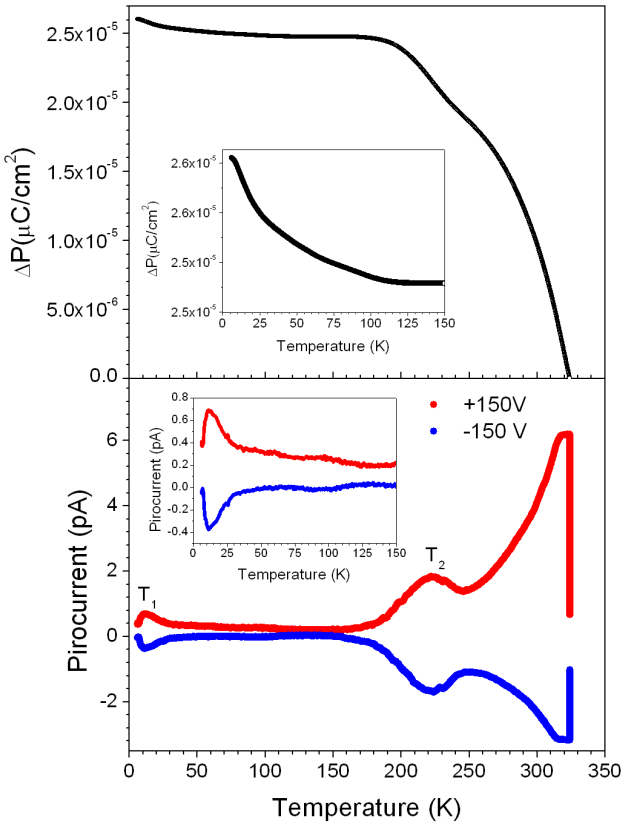

Figure 6-11 Pyrocurrent measurements of the PMCW_50 sample. Bottom) Typical pyrocurrent profile after poling at 380 K with voltage V = ±150 V. Top) Polarization variation obtained from the integration of the pyrocurrent measurements. In both cases a zoom of the low temperature region is shown in the inset.

Beside the PE-AFE transition at 345 K, the measurement presents other features. At low temperature two peaks, denoted as T_1 and T_2 and occurring around 15 and 200 K, are present. The first one could be related to the antiferromagnetic transition observed in the magnetization measurement at 10 K

and the second with the first magnetic transition at 188 K. The assignment of T_1 and T_2 are supported by the change in the polarization of the system around the magnetic transition temperatures (T_{C1} = 188 K and T_{C2} = 9 K) shown in figure 6-11 (top). These effects, joined with the anomalies T_{A1} and T_{A2} detected in the behaviour of the cell volume (see figure 6-6) and to the magnetic measurements, represents a clear indication of a spin-lattice coupling in the system. Furthermore the inversion of the peaks present in the pyrocurrent measurements with the change of the poling filed sign indicate the possible ferroelectric character of these contributions.

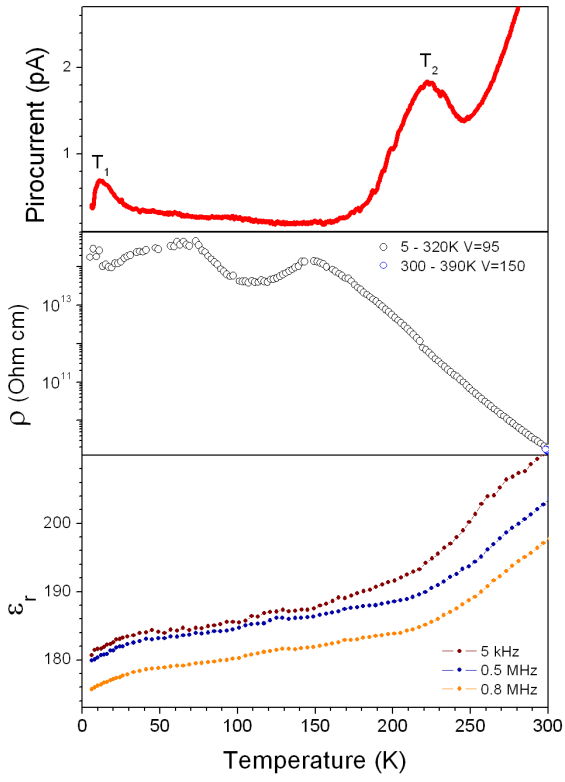

Figure 6-12 Comparison between the different electrical characterization measurements: (top) pyrocurrent measurement, (central) resistance and (bottom) dielectric constant.

Figure 6-12 shows the comparison among the various electrical measurements to better appreciate the corresponding relationships. First, the T_1 peak in the pyrocurrent measurement is related to a minimum in the resistivity connected to a change in the slope of the thermal behaviour of the dielectric constant, to the 9 K AF magnetic transition and to the T_{A1} anomaly in the cell volume as well. Then an abrupt change of the dielectric constant trend at T_2 is associated to a further magnetic transition, evidencing a possible magneto-dielectric coupling in the system.

6.5 Magnetic structure analysis

A series of ToF-NPD experiments were performed on the WISH instrument in the temperature range 1.5 – 300 K. As indicated in figure 6-13a, some extra reflections, having the characteristic temperature dependence of magnetic reflections, appear below 10 K, differently from what happens at the first magnetic transition (T_{c1} = 188 K), below which only an increase of diffuse scattering in the d-range 7 - 12 Å (see figure 6-13b) is observed. The diffuse scattering becomes particularly evident below 80 K, joined to a strong temperature dependence of the paramagnetic background, as indication of changes in the magnetic interaction.

To better analyse the evolution below T_{C1}, the background on the long-d bank ($2\theta = 27.0°$) was integrated in the d-range 14 – 18 Å and plotted in figure 6-13c. The integrated value decreases monotonically from 190 K down to low temperature (the anomaly around 90 K is probably due to the switch of the exchange gas in the cryostat) as indication of a progressive increase of the magnetic interactions. Two main changes are observed in the temperature behaviour. The first one occurs around 190 K and is related to the first magnetic transition T_{C1}. The second one, consisting in a drastic change of the slope, is related to the appearing of the magnetic peaks.

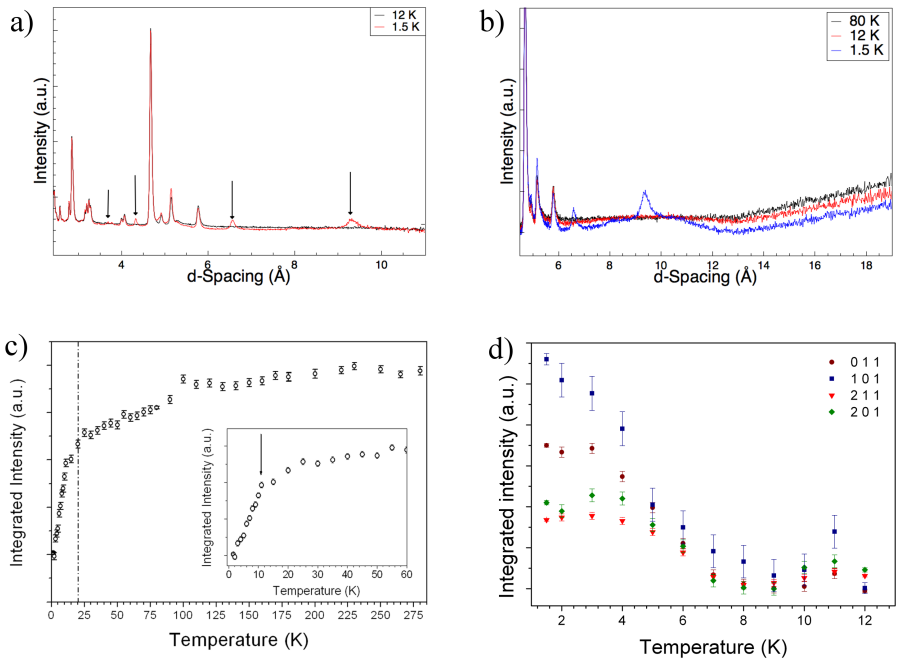

Figure 6-13 a) Superposition of the 1.5 K and 12 K ToF diffraction data, the arrows indicate the magnetic reflections. b) Evolution of the diffuse scattering at long d-spacing. c) Integration of the paramagnetic background in the d-range 14 -18 Å as function of the temperature. d) Intensity of selected magnetic reflections as function of the temperature; the indices refer to the magnetic unit cell.

By the analysis of the diffraction pattern collected at 1.5 K, and in particular by the pure magnetic diffraction pattern obtained from the subtraction between the 12 and the 1.5 K data, it is evident that a propagation vector $\kappa_1 = (0\ 0\ 0)$, referred to the presence of magnetic intensity on the nuclear reflections, is not sufficient to index the whole magnetic pattern. By the use of the k-search software[11] of the Fullprof suite, it was possible to index the remaining peaks with a propagation vector $\kappa_2 = (½\ 0\ 0)$. The magnetic symmetry was analysed by means of the ISODISTORT[12] software combining the two propagation vectors κ_1 and κ_2; the output of the analysis is reported in table A-3 in appendix. A carefully analysis of the magnetic systematic absences was performed with the

help of the MAGNEXT[13] software of the Bilbao crystallographic server,[14-16] in order to reduce the possible space groups

The Rietveld refinement was performed in all the possible magnetic space groups having the appropriate systematic extinctions by means of the Jana2006 software.[2] The best agreement between observed data and the calculated model was obtained for the *Pm'c2₁'* space groups; the corresponding Rietveld plots are reported in figure 6-14, the results of the refinement are summarized in table 6-3 and the atomic coordinates of the magnetic cell are reported in table A-4 in the appendix. Beside the symmetry constrains imposed by the magnetic space group, further constrains were added in the last steps of the refinement, as suggested by the behaviour of some parameters achieving convergence. In particular the M_z moduli of the three independent Mn/Co sites, approaching similar values during refinement, were constrained to assume the same value. Similarly, M_x (for the Mn1 site) and M_y, assuming negligible values within the e.s.d.'s, were fixed to zero.

Table 6-3 Crystal data and refinement reliability factor at 1.5 K

Chemical Formula	$Pb_2Mn_{0.6}Co_{0.4}WO_6$
Space Group	*Pm'c2₁'*
a(Å)	15.9836(5)
b(Å)	5.7421(2)
c(Å)	11.5272(4)
Volume(Å^3)	1057.98(6)
κ_1	(0 0 0)
κ_2	(1/2 0 0)

	WISH 2θ=152.82°	**WISH 2θ=121.66°**	**WISH 2θ=90°**	**WISH 2θ= 58.33°**	**WISH 2θ=27.08°**	**Overall**
Gof	6.71	6.22	5.82	3.93	1.31	5.46
$R(F)_{obs}$	3.21	3.72	3.92	3.90	1.38	-
Rp	3.60	3.60	3.73	2.92	0.88	3.22
wRp	4.59	4.59	4.44	3.30	1.11	4.15

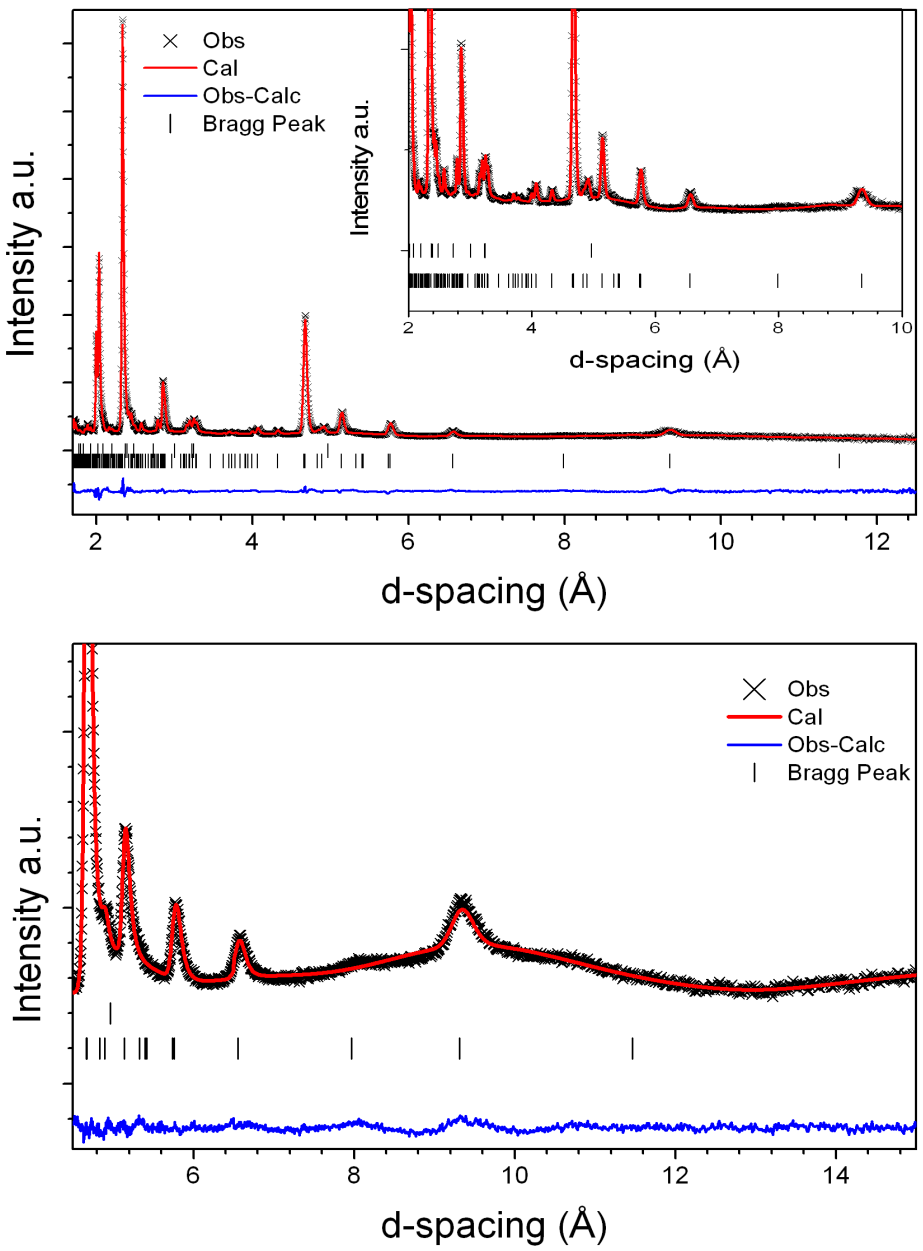

Figure 6-14 Rietveld plot of WISH bank with 2θ= 58.3° and 27.0° of the *Pm'c2₁'* model; the zoom of the high d-space region of the 2θ= 58.3° bank is shown in the inset. Observed (×, black), calculated (line, red), and difference (line, blue) patterns are reported; the tick marks show the calculated position of the reflections.

Table 6-4 Refined magnetic parameters.

Atom site	M_x (μ_B)	M_y (μ_B)	M_z (μ_B)
Mn/Co1	0	0	1.47(3)
Mn/Co2	0	0	-1.47(3)
Mn/Co3	0	0	1.47(3)

The refined values of the magnetic parameters are reported in table 6-4. The small value of the refined magnetic moment with respect to the expected one (5.11 μ_B in case of Mn^{2+} *hs* and Co^{2+} *hs* with unquenched orbital momentum) is probably due to the chemical disorder of the magnetic site. Moreover, from figure 6-13b, the presence of diffuse scattering is evident even at 1.5 K, indicating the partial occurrence of short-range interactions possibly generated by the frustration of the magnetic ordering in the system.

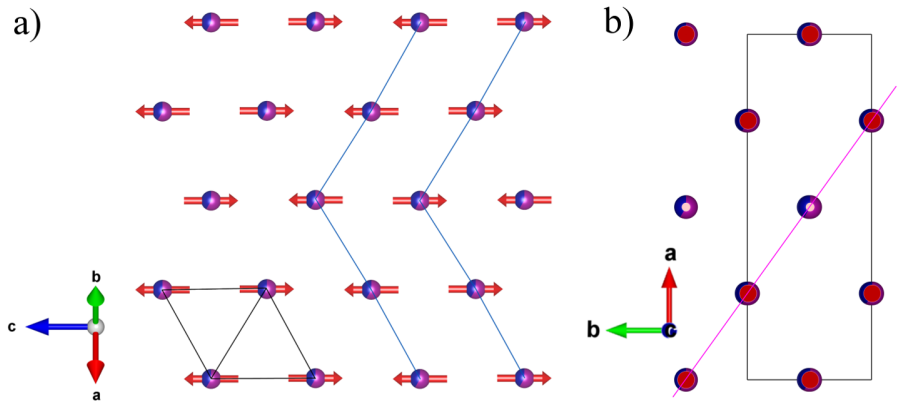

Figure 6-15 Schematic representation of the magnetic structure of PMCW_50; only the magnetic atoms are represented for clarity, a) the "fundamental unit" (black lines) and alternate zig-zag stripes (blue line) of ferromagnetic interactions stacked in an AF way on the {111} plane of the fundamental perovskite; b) orientation of the considered magnetic planes with respect to the magnetic cell.

The refined magnetic model, consisting in a collinear antiferromagnetic structure with the spin lying along the ***c*** direction, is reported in figure 6-15. The "fundamental unit" of the structure, shown in figure 6-15a, consists in four next

neighbour magnetic atoms arranged in triangular lattices with three almost equivalent distances ranging from 5.605(1) - 5.769(1) Å. If we consider the interactions generated by all the possible exchange paths, these are probably of the same intensity and, as suggested by the negative $\Theta_{C\text{-}W}$, of AF nature. In this scenario, the system shows the characteristics of a classical geometrical frustration, with only two of the three possible interactions having an AF nature. This would lead to six degenerate configurations, but the observed symmetry reduction from *Pmcm* to *Pmc2₁* removes the degeneracy via a spin driven Jahn-Teller effect, bringing to a small lattice distortions. The "fundamental units" lie on the {111} plane of fundamental perovskite cell and their disposition gives rise to a zig-zag arrangement of ferromagnetic interactions that are coupled in a AF way along the ***c*** direction of the magnetic cell.

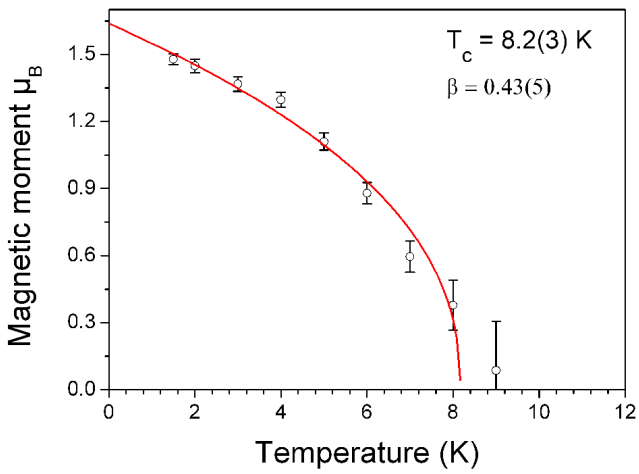

Figure 6-16 Refined value of the magnetic moment as a function of the temperature; the red line represents the best fit with equation 1 (see text).

The proposed model was used to follow the thermal evolution of the magnetic structure. The refined value of the magnetic moment as a function of

the temperature is reported in figure 6-16. The experimental values of the magnetization were fitted with a classical power law:

$$M(T) = M_0\left(1-\frac{T}{T_c}\right)^{\beta} \qquad (1$$

The obtained value of the T_c is in good agreement with the antiferromagnetic transition observed at T_{C1} in the magnetization measurements (figure 6-8). Nevertheless the irreversibility between ZFC and FC measurements and the M(H) loop clearly indicates that a weak ferromagnetic contribution is present in the systems. In the light of the magnetic structure this weak ferromagnetism may have two origins. On one side it could be produced by the short range interactions that survive at very low temperature, as indicated by the diffuse magnetic scattering present even in the 1.5 K diffraction pattern. Alternatively it could derive from a canting of the antiferromagnetic structure, since the magnetic space group $Pm'c2_1'$ allows a ferromagnetic contribution along the ***b*** axis.

6.6 Spin-lattice coupling

The symmetry reduction at the establishing of the long-range magnetic order can be considered the evidence of a Spin Driven Jahn-Teller (SDJT) mechanism first shown by Yamashita and Ueda[17] in pyrochlore systems, where the ground state degeneracy is removed by a lattice distortion driven by magneto-elastic striction.

Other example of SDJT effect are reported in literature on both collinear and non-collinear magnetic systems.[17-27] We focus here on collinear magnetic structures and on the possibly induced electrical polarization, whereas the effects of non collinear structure are discussed in chapter 2. One of the first examples is the orthorhombic rare earth manganite $RMnO_3$(R= Ho, Y). This system shows incommensurate magnetic ordering below $T_{N1} \approx 42$ K, and at $T_{N2} \approx 26$ K the

propagation vector locks into a commensurate value to generate an E-type antiferromagnetic structure.[18] Pyrocurrent measurements reveal, in conjunction with T_{N2}, the appearance of electrical polarization. Since the s.g. of the nuclear structure is centric, *Pbnm*, and does not allows spontaneous polarization, the inversion centre breaking at the magnetic transition via SDJT is invoked. Sergienko at al.[19], using the Landau theory, show that the E-type AF ordering could break the spatial inversion centre and give rise to a net polarization. In this frame, the electric polarization is generated in a microscopic model by the interplay between electron hopping and elastic energy, in presence of octahedral tilting. The elastic energy (magnetostrictive effect) tends to reduce the Mn-O-Mn angles and changes the oxygen barycentre, inducing the polarization. Lorentz et al.[18] found that the polarization is strongly influenced by the Ho sublattice; in particular a considerable increase of the polarization is observed when the rare earth orders magnetically, indicating that probably the spin orbit coupling of the Ho atoms plays an essential role. In any case the polarization experimentally observed in a polycrystalline sample is 0.008 $\mu C/cm^2$,[18] and increases at 0.15$\mu C/cm^2$ in a single crystal,[20] remaining however well below the outstanding calculated values ranging between 0.5 and 12 $\mu C/cm^2$.[19]

Other examples are represented by the compounds of the series RMn_2O_5 with R= rare earth. These charge-ordered compounds order magnetically below 50 K with an incommensurate (IC) propagation vector that depends on the ionic radii of the rare earth.[21] By decreasing the temperature the propagation vector locks to a commensurate value and the magnetic structure results an almost collinear AF structure. A further decrease of the temperature promotes a new transition to a different IC phase and finally, at very low temperature, some members of the series additionally display the ordering of the rare earth.[21] It was pointed out that the system shows large variations of the dielectric proprieties in conjunction with all these magnetic transitions, in particular in the commensurate phase.[21] Moreover clear evidences of magneto-electric coupling, indicating strong spin-lattice interaction, were observed, like reversal of the

electrical polarization by the application of a magnetic field[23] and colossal magneto-dielectric effect.[24] Also in this case the nuclear space group before the transition is the centrosymmetric *Pbam* and consequently the magnetic transition breaks the space inversion symmetry to the supposed $P_{2a}b'2_1m'$ (OG setting, BNS P_aca2_1).[25] In literature, some authors couple this symmetry break to SDJT and magnetostrictive effect.[25-27] In particular Chapon at al.[26, 27] shows that the observed polarization is the result of symmetric exchange striction. This mechanism is, in a certain way, a generalization in 3D of the spin-Peiers dimerization in 1D.[28] If we take a one dimensional chain of two cations with different valence, the spin Hamiltonian could be written as:

$$H = \sum_{i=1}^{n} J_{i,i+1}(S_i \cdot S_{i+1}) \qquad (2$$

If the exchange interaction $J_{i,i+1}$ is modulated by the atoms displacement u_i

$$J_{i,i+1} = J_0 + \partial J(u_i - u_{i+1}) \qquad (3$$

the dimerization is spontaneous and lead to energy gain (figure 6-17).

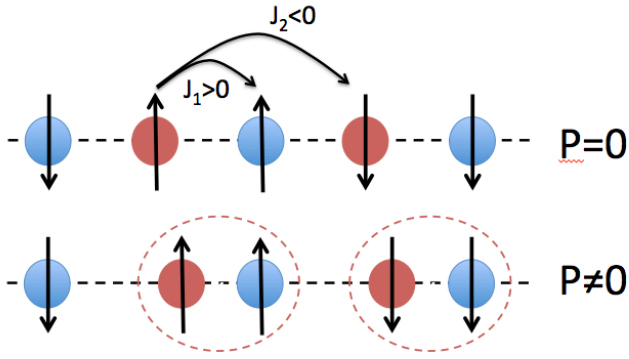

Figure 6-17 Schematic representation of the symmetric exchange striction mechanisms in a 1D chain with FM nearest neighbour interaction and AF next nearest neighbour interaction. The different colour indicates two chemical species with different charge.

Now if the two magnetic atoms are isovalent, there is no electric polarization resulting from the dimerization; however, when the two ions in the chain have a different valence, a spontaneous polarization is developed from the spin-Peiers mechanism. The polarization could be expressed, also in absence of a complete dimerization, as:

$$P = \sum_{i}^{n} C_{i,i+1}^{ex} (\vec{S}_i \cdot \vec{S}_{i+1}) \quad (4$$

where C^{ex} is the constant describing the strength of the symmetric exchange striction. This entire scenario could be explained in a less formal, but simpler, way. Let's imagine to have an Ising 1D spin chain with FM nearest neighbour (NN) and AF next nearest neighbour interactions (NNN); the frustrated system has as ground state in the ↑↑↓↓ configuration if $J_2 > |J_1|/2$. This spin arrangement breaks the spatial inversion centre and in presence of different ion charges or tilted polyhedra configuration generates an electrical polarization (figure 6-17), by shortening the bonds with the satisfied exchange interaction and by stretching the unsatisfied ones.[29] In 3D these mechanism could be easy generalized by taking into account all the spin couples i, j:

$$P = \sum_{i,j}^{n} C_{i,j}^{ex} (\vec{S}_i \cdot \vec{S}_j) \quad (5$$

In case of PMCW_50 the calculated polarization obtained by the application of equation 5 to the experimental values of the spins obtained from the long range magnetic structure is shown in figure 6-18, compared with the integration of the pyrocurrent from 150 K to 5 K. Clearly, the used model accounts in some extent the experimental polarization below the long range order transition, but is not describing all the characteristic of the observed polarization since it do not take into account the presence of small short-range ordered domains above and even below the transition.

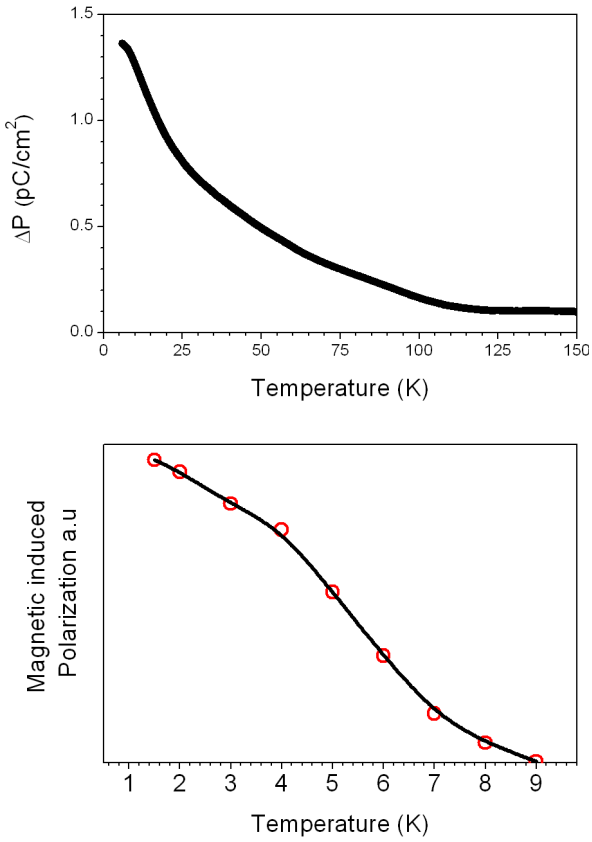

Figure 6-18 Top) Experimental polarization obtained from the integration of the pyrocurrent (before the integration, a constant current value was subtracted as background correction due to the instrument set up). Bottom) Magnetic induced polarization in the PMCW_50 sample due to the long-range magnetic structure via symmetric exchange striction mechanism.

To model the observed polarization, it is necessary to take into account the symmetric exchange striction contribution arising from these small domains. For this purpose, we integrated the paramagnetic background in the d-spacing range 14-18 Å (figure 6-13c), whose strong temperature dependence, that becomes appreciable thanks to the very low instrumental background of the WISH instrument, is an indication of the loss of pure paramagnetic region.

Halpern and Johnson[30] shown that the differential cross section of neutron due to a paramagnetic substance is:

$$d\Phi_m = \frac{2}{3}S(S+1)\left(\frac{e^2\gamma F^{\frac{1}{2}}}{mc^2}\right)^2 d\Omega. \qquad (6$$

where S is the spin quantum number, F is the amplitude of the form factor, γ is the neutron magnetic moment in μ_B, m is the mass of the neutron, e is the electric charge and c is the speed of light.

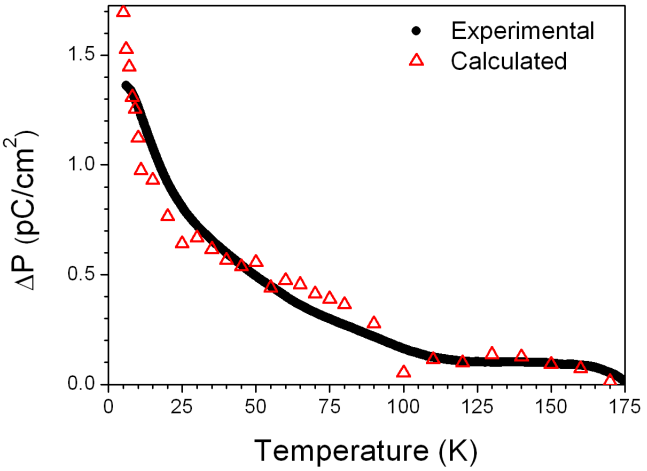

Figure 6-19 Experimental (black line) and calculated (red triangles) polarization as function of temperature.

If we assume that the major contribution to the variation of the background with the temperature is mainly due to the change in the magnetic behaviour of the system, then the reduction of the paramagnetic background is proportional to the increase of the fraction of interacting cations and in particular to *S(S+1)*. By taking this value from the experimental integration of the background and by applying equation 5 one can follow the temperature evolution of the electrical polarization. The results are shown in figure 6-19,

where the calculated polarization has been scaled by a constant to take into account the unknown magnetoelestic coupling constant. A good agreement, at least from a qualitative point of view, is clearly visible in spite of the quite simplified model that does not take into account other possible source of electrical polarization. This suggests an important role of the symmetric exchange striction mechanism, confirming that the magnetic and electric ordering in the system are related by a solid spin-lattice interaction and that the frustration of the magnetic interaction is resolved via a SDJT effect.

6.7 Conclusions

Figure 6-20 reports a graphical representation of the PMCW_50 1D phase diagram constructed on the basis of the undertaken structural and physical characterization. At high temperature, in particular above 345 K, the system is paraelectric (PE) and paramagnetic (PM) with cubic symmetry. By decreasing the temperature a first transition is observed at 345 K from the cubic high temperature phase to the orthorhombic RT phase that is centrosymmetric with s.g. *Pmcn*. The physical characterization shows at this temperature the occurrence of different events, such as an intense pyrocurrent peak and a strong resistivity increase coupled with a progressive expansion of the ***bc*** plane with decreasing the temperature below the transition, indicating a stabilization of the distortion on cooling. These are all indications of an electrical transition that, because the centrosymmetric nature of the RT structure space group, should lead to an antiferroelectric (AFE) polar state. It's worthy to underline that, on the basis of powder diffraction data, it is rather difficult to discriminate between centro or non-centro symmetry specially if a remarkable lattice distortion is absent. To clarify this point further physical characterizations, like electric hysteresis loops or single crystal diffraction experiments, are necessary.

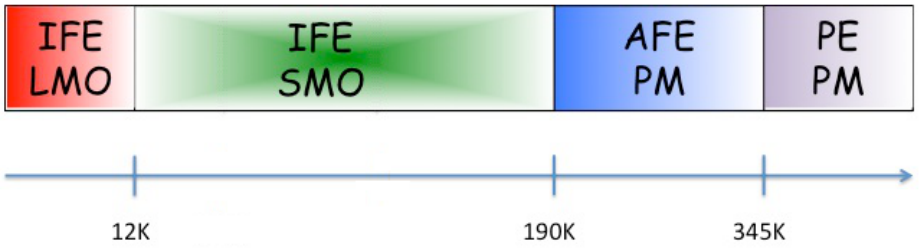

Figure 6-20 Phase diagram of PMCW_50. At low temperatures the system presents a long-range magnetically ordered phase (LMO) inducing a ferroelectric state (IFE) via a SDJT effect. By increasing the temperature the system undergoes a magnetic transition to a short-range order phase (SMO). At 190 K the system became magnetically disordered and the previously induced ferroelectric state is destroyed in favour of an antiferroelectric (AFE) and paramagnetic (PM) state. Finally at 345 K the system undergoes an orthorhombic to cubic transition in which both the ferroic state are destroyed.

By decreasing the temperature the systems undergoes a first magnetic transition at T_{C1} = 188 K, observed in the M(T) measurements. The progressive increasing of the applied magnetic field weakens this transition up to the complete suppression. No new reflections appear in the ToF-NPD pattern below this temperature, but the observed paramagnetic background is an indication of short-range interactions. The transition is connected to a series of phenomena that can be considered indications of changes in the electrical order of the system: a broad peak in the pyrocurrent measurement (indication of changes in the electrical polarization), a change of the transport properties and finally the change of the temperature dependence of the dielectric constant. Therefore the transition observed at T_{C1} could be described in terms of a conversion between the AFE/PM phase to a Short-range Magnetically Ordered (SMO) state inducing locally an improper ferroelectric state (IFE). In the stability range of this SMO/IFE phase, the magnetic interaction and consequently the polarization of the system manifest minor variations until 20 K, where the paramagnetic background, linearly related to the magnetic interactions of the system, changes

its temperature trend disclosing the final low temperature transition. At 9K all the electric properties (pyrocurrent, resistivity and dielectric constant) show noticeable variations in connection with the appearing of long range collinear antiferromagnetic ordering (LMO) in the non-centrosymmetric magnetic space group $Pm'c2_1'$. This transition is a classic example of a Spin Driven Jahn-Teller effect,[17, 26] in which a small lattice distortion is induced to resolve the ground state degeneracy of a magnetically frustrated system. The observed polarization is produced by the breaking of the spatial inversion symmetry caused by symmetric exchange striction mechanism, as supported by the modelling of the experimental polarization, obtained from the pyrocurrent measurement, by means of equation 5 and from the thermal evolution of the paramagnetic background.

All the experimental evidences point towards the presence of a strong spin-lattice coupling deriving from the spin-orbit interaction of the Co^{2+} atoms, as suggested by the analysis of the paramagnetic part of the M(T) measurements. The structural and physical characterization of the sample indicates the $Pb_2Mn_{0.6}Co_{0.4}WO_6$ as a type II multiferroic material, surely below 10K but also probably below 190 K.

6.8 Reference

[1] Orlandi F.; Righi L.; Cabassi R.; Delmonte D.; Pernechele C.; Bolzoni F.; Mezzadri F.; Solzi M.; Merlini M. and Calestani G. "*Structural and Electric Evidence of Ferrielectric State in Pb_2MnWO_6 Double Perovskite System*" Inorg. Chem. (2014) 53, 10283−10290.

[2] Petricek, V.; Dusek, M.; Palatinus, L. "*Crystallographic Computing System JANA2006: General features"* Z. Kristallogr. (2014), 229, 345– 352.

[3] Baldinozzi G., Sciau Ph., Pinot M. and Grebille D. "*Crystal structure of the antiferroelectric perovskite Pb_2MgWO_6*" Acta Cryst. (1995) B51, 668-673.

[4] Nespolo, M.; Ferraris, G., Ohashi, H. "*Charge distribution as a tool to investigate structural details: meaning and application to pyroxenes*" Acta Crystallogr. (1999), B55, 902−916.

[5] Walsh A., Payne D. J., Egdellb R. G. and Watsonc G. W. "*Stereochemistry of post-transition metal oxides: revision of the classical lone pair model*" Chem. Soc. Rev. (2011), 40, 4455−4463.

[6] Halasyamani P. S. *"Asymmetric Cation Coordination in Oxide Materials: Influence of Lone-Pair Cations on the Intra-octahedral Distortion in d^0 Transition Metals"* Chem. Mater. (2004), 16, 3586−3592.

[7] Shirane G., Pepinsky R. and Frazer B. C. *"X-ray and neutron diffraction study of ferroelectric $PbTiO_3$*" Acta Crystallogr. (1956), 9, 131-140.

[8] Mandal T. K., Abakumov A. M., Lobanov M. V., Croft M. , Poltavets V. V. and Greenblatt M. *"Synthesis, Structure, and Magnetic Properties of $SrLaMnSbO_6$: A New B-Site Ordered Double Perovskite"* Chem. Mater. (2008), 20, 4653-4660.

[9] Blanco M. C., De Paoli J. M., Ceppi S., Tirao G., Nassif V. M., Guimpel J. and Carbonio R. E *"Synthesis, structural characterization and magnetic properties of the monoclinic ordered double perovskites $BaLaMSbO_6$, with M = Mn, Co and Ni"* J. of Alloys and Compounds (2014), 606, 139-148.

[10] Viola M. C., Martınez-Lope M. J., Alonso J. A., Martınez J. L., De Paoli J. M., Pagola S., Pedregosa J. C., Fernandez-Dıaz M. T. and Carbonio R. E. *"Structure and Magnetic Properties of Sr_2CoWO_6: An Ordered Double Perovskite Containing $Co^{2+(}$HS) with Unquenched Orbital Magnetic Moment"* Chem. Mater. (2003), 15, 1655-1663.

[11] Rodríguez-Carvajal J. *"Recent Advances in Magnetic Structure Determination by Neutron Powder Diffraction"* Physica B, (1993), 192, 55-69

[12] Campbell B. J., Stokes H. T., Tanner D. E. and Hatch D. M., *"ISODISPLACE: An Internet Tool for Exploring Structural Distortions."* J. Appl. Cryst., (2006) 39, 607-614.

[13] Gallego S. V., Tasci E. S., de la Flor G., Perez-Mato J. M. and M. I. Aroyo *"Magnetic symmetry in the Bilbao Crystallographic Server: a computer program to provide systematic absences of magnetic neutron diffraction"* J. Appl. Cryst. (2012), 45(6), 1236-1247.

[14] Aroyo M. I., Perez-Mato J. M., Orobengoa D., Tasci E., de la Flor G. and Kirov A. *"Crystallography online: Bilbao Crystallographic Server"* Bulg. Chem. Commun. (2011), 43(2), 183-197.

[15] Aroyo M. I., Perez-Mato J. M., Capillas C., Kroumova E., Ivantchev E., Madariaga G., Kirov A. and Wondratschek H. *"Bilbao Crystallographic Server I: Databases and crystallographic computing programs"* Z. Krist. (2006), 221, 1, 15-27.

[16] Aroyo M. I., Kirov A., Capillas C., Perez-Mato J. M and H. Wondratschek *"Bilbao Crystallographic Server II: Representations of crystallographic point groups and space groups"* Acta Cryst. (2006), A62, 115-128.

[17] Yamashita Y. and Ueda K. *"Spin-Driven Jahn-Teller distortion in a pyrochlore system"* Phys. Rev. Lett. (2000) 85,4960-4963.

[18] Lorenz B., Wang Y. and Chu C. W. *"Ferroelectricity in perovskite $HoMnO_3$ and $YMnO_3$"* Phys. Rev. B (2007) 76, 104405.

[19] Sergienko I. A., Sen C. and Dagotto E. *"Ferroelectricity in the Magnetic E-Phase of Orthorhombic Perovskites"* Phys. Rev. Lett. (2006) 97, 227204.

[20] Lee N., Choi Y. J., Ramazanoglu M., Ratcliff II W., Kiryukhin V. and Cheong S.-W. *"Mechanism of exchange striction of ferroelectricity in multiferroic orthorhombic $HoMnO_3$ single crystals"* Phys. Rev. B (2011), 84, 020101(R).

[21] Radaelli P.G. and Chapon L.C. *"A neutron diffraction study of RMn_2O_5 multiferroics"* J. Phys.: Condens. Matter (2008), 20, 434213.

[22] Noda Y., Kimura H., Fukunaga M., Kobayashi S., Kagomiya I. and Kohn K. *"Magnetic and ferroelectric properties of multiferroic RMn_2O_5"* J. Phys.: Condens. Matter (2008), 20, 434206.

[23] Hur N., Park S., Sharma P. A., Ahn J. S., Guha S. and Cheong S-W. *"Electric polarization reversal and memory in a multiferroic material induced by magnetic fields"* Nature (2004), 429, 392.

[24] Hur N., Park S., Sharma P. A., Guha S., and Cheong S-W. *"Colossal Magnetodielectric Effects in $DyMn_2O_5$"* Phys. Rev. Lett. (2004) 93, 107207.

[25] Blake G. R., Chapon L. C., Radaelli P. G., Park S., Hur N., Cheong S-W., and Rodríguez-Carvajal J. *"Spin structure and magnetic frustration in multiferroic RMn_2O_5 (R=Tb,Ho,Dy)"* Phys. Rev. B (2005), 71, 214402.

[26] Chapon L. C., Blake G. R., Gutmann M. J., Park S., Hur N., Radaelli P. G., and Cheong S-W. *"Structural Anomalies and Multiferroic Behavior in Magnetically Frustrated $TbMn_2O_5$"* Phys. Rev. Lett. (2004), 93, 177402.

[27] Chapon L. C., Radaelli, P. G., Blake G. R, Park S., and Cheong S.-W. *"Ferroelectricity Induced by Acentric Spin-Density Waves in YMn_2O_5"* Phys. Rev. Lett. (2006), 96, 097601.

[28] Tokura Y., Shinichiro S. and Nagaosa N. *"Multiferroics of spin origin"* Rep. Prog. Phys. (2014), 77, 076501.

[29] Cheong S. W. and Mostovoy M. "Multiferroics: a magnetic twist for ferroelectricity" Nature Materials (2007), 6, 13-20.

[30] Halpern O. and Johnson M. H. "*On the Magnetic Scattering of Neutrons*" Phys. Rev. (1939) 55, 898.

7 Pb_2CoWO_6 (PCW)

7.1 Crystal structure at room temperature

PXRD measurements performed on the PCW sample at RT reveal the classical pattern of a double perovskite system with a superstructure related to the fundamental perovskite by the relations $\boldsymbol{a} = 2\boldsymbol{a}_p$, $\boldsymbol{b} = \sqrt{2}\boldsymbol{a}_p$, and $\boldsymbol{c} = \sqrt{2}\boldsymbol{a}_p$ ($\boldsymbol{a}_p \approx 3.9$Å), different from the one we previously found in Mn-containing compounds. However, some low intensity extra peaks were detected in ToF-NPD data collected at ISIS with HRPD and WISH instruments. These reflections revealed to be modulation satellites that can be indexed with a modulation vector $\kappa \approx (0.9\ 0\ 0.16)$, in agreement with the modulated structure already reported by Baltinozzi *et al.*[1] in the *I2/m(α0γ)0s* superspace groups, using position modulation, up to second harmonic, for all the atoms in the structure. Owing to the quality of the high resolution and high intensity data collected, we decided to re-determine the structure. The solution we obtained is in agreement with the one previously reported, the main differences being related to the type and the values of the modulated functions. Thanks to the high resolution of the HRPD data, it was possible to determine the absence of high order satellites in the neutron diffraction data. This simplified the structural model, by reducing the modulation parameters, giving rise to a stable refinement.

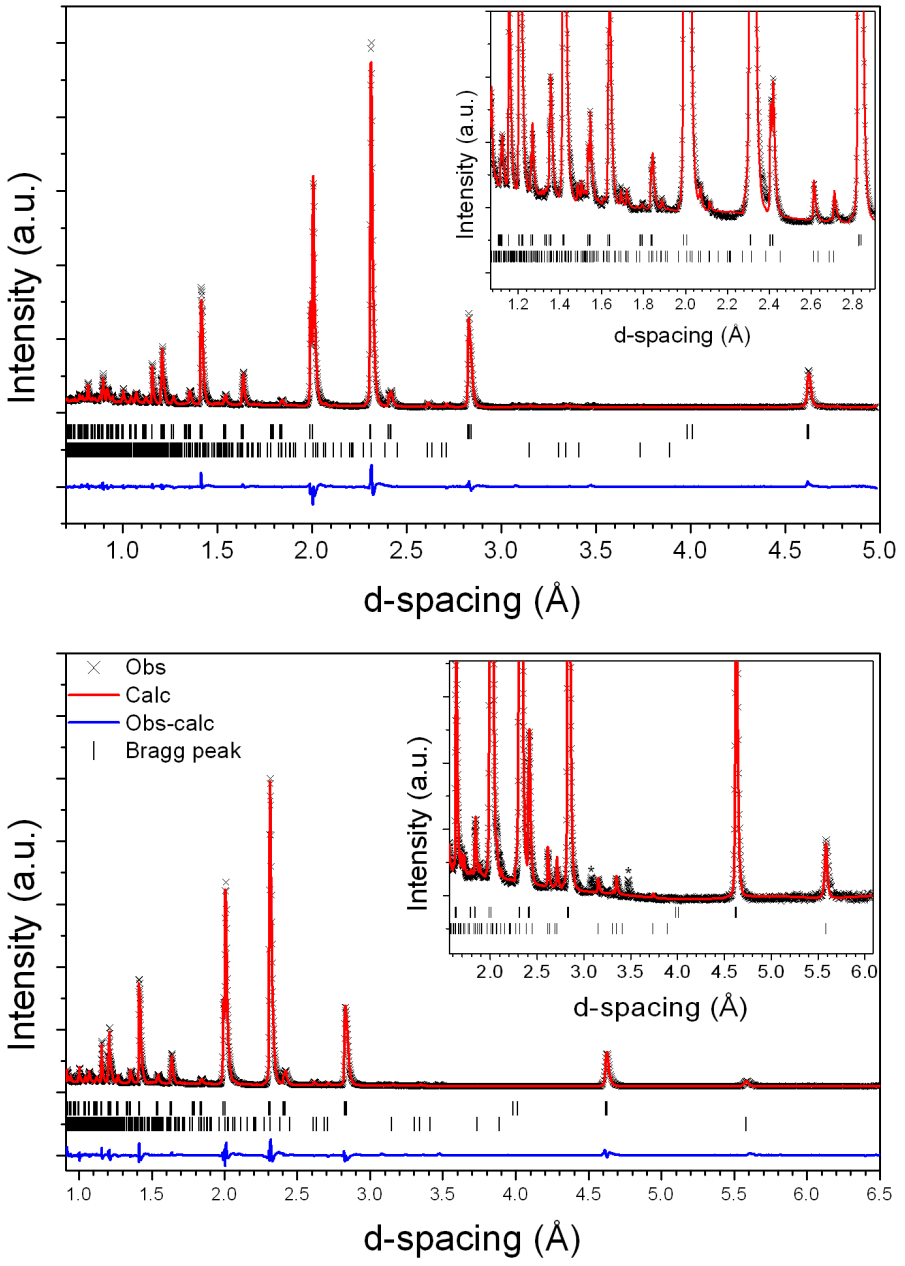

Figure 7-1 Rietveld plots for PCW data collected at RT on WISH 2θ=152.8 (top) and 90° (bottom) banks. Observed (×, black), calculated (line, red), and difference (line, blue) patterns are reported. Lower and upper tick marks indicate the main and first order satellite reflections; Pb_2WO_5 diffraction contributions are indicated by (*).

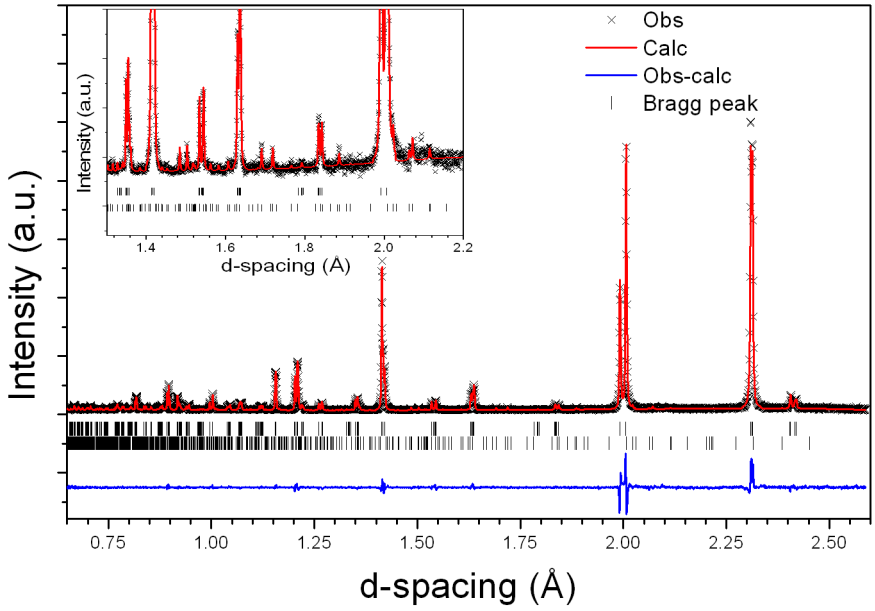

Figure 7-2 Rietveld plots of PCW data collected at RT on HRPD high-resolution bank. Observed (×, black), calculated (line, red), and difference (line, blue) patterns are reported. Lower and upper tick marks indicate the main and first order satellite reflections respectively.

The Rietveld plots, obtained thanks to the Jana2006 software,[2] showing good agreement between the observed and calculated data, are reported in figure 7-1 for the 2θ =152.8 and 90° WISH banks and in figure 7-2 for the high-resolution bank of HRPD. The average nuclear structure, shown in figure 7-3, is a monoclinic double perovskite with a NaCl like arrangement of the B site cations, without any detectable anti-site defects.

The lattice shows pseudo-symmetry, being the β angle very close to 90°. The symmetry reduction to monoclinic is mainly due to the B site ordering, not possible in the orthorhombic lattice with the observed superstructure. A remarkable tilt of the octahedra is detected along the ***a*** direction, whereas in the normal plane only a smaller distortion is required to accommodate the different size of the cations and the bond requirements of the lead atoms, which form five

short bonds ranging from 2.658(2) to 2.745(4) Å, generating a pyramidal coordination (figure 7-3).

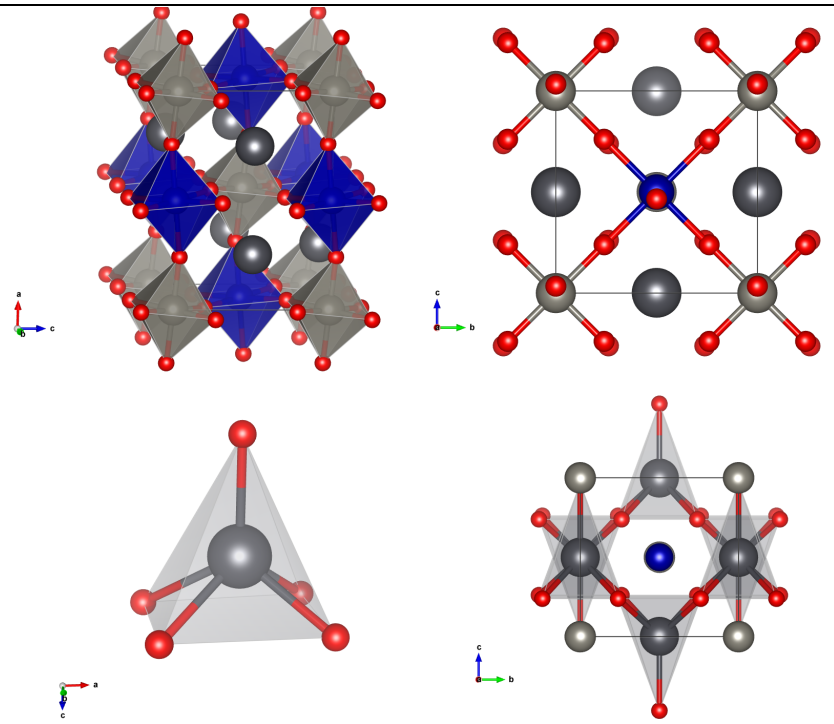

Figure 7-3 Top) Ball and stick representation of the PCW average structure at RT (black lead, blue cobalt, grey tungsten) pointing out the tilt of the octahedra along the ***a*** axis. Bottom) Coordination polyhedra of the lead atoms and relative orientation in the average nuclear structure.

In order to fit the experimental data, we introduced only positional modulation functions, expressed in Fourier series truncated at the first order, since, as previously stated, no satellite reflections of the second and/or higher orders were experimentally detected. We found that the introduction of positional modulation functions for the Co and W atoms does not improve the fit and introduces correlation between the parameters, so that the positional modulation was introduced only for lead and oxygen atoms. Refined coordinates of the basic structure, occupancies, atomic displacement parameters and the

symmetry permitted Fourier amplitudes of the modulation functions are reported in table 7-1 and 7-2 respectively.

Table 7-1 Crystal data and refinement reliability factors for Pb_2CoWO_6 at room temperature

Chemical Formula	Pb_2CoWO_6
Space Group	*12/m(α0γ)0s*
a(Å)	7.96894(5)
b(Å)	5.66976(5)
c(Å)	5.68384(5)
β(°)	89.974(3)
α	0.911(7)
γ	0.159(3)
Volume(Å^3)	256.807(4)

	HRPD 2θ=168.3°	**HRPD 2θ=89.6°**	**WISH 2θ=90°**	**WISH 2θ=121.66°**	**WISH 2θ=152.8°**	**Overall**
Gof	1.74	2.61	7.04	6.91	6.61	5.39
$R(F)_{obs}$	5.03	4.70	3.42	5.16	7.82	-
R_p	7.26	4.12	4.82	4.45	4.42	5.12
$_wR_p$	7.51	4.39	6.17	5.75	5.60	5.81

Table 7-2 Fractional atomic coordinates, atomic displacement parameters, occupancy factors and modulation parameters of the Pb_2CoWO_6 structure at RT.

	x	**y**	**z**	**Occupancy**	**U(Å^2)**
Pb	0.2525(7)	0.00	0.5013(3)	1	0.0278(3)
W	0.00	0.00	0.00	1	0.0095(9)
Co	0.5	0.00	0.00	1	0.026(2)
O1	0.2421(4)	0	0.0339(3)	1	0.0222(7)
O2	-0.01718(18)	0.2393(4)	0.2389(4)	1	0.0182(5)

Modulation parameters

	x sin	**y sin**	**z sin**	**x cos**	**y cos**	**z cos**
Pb	-	0.0037(10)	-	-	0.0267(4)	-
O1	-	-0.0079(13)	-	-	0.0167(7)	-
O2	0.0059(5)	-0.0061(10)	0.0011(9)	0.0017(3)	0.0206(6)	-0.0192(4)

The t-plots for the cations-oxygen bond lengths are shown in figure 7-4. The modulation concerns mainly the metal-O2 distance and the larger modulation is observed for the Pb-O2 bond length. This indicates that the bond requirements of the lead and the B site cations, which cannot be satisfied with a "simple" tilting of the octahedral network, is the driving force of the modulation. The complex bonds modulation is reflected in a variation of the in plane tilting angles, as indicated in the corresponding t-plot reported in figure 7-5.

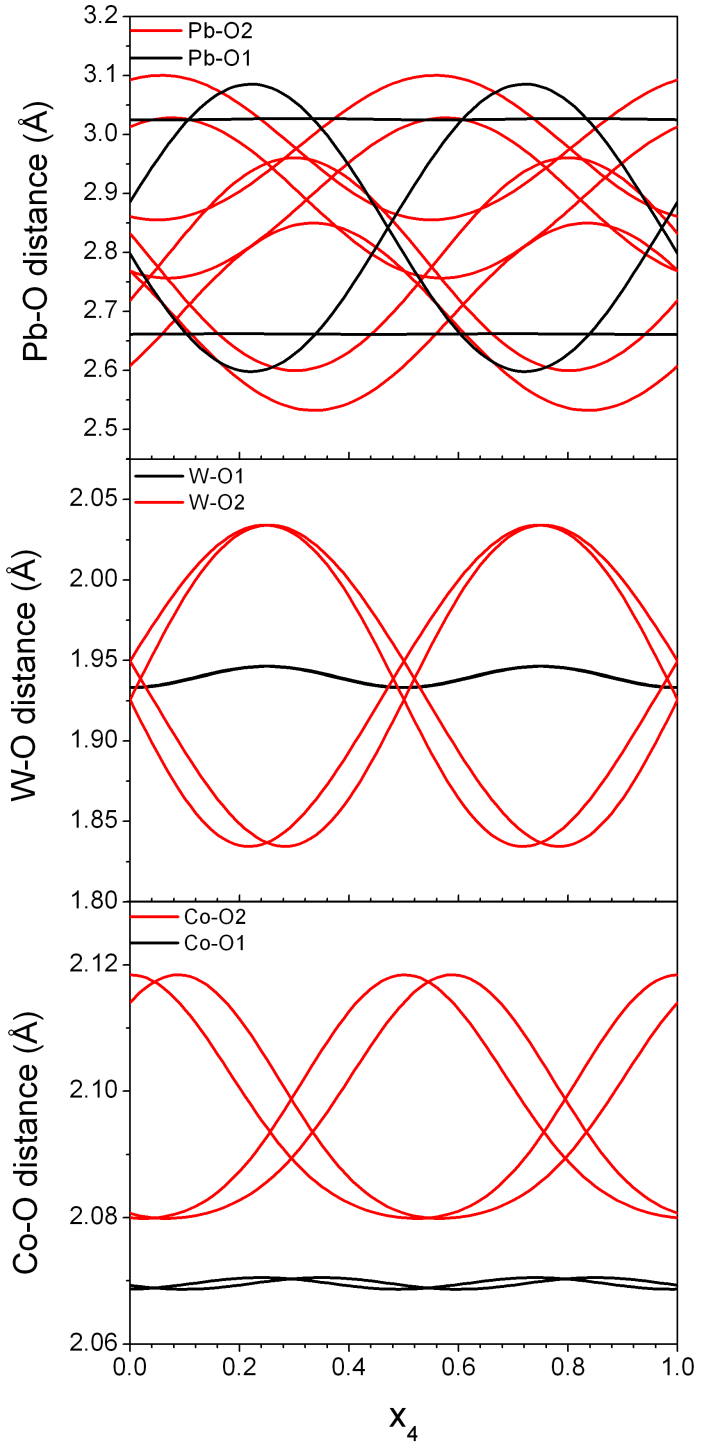

Figure 7-4 t-plot of the Pb-O, W-O and Co-O bond lengths.

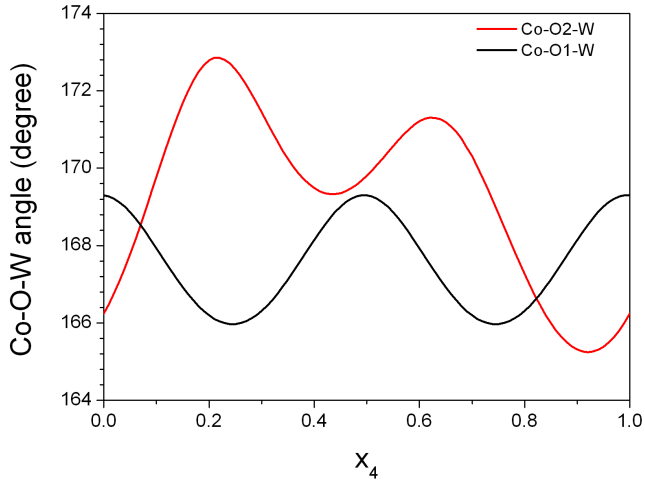

Figure 7-5 t-plot of the out of plane tilting angles (black line), and of the in plane tilting angles (red line).

7.2 Low temperature orthorhombic structure

On cooling, the PCW system undergoes a phase transition around 230 K. Below this temperature the diffraction pattern can be indexed with an orthorhombic superstructure related to the simple perovskite by the relations $\boldsymbol{a} = 2\boldsymbol{a}_p$, $\boldsymbol{b} = \sqrt{2}\boldsymbol{a}_p$, and $\boldsymbol{c} = 2\sqrt{2}\boldsymbol{a}_p$. The occurrence of a phase transition in this temperature range is confirmed also by the dielectric measurements performed on the sample. The temperature dependence of the dielectric constant, measured at different frequencies, is shown in figure 7-6, where a change of the behaviour of the relative dielectric constant is evident in the low frequency measurements. The transition has strong frequency dependence: it is shifted at higher temperature with the increase of the frequency and disappears for values higher of 800kHz. The strong dependence is probably related to the incommensurate character of the RT phase and in particular to the lead and oxygen modulations. The sudden drop of the dielectric constant, clearly visible at higher temperatures in the low frequency measurements, is related to the further phase transition

from the RT structure to the cubic elpasolite-type structure, confirmed by PXRD measurements.

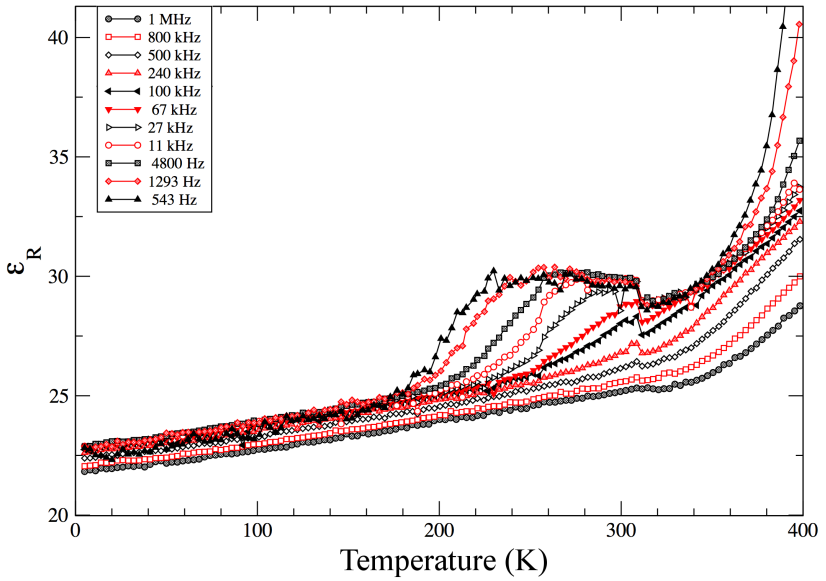

Figure 7-6 Dielectric measurements of the PCW sample at different frequencies. The measurement were performed on a planar capacitor of thickness t= 0.48 mm and area A= 9 mm^2, using mica linings to avoid contacts effects.

The orthorhombic structure observed below 230 K is isostructural with $Pb_2Mn_{0.6}Co_{0.4}WO_6$, showing the centrosymmetric space group *Pmcn*. The structure was refined using ToF-NPD data from the high-resolution bank of the HRPD instrument and of the WISH instrument bank with $2\theta = 58.3°$, 90°, 121.6° and 152.8°, using the Jana2006 software.[2] The Rietveld plot of selected banks are reported in figure 7-7 showing a good agreement between the observed and calculated data. The crystal data and reliability factors are reported in table 7-3, whereas atomic coordinates, occupancies and atomic displacement parameters are reported in table 7-4. Selected bond lengths and angles are reported in table A-5 in appendix.

Table 7-3 Crystal data and refinement reliability factors for Pb_2CoWO_6 at 150K

Chemical Formula	Pb_2CoWO_6
Space Group	*Pmcn*
a(Å)	7.9434(5)
b(Å)	5.7039(7)
c(Å)	11.4397(13)
Volume(Å^3)	518.30(5)

	HRPD 2θ=168.3°	**WISH 2θ=58.3°**	**WISH 2θ=90°**	**WISH 2θ=121.66°**	**WISH 2θ=152.8°**	**Overall**
Gof	2.01	7.34	9.88	11.52	12.32	8.9
$R(F)_{obs}$	6.51	3.40	3.40	3.52	3.72	-
R_p	3.41	3.89	5.24	5.55	5.26	4.21
$_wR_p$	4.29	4.39	6.55	7.24	7.08	6.61

Table 7-4 Fractional atomic coordinates, atomic displacement parameters and occupancy factor of the PCW sample at 150 K.

	x	**y**	**z**	**Occupancy**	**U(Å^2)**
Pb	0.01176(15)	0.2829(3)	0.14243(8)	1	0.0110(4)
W	0.25	0.7437(10)	0.1203(5)	1	0.0034(10)
Co	0.25	0.221(2)	-0.1112(11	1	0.018(3)
O1	0.0093(4)	0.7315(4)	0.13376(16)	1	0.0208(6)
O2	0.25	-0.0162(11)	0.0118(5)	1	0.0205(10)
O3	0.25	0.5179(10)	-0.0023(5)	1	0.0126(8)
O4	0.25	-0.0379(9)	0.2563(4)	1	0.0124(16)
O5	0.25	0.4787(10)	0.2363(4)	1	0.0232(17)

Owing to their stereoactive character, the lead atoms form with the surrounding oxygen four short bond ranging from 2.446(3) to 2.590(3) Å opposite to the lone-pair. The displacements of the cations (figure 7-8) from the centre of the coordination polyhedra are arranged in an antipolar way similarly to the $Pb_2Mn_{0.6}Co_{0.4}WO_6$ compound.

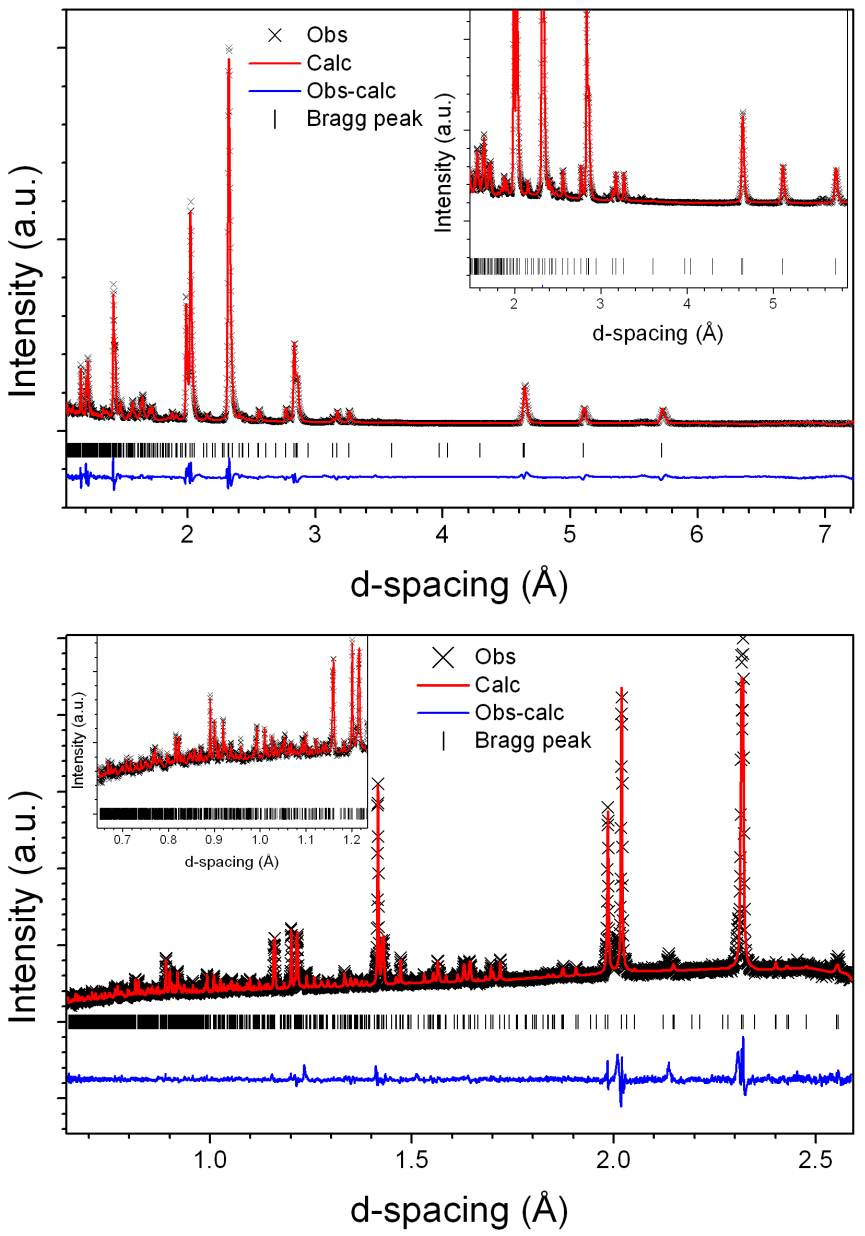

Figure 7-7 Rietveld plots of PCW at 150 K: WISH data 2θ= 90° (top) and HRPD high-resolution bank (bottom). Observed (×, black), calculated (line, red), and difference (line, blue) patterns are reported. The tick marks indicate the position of the Bragg reflections.

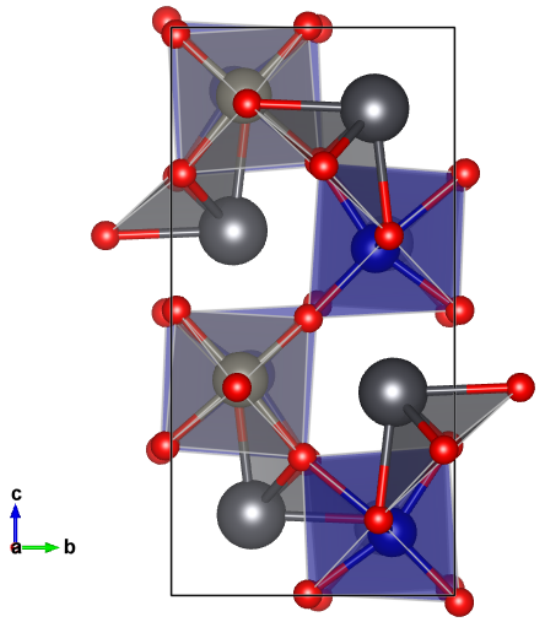

Figure 7-8 ***bc*** plane of the orthorhombic phase at 150 K. Black spheres represent the lead atoms, showing four short bond with the surrounding oxygen atoms (red). The blue and grey octahedra represent the coordination of cobalt and tungsten atoms respectively.

The tungsten coordination polyhedron is quite regular showing a small C_4 type[3] distortion with one short (1.848(8) Å) and one long (2.012(8) Å) bonds. The cobalt octahedron is more distorted, showing four almost equivalent bonds ranging from 2.082(13) to 2.103(13) Å, one short bond (1.952(14) Å) and a very long one (2.360(13) Å). This strong C_4 distortion[3] leads to a pseudo square pyramidal coordination of the Co^{2+} atoms, quite uncommon in double perovskites systems, which suggests a certain degree of covalence in the Co-O bond. The short bonds with oxygen of both B and B' sites are aligned along the [0 1 2] direction and are rotated by 90° respect to the neighbour sites, generating an antipolar distortion. The structural distortions suggest that the compound could be an antiferroelectric material, even if other electrical characterizations are needed to confirm this claim.

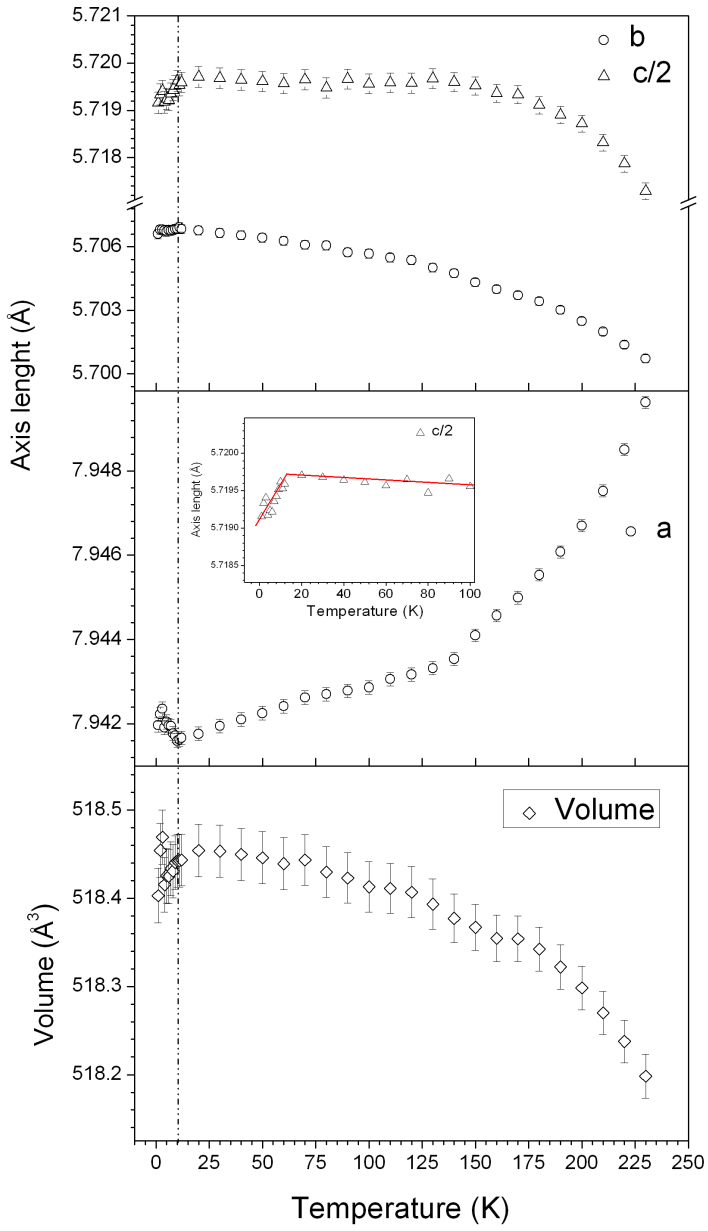

Figure 7-9 Thermal evolution of the lattice parameters and cell volume of the PCW orthorhombic phase. The dotted line indicates the temperature below which there is the appearance of the magnetic reflections. Inset) low temperature region of the ***c*** axis evolution showing the abrupt change of the thermal expansion coefficient.

The thermal evolution of the orthorhombic cell parameters, obtained from the WISH ToF-NPD data, is reported in figure 7-9. While ***a*** shows the classical thermal behaviour with a positive expansion coefficient at least down to 10 K, ***b*** and ***c*** show, as in PMW and PMCW_50, a negative thermal coefficient; since the main cationic shifts lie in the latter plane, this is probably related to an increase of the antiferroelectric distortion with decreasing the temperature. It is interesting to note that the latter aspect predominates, so that the system shows a negative thermal expansion coefficient of the cell volume. At 10 K some anomalies in the thermal behaviour of the cell parameters are observed. In particular the ***c*** axis shows an abrupt change of the thermal coefficient at this temperature (see inset of figure 7-9) and at the same time the ***a*** axis changes is expansion coefficient in the opposite way. Since at the same temperature some extra peaks, whose thermal behaviour suggests a magnetic nature, appear in the neutron diffraction pattern, this could indicate the presence of a strong magneto-striction effect in the system.

7.3 Magnetic structure and properties

ZFC and FC magnetization measurements, shown in figure 7-10, pointed out a magnetic transition around 10 K. The transition shows in the FC measurement a ferromagnetic character, whereas in the ZFC measurement a peak ascribable to an antiferromagnetic ordering is present. From the fit of the paramagnetic region of the inverse susceptibility with a Curie-Weiss law was obtained a $\Theta_{C\text{-}W}$ = -17(5) K that indicates a general antiferromagnetic character of the exchange interactions. The value of the effective moment μ_{eff} = 4.5(3) μ_B is quite high for Co^{2+} in spin only configuration, indicating an unquenched orbital momentum. Since the crystal field of the highly distorted octahedron removes the degeneracy of the *d*-orbitals, the unquenched orbital momentum should originate from the spin orbit coupling of the Co^{2+} ion. In literature are

present some example of double perovskites showing Co^{2+} with unquenched orbital momentum.[4-5]

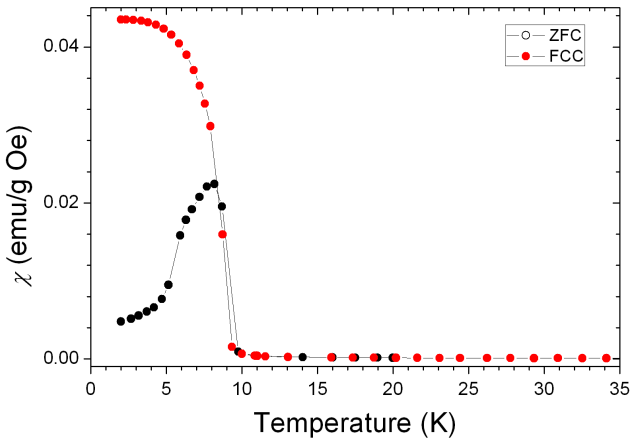

Figure 7-10 ZFC and FC magnetization measurement of PCW performed by means of a SQuiD magnetometer with an applied field of 50 Oe; only the 2 -35 K region is shown, for higher temperatures the ZFC and FC measurements are perfectly superimposed and follow a Curie-Weiss law.

Extra reflections ascribable to long range magnetic ordering appear below 10 K in the ToF-NPD data collected at WISH. The pure magnetic reflections can be indexed with a slightly incommensurate propagation vector κ_1=(½ ½-δ 0), but magnetic intensity detected on the nuclear reflections indicates the presence of the additional propagation vector κ_2 = (0 0 0). The magnetic structure was solved by means of the superspace formalism and the possible superspace groups were found by means of the Isotropy subgroups[6] combining the two propagation vectors; the obtained subgroups with the corresponding systematic absences are reported in table A-6 in appendix. All the possible subgroups that satisfy the systematic absence for the average magnetic structure[7-9] were tried and the best solution was found in the *Pm'c2$_1$'(½ β 0)000* corresponding to the irreducible representations mGM2+ ⊕ mH1 with order parameter direction P1-P (a;b,b,0,0). The lower symmetry groups doesn't give

better solutions; on the contrary the symmetry reduction makes the refinement unstable and the obtained solutions are qualitatively similar to the *Pm'c2$_1$'(½β 0)000* ones. The structure refinement was performed on the data collected on the WISH bank with 2θ= 154.8°, 121.6°, 90°, 58.3°, 27.8° and on the HRPD ones with 2θ=168 and 90° by means of the Jana2006 software.[2] Crystal data and reliability factors of the refinement at 2 K are reported in table 7-5, whereas atomic coordinates in the new subgroups obtained from the *Pmcn* structure refined at 12 K are reported in table A-7 in the appendix. The Rietveld plot of some selected banks are reported in figure 7-11. The refined moments of the basic structure and the amplitude of the modulation functions are reported in table 7-6. The missing components were imposed to zero. In some case this was required by symmetry constrains and in others it was suggested by the refinement on approaching convergence.

Table 7-5 Crystal data and refinement reliability factors for Pb_2CoWO_6 at 2K

Chemical Formula	Pb_2CoWO_6
Space Group	*Pm'c2$_1$'(1/2β0)000*
a(Å)	7.94913(8)
b(Å)	5.71196(9)
c(Å)	11.44791(18)
β	0.4945(6)
Volume(Å^3)	519.794(13)

	HRPD 2θ =168°	**HRPD 2θ=90°**	**WISH 2θ=27.8°**	**WISH 2θ=58.3°**	**WISH 2θ=90°**	**WISH 2θ=152.8°**	**Overall**
Gof	1.91	4.40	1.95	7.96	10.96	14.21	7.93
R(F)$_{obs}$	5.20	4.51	6.91	4.15	4.31	4.04	-
R$_p$	3.23	3.16	2.71	4.85	5.66	5.99	3.37
$_w$R$_p$	4.07	4.31	1.81	6.18	7.27	7.80	6.59

Table 7-6 Magnetic parameter of the incommensurate structure at 2 K. The parameters not shown are zero from symmetry or constrained to zero by as indicated from the refinement approaching convergence.

	$M_{y,0}$ (μ_B)	**$M_{z,0}$ (μ_B)**	**$M_{x,cos1}$ (μ_B)**	**$M_{z,sin1}$ (μ_B)**
Co1	1.696(17)	-2.429(13)	-	1.78(3)
Co2	1.696(17)	2.429(12)	1.780(18)	-

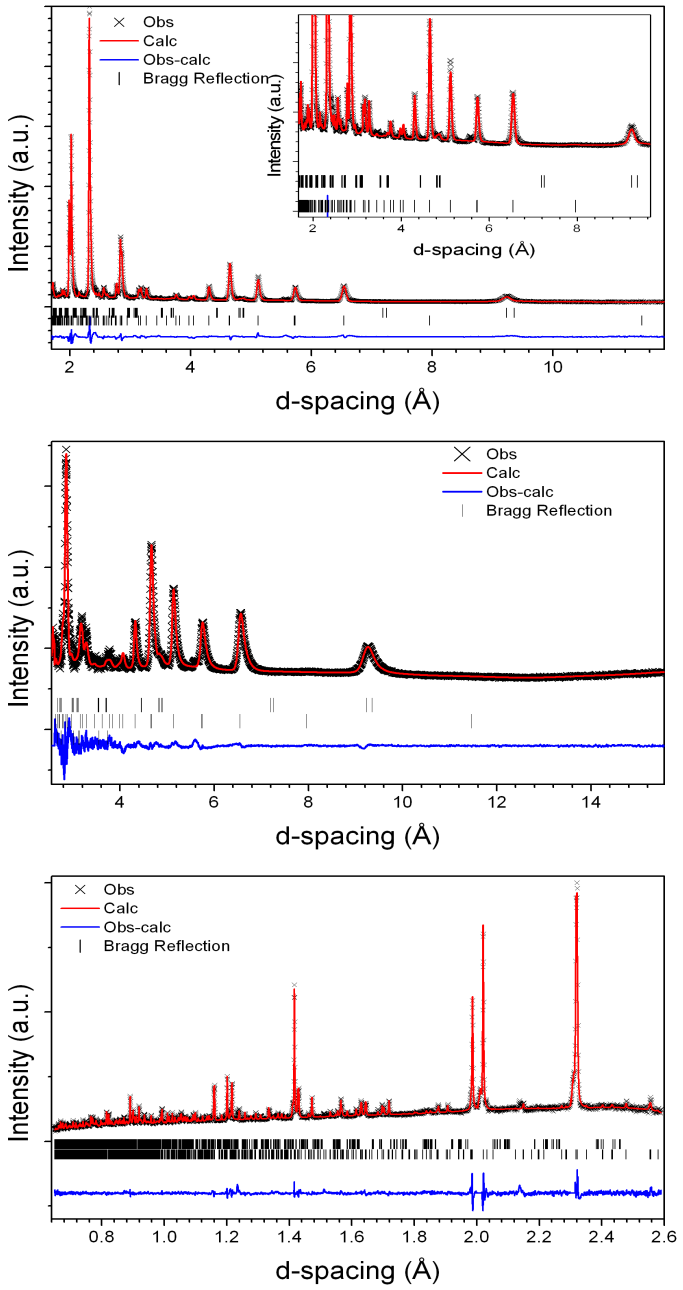

Figure 7-11 Rietveld plots for PCW at 2 K: WISH data 2θ= 58.3 (top), 27.0° (middle), HRPD high-resolution bank (bottom). Observed (×, black), calculated (line, red), and difference (line, blue) patterns are reported. Lower and upper tick marks indicate the Bragg positions of the main and first order satellite reflections respectively.

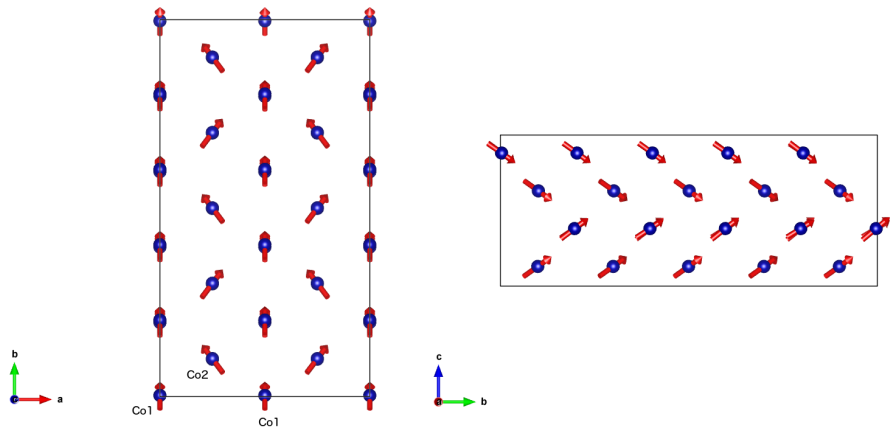

Figure 7-12 Magnetic incommensurate structure representation in a commensurate supercell 2***a*** x 5***b*** x ***c***. The magnetic moments of the Co1 planes are constrained in the ***bc*** plane, whereas the Co2 moments are alternatively canted from this plane.

The nearly commensurate character of the propagation vector makes difficult to display the magnetic structure, unless to take into account a very high number of fundamental cells. A commensurate supercell with dimension 2***a*** x 5***b*** x ***c*** is shown in figure 7-12. The Co1 atoms have a moment that lie on the ***bc*** plane and possesses a sinusoidal modulation of the *z* component along the ***b*** axis. On the contrary, the Co2 atoms have a co-sinusoidal modulation of the *x* component of the magnetization that tilt the magnetic moment from the ***bc*** plane. The canting angle from this plane change with the propagation vector along the ***b*** direction. A supercell with dimension 2***a*** x 60***b*** x ***c***, able to display the modulation of the canting angle, is shown in figure 7-13. A progressive reduction of the canting angle leading to its inversion, giving an "x-shape" to the magnetic moments, results evident from the figure. A further interesting feature of the structure is the ferromagnetic component along the ***a*** direction. This is in agreement with the magnetization measurements showing in the FC curve a clearly indication of ferromagnetism. In the other two directions the magnetic coupling are essentially antiferromagnetic (AF), confirming that the average magnetic interaction are AF as suggested from the value of the $\Theta_{C\text{-}W}$.

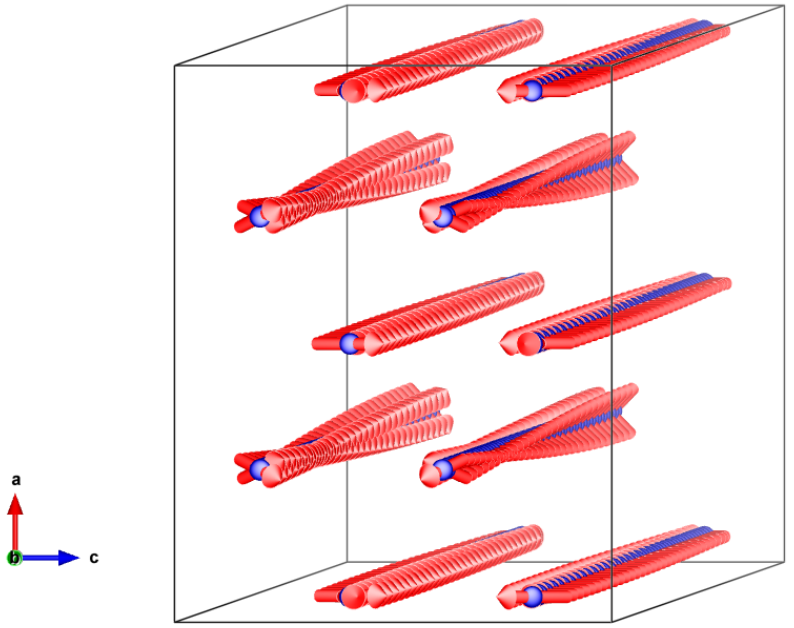

Figure 7-13 Magnetic incommensurate structure representation in a supercell 2***a*** x 60***b*** x ***c***. The modulation of the spins is evident from the "x-shape" of the Co2 plane in witch the canting angle from the ***bc*** plane have a sinusoidal modulation. In the same way the Co1 plane shows a sinusoidal modulation of the z component.

The refined value of the magnetic moment for both cobalt atoms are in agreement with the value of the effective magnetrons obtained from the fit of the inverse susceptibility. Figure 7-14 shows the t-plot of the magnetic moments that does not exceed the value of $\mu_{eff} = 4.5(3)\ \mu_B$. Finally is worthy to underline that, similarly to the case of $Pb_2Mn_{0.6}Co_{0.4}WO_6$, the symmetry reduction at the magnetic transition implies the removing of the inversion centre. This allows the generation of a spontaneous electrical polarization in the system, making PCW a type II multiferroics below 10 K. Furthermore the evidence, from the thermal evolution of the cell parameters, of a strong magnetostrictive effect at the magnetic transition is indicative of a spin lattice coupling in the compound.

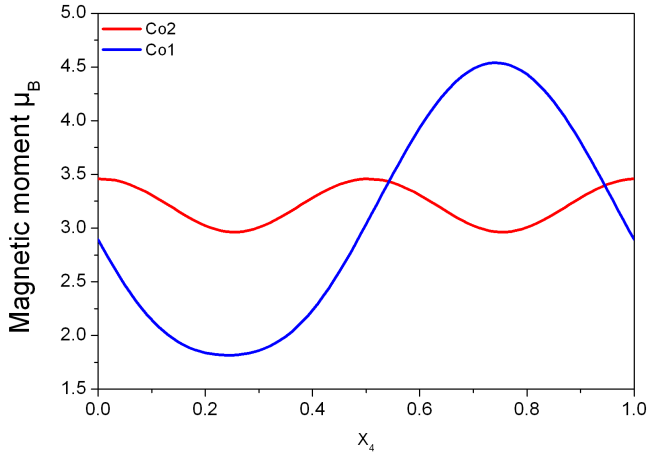

Figure 7-14 t-plot of the magnetic moment for both cobalt atoms.

7.4 Conclusion

This chapter presents the structural characterization of Pb_2CoWO_6. The modulated RT structure was already known in literature,[1] but the new, high quality data we collected were able to confirm the modulation vector and the superspace group already reported, pointing out however the absences of modulation for the Co and W atoms in the system and the lack of high order satellites, leading to a more simple structure definition.

The system undergoes at 230 K a phase transition to a centrosymmetric orthorhombic structure, iso-structural with PMCW_50. The ToF-NPD data indicate the establishing of a long-range magnetic order in the system below 10 K. The magnetic structure is incommensurate showing a complex sinusoidal modulation of the magnetic moments. The magnetic transition reduces the system symmetry removing the spatial inversion symmetry allowing the possible formation of a spontaneous electrical polarization indicated also from the strong magnetostrictive effect observed in the thermal evolution of the cell parameters.

7.5 Reference

[1] Baldinozzi G, Calvarin G, Sciau P, Grebille D, Suard E. "*Neutron Rietveld refinement of the incommensurate phase of the ordered perovskite Pb_2CoWO_6.*" Acta Cryst. (2000). B56, 570-576.

[2] Petricek, V.; Dusek, M.; Palatinus, L. "*Crystallographic Computing System JANA2006: General features*" Z. Kristallogr. (2014), 229, 345– 352

[3] Halasyamani P. S. *"Asymmetric Cation Coordination in Oxide Materials: Influence of Lone-Pair Cations on the Intra-octahedral Distortion in d^0 Transition Metals"* Chem. Mater. (2004), 16, 3586−3592.

[4] Viola M. C., Martınez-Lope M. J., Alonso J. A., Martınez J. L., De Paoli J. M., Pagola S., Pedregosa J. C., Fernandez-Dıaz M. T. and Carbonio R. E. *"Structure and Magnetic Properties of Sr_2CoWO_6: An Ordered Double Perovskite Containing Co2+(HS) with Unquenched Orbital Magnetic Moment"* Chem. Mater. (2003), 15, 1655-1663.

[5] Blanco M. C., De Paoli J. M., Ceppi S., Tirao G., Nassif V. M., Guimpel J. and Carbonio R. E *"Synthesis, structural characterization and magnetic properties of the monoclinic ordered double perovskites $BaLaMSbO_6$, with M = Mn, Co and Ni"* J. of Alloys and Compounds (2014), 606, 139-148.

[6] Campbell B. J., Stokes H. T., Tanner D. E. and Hatch D. M., *"ISODISPLACE: An Internet Tool for Exploring Structural Distortions."* J. Appl. Cryst., (2006) 39, 607-614.

[7] Gallego S. V., Tasci E. S., de la Flor G., Perez-Mato J. M. and M. I. Aroyo *"Magnetic symmetry in the Bilbao Crystallographic Server: a computer program to provide systematic absences of magnetic neutron diffraction"* J. Appl. Cryst. (2012), 45(6), 1236-1247.

[8] Aroyo M. I., Perez-Mato J. M., Orobengoa D., Tasci E., de la Flor G. and Kirov A. *"Crystallography online: Bilbao Crystallographic Server"* Bulg. Chem. Commun. (2011), 43(2), 183-197.

[9] Aroyo M. I., Perez-Mato J. M., Capillas C., Kroumova E., Ivantchev E., Madariaga G., Kirov A. and Wondratschek H. *"Bilbao Crystallographic Server I: Databases and crystallographic computing programs"* Z. Krist. (2006), 221, 1, 15-27.

8 Conclusions

In the previous chapters of this thesis, the properties of the two end members and of an intermediate composition (x=0.4) of the $Pb_2Mn_{1-x}Co_xWO_6$ solid solution were described in detail. These three compounds show very different structure evolution and in particular completely different magnetic ground states. Starting from the analysis of the room temperature structure, Pb_2MnWO_6 (PMW) shows a non-centrosymmetric structure with space group $Pmc2_1$. The combined refinement from neutron and synchrotron data and the complete electrical characterization allowed establishing the ferrielectric character of the system. The electrical nature of the system is mainly characterized by the presence of two Pb sublattices with different coordination polyhedra producing local electrical dipoles. The two sublattices are grossly coupled in an antipolar way but, being unbalanced, they give rise to an electrical polarization along the ***c*** axis of the structure. The ferrielectric structure is stable in a wide temperature range, i.e. from 450 K, the para-ferrielectric transition temperature, down to 2 K. $Pb_2Mn_{0.6}Co_{0.4}WO_6$ (PMCW_50) shows on the contrary a centrosymmetric structure with *Pmcn* space group. In this structure all the Pb atoms have the same distorted PbO_4E (E = lone pair) coordination, but the local dipoles generated from the asymmetric coordination are coupled in an antiferroelectric structure. The other end member, Pb_2CoWO_6 (PCW), shows at room temperature an incommensurate modulated structure with modulation

vector $\kappa \approx (0.9\ 0\ 0.16)$; the incommensurate structure is basically a modulation of the in-plane tilting angle between the CoO_6 octahedra. By cooling, the modulation is removed and PCW undergoes to a phase transition to an orthorhombic structure basically iso-structural with the PMCW_50 RT one, with the Co ions in pseudo square pyramid coordination.

The magnetic properties change significantly along the solid solution; in particular the three analysed compounds show three different magnetic ground states. PMW displays two different magnetic transitions at 45 K and 8 K. The first transition is characterized by the establishment of short-range interactions, ascribed to Mn-O-Mn exchange interactions generated by anti phase boundary (APB) defects. Below 8 K the systems undergoes a transition to a long range magnetically ordered state with propagation vectors $\kappa_1 = (0\ 0\ 0)$ and $\kappa_2 = (¼\ 0\ 0)$. The first transition is suppressed in the other end member, that shows only a unique long range order transition at 10 K, with a ferromagnetic component; the neutron diffraction data indicate a complex incommensurate structure with propagation vectors $\kappa_1 = (0\ 0\ 0)$ and $\kappa_2 = (½\ ½\text{-}\delta\ 0)$. PMCW_50 shows a more complex magnetic behaviour. Like in case of PMW, a first transition showing a weak ferromagnetic character is observed, even if at a much higher temperature (190 K), followed by a second transition around 9 K. The neutron diffraction experiment shows below 190 K a diffuse scattering and a dependence of the paramagnetic background on temperature, indicating a progressive evolution of the exchange interactions. Even in this case the origin of the high temperature transition may be ascribed to APB's, but differently from the case of PMW, three different exchange iterations are statistically present in PMCW_50: Mn-O-Mn, Co-O-Co and Mn-O-Co. Among these, the latter is responsible for the increase of the transition temperature, being the effects of the other two known by the behaviour of the end members. However, the different characteristic temperatures of the interactions can explain the complex behaviour of the paramagnetic background and of the diffuse scattering. Below 9 K the systems undergoes a long-range magnetic transition and the magnetic reflections

observed in the diffraction pattern can be index with propagation vectors κ_1= (0 0 0) and κ_2 = (½ 0 0). The observed collinear magnetic structure removes the inversion centre and allows a spontaneous electrical polarization via symmetric exchange striction mechanism confirmed by the observation, in the pyrocurrent measurements, of two peaks in correspondence of the magnetic transition temperatures.

To better study the exchange interactions, two new intermediate composition of the solid solution, namely with the 25 % (PMCW_25) and 75 % (PMCW_75) of Co, were synthetized. The characterizations of these two new compounds are still preliminary, but some significant results we obtained are useful to construct a multiferroic phase diagram of the system. The ZFC and FC magnetization measurements of the two new compounds, carried out by means of a SQuiD magnetometer between 2 and 300 K, are reported in figure 8-1, compared with those of PMW and PMCW_50. The PMCW_25 system shows at least two critical temperatures: the first one at 190 K, in analogy with the PMCW_50 compound, and a second magnetic transition around 70 K. The transitions are clearly visible in both ZFC and FC measurements. By the hysteresis loop obtained at 2 K (not shown) a small coercive field is detected, indicating a weak ferromagnetic component. Even PMCW_75 shows two critical temperatures, at 190 K and at 9 K, similarly to the case of PMCW_50. The second magnetic transition shows a cusp characteristic of an antiferromagnetic ordering. The irreversibility between ZFC and FC measurements indicates a weak ferromagnetism confirmed also in this compound by hysteresis loop measurement. It is worthy to note that the first magnetic transition at 190 K is present in all the compositions containing both Co and Mn in the B site but that the value of the susceptibility increases up to the x= 0.4 compound and then decreases. These features confirm that this transition is related to the Mn-O-Co interaction in the APB's, that are statistically more probable in the PMCW_50 compound.

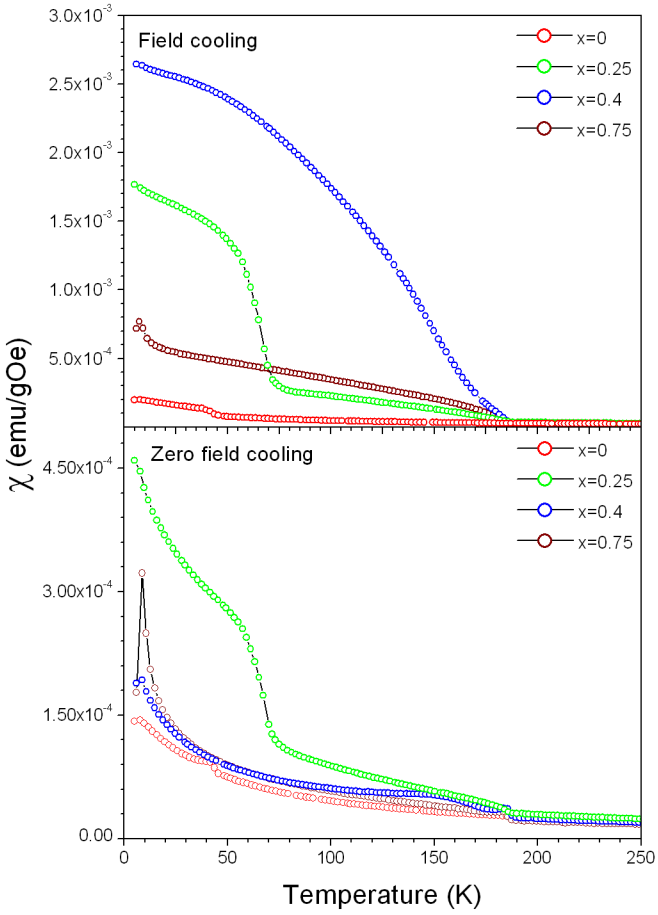

Figure 8-1 FC (top) and ZFC (bottom) measurements for the $Pb_2Mn_{1-x}Co_xWO_6$ solid solution systems.

To better study the magnetic transition observed in the two new compositions ToF-PND experiments were performed at the WISH instrument at the ISIS facility. The high d-spacing part of the diffraction pattern obtained at 1.5 K for all the compounds are compared in figure 8-2.

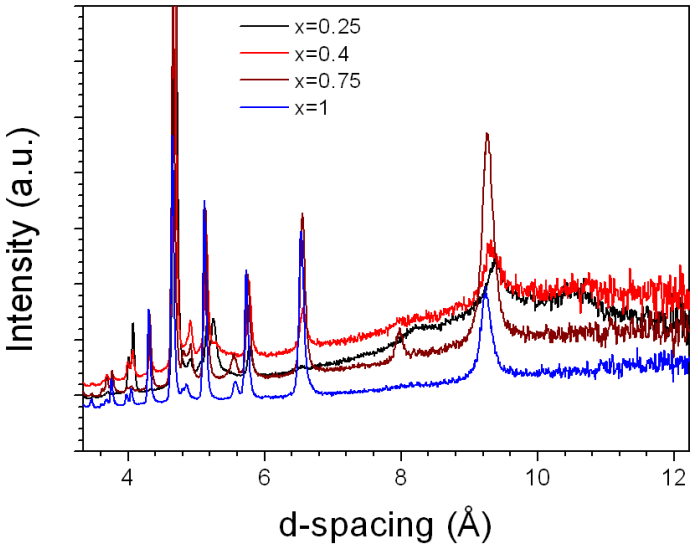

Figure 8-2 High d-spacing region of the time of flight neutron diffraction data from the WISH instrument for the $Pb_2Mn_{1-x}Co_xWO_6$ solid solution compounds.

Is evident that all the compounds show different magnetic ground states indicating that the substitution of Mn atoms with Co ones completely changes the magnetic interactions and lead to different magnetic properties. PMCW_25 does not show magnetic diffraction peaks down to 1.5 K, pointing out the absence of long-range ordered phases, but it is characterized by a strong diffuse scattering at high d-spacing indicating short-range order. On the contrary, PMCW_75 behaves like the other studied composition, showing diffuse scattering below the first magnetic transition, and the appearance of magnetic reflections below 9 K, indicating a long-range magnetic ordering below this temperature. The magnetic structure was not yet solved, but some preliminary considerations could be advanced. In particular the propagation vectors result to be very similar to those of PCW but, as can be deduced from figure 8-2, the relative intensities of the Bragg reflections are different, indicating a change in the spin arrangement.

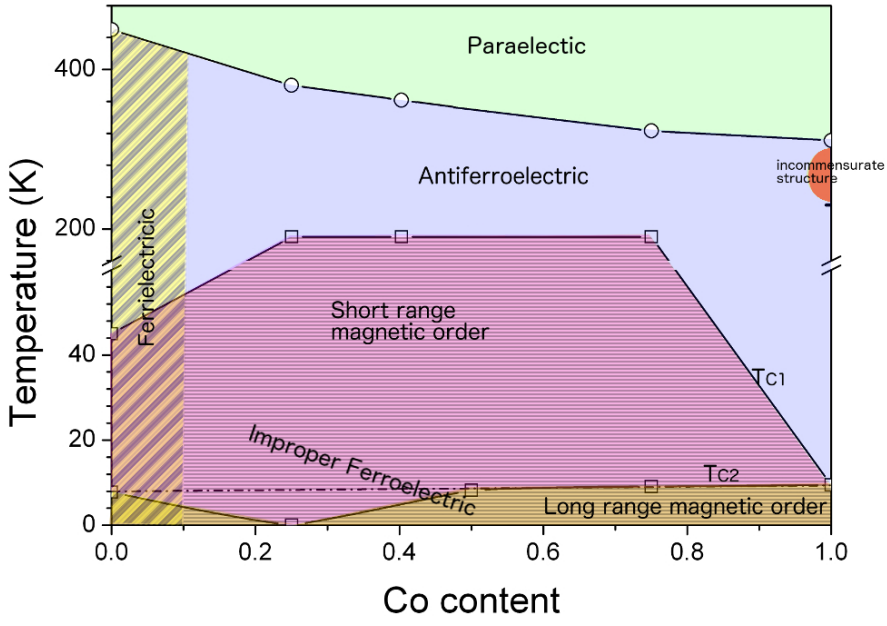

Figure 8-3 Multiferroic phase diagram of the $Pb_2(Mn,Co)WO_6$ system.

Even if the electric and magnetic characterization of the $Pb_2(Mn,Co)WO_6$ system has not been completed, the studies performed in this work make possible to sketch the multiferroics phase diagrams of the system that is shown in figure 8-3. Starting from the electrical properties, the system shows a ferrielectric character in the Mn rich region. By increasing the cobalt content, the system became antiferroelectric, at least in the paramagnetic temperature range. The transition temperature to the cubic phase, related to paraelectric state, decreases monotonically with the Co content. From the magnetic point of view, all the compositions sufficiently rich in both Mn and Co to present Mn-O-Co exchange interactions at the APB's show a first magnetic transition at 190 K. Pyrocurrent measurements indicate a polarization changes at this temperature, indication of a possible improper ferroelectric state below this temperature induced by the short range magnetic ordering. The symmetry analysis, performed on the intermediate PMCW_50 compound and on the pure-cobalt end member, confirmed an improper ferroelectric state below 10 K, where

both these systems undergo the breaking of both time and spatial inversion symmetry at the long range order magnetic transitions.

In conclusion, the $Pb_2(Mn,Co)WO_6$ system can be considered a good example to illustrate as a double perovskite structure can allow a fine tuning of the physical properties by chemical substitution of the B site cations. The introduction of cobalt in the system changes the magnetic exchange interactions and reduces the ferrielectric distortion of the PMW systems leading from a ferrielectric to an antiferroelectric structure. However the small spin-orbit coupling of the Co atom allow the establishment of a strong-spin lattice coupling that generate a type II multiferroics state below the magnetic transition temperatures.

Furthermore, this thesis offers an example of the symmetry analysis in these systems, where in particular the use of the magnetic space groups and of the superspace formalism allows a deep comprehension of the properties related to ferroic orders and of the relation between them, indicating the magnetic symmetry as a fundamental rule in the study of multifunctional materials.

9 Appendix

Table A- 1 List of selected bond lengths (Å) and angles (degrees) of the Pb_2MnWO_6 compound at RT.

	Bond length (Å)		Bond angle (°)
Pb1-O1	2.923(10)	**O3-Mn1-O4**	85.3(6)
Pb1-O2	3.066(10)	**O4-Mn1-O8**	108.2(6)
Pb1-O3	3.000(10)	**O3-Mn1-O6**	85.0(6)
Pb1-O4	3.216(12)	**O6-Mn1-O8**	81.6(6)
Pb1-O5	3.063(9)	**O9-Mn1-O9**	165.0(5)
Pb1-O6	2.583(9)	**O1-W1-O5**	88.4(6)
Pb1-O7	2.567(10)	**O1-W1-O10**	90.7(5)
Pb1-O7	3.284(11)	**O2-W1-O10**	82.4(5)
Pb1-O8	3.233(9)	**O2-W1-O5**	98.4(6)
Pb1-O9	3.307(10)	**O9-W1-O9**	166.8(4)
Pb1-O9	2.493(10)	**O1-Mn2-O2**	79.6(6)
Pb1-O10	2.575(8)	**O1-Mn2-O5**	94.4(7)
Pb2-O1	2.871(10)	**O2-Mn2-O10**	91.9(7)
Pb2-O2	2.555(9)	**O5-Mn2-O10**	94.1(6)
Pb2-O3	2.775(10)	**O7-Mn2-O7**	166.8(8)
Pb2-O4	2.969(11)	**O3-W2-O4**	101.1(6)
Pb2-O5	3.138(10)	**O3-W2-O8**	75.2(5)
Pb2-O6	3.022(10)	**O4-W2-O6**	93.1(6)
Pb2-O7	2.595(10)	**O6-W2-O8**	90.6(5)
Pb2-O7	3.195(11)	**O7-W2-O7**	162.5(5)
Pb2-O8	2.366(7)		
Pb2-O9	2.711(9)		
Pb2-O9	3.146(10)		
Pb2-O10	2.977(8)		
Mn1-O3	2.184(17)		
Mn1-O4	2.147(17)		
Mn1-O6	2.361(16)		
Mn1-O8	2.112(15)		
Mn1-O9(X2)	2.133(8)		
W1-O1	1.884(14)		
W1-O2	1.947(16)		
W1-O5	1.802(12)		
W1-O9(X2)	1.917(8)		
W1-O10	2.091(12)		
Mn2-O1	2.191(17)		
Mn2-O2	2.273(18)		
Mn2-O5	2.196(17)		
Mn2-O7(X2)	2.159(8)		
Mn2-O10	2.078(17)		
W2-O3	1.889(14)		
W2-O4	1.805(14)		
W2-O6	1.928(15)		
W2-O7(X2)	1.896(8)		
W2-O8	2.134(11)		

Table A- 2 List of selected bond lengths (Å) and angles (degrees) of the $Pb_2Mn_{0.6}Co_{0.4}WO_6$ compound at RT.

	Bond length (Å)		Bond angle (°)
W1-O1	1.9406(17)	**O1- W1 -O1**	169.3(3)
W1-O1	1.9406(17)	**O1- W1 -O2**	95.31(15)
W1-O2	1.767(8)	**O1- W1 -O3**	90.45(15)
W1-O3	1.979(9)	**O1- W1 -O4**	88.96(14)
W1-O4	1.967(7)	**O1- W1 -O5**	84.70(15)
W1-O5	2.013(9)	**O2- W1 -O3**	91.9(4)
Pb1-O1	3.117(4)	**O2- W1 -O4**	94.6(4)
Pb1-O1	2.620(4)	**O3- W1 -O5**	86.7(4)
Pb1-O1	2.672(3)	**O4- W1 -O5**	86.9(3)
Pb1-O1	3.101(3)	**Mn- O5 -W1**	172.2(5)
Pb1-O2	2.946(6)	**Mn- O2 -W1**	177.4(5)
Pb1-O2	3.081(6)	**Mn- O4 -W1**	169.8(5)
Pb1-O3	2.864(6)	**W1- O3 -Mn**	177.9(6)
Pb1-O3	2.845(6)	**W1- O1 -Co/Mn**	171.2(4)
Pb1-O4	2.968(5)	**O1- Co/Mn -O1**	173.1(6)
Pb1-O4	2.637(5)	**O1- Co/Mn -O2**	93.4(3)
Pb1-O5	2.571(5)	**O1- Co/Mn -O3**	90.7(3)
Pb1-O5	3.009(6)	**O1- Co/Mn -O4**	86.7(3)
Co/Mn O1	2.0794(18)	**O1- Co/Mn -O5**	89.0(3)
Co/Mn O1	2.0794(18)	**O2- Co/Mn -O3**	91.4(5)
Co/Mn O2	2.238(14)	**O2- Co/Mn -O5**	94.6(6)
Co/Mn O3	2.025(14)	**O3- Co/Mn -O4**	84.8(5)
Co/Mn O4	2.137(14)	**O4- Co/Mn -O5**	89.3(5)
Co/Mn O5	2.155(14)		

Table A- 3 Group theory analysis of the PMCW_50 sample conducted with the use of the ISODISTORT software.[1]

Representation	Order parameter direction	Magnetic space group	Lattice base vector	Systematic absence
mGM1+⊕mY1; mGM3-⊕mY1.	P1(1)P1(1) (a;b,0)	*P mn2$_1$*	basis= {(2,0,0),(0,1,0),(0,0,1)} origin=(3/4,1/4,0)	(0 0 l) I=0 l=2n
mGM3+⊕mY2; mGM1-⊕mY2.	P1(1)P1(1) (a;b,0)	*Pm'n'2$_1$*	basis= {(2,0,0),(0,1,0),(0,0,1)} origin=(3/4,1/4,0)	(0 0 l) I=0 l=2n
mGM2+⊕mY1; mGM4-⊕mY1.	P1(1)P1(1) (a;b,0)	*P m'n2$_1$'*	basis= {(2,0,0),(0,1,0),(0,0,1)} origin=(1/4,1/4,0)	(0 0 l) I=0 l=2n+1
mGM4+⊕mY2; mGM4-⊕mY2.	P1(1)P1(1) (a;b,0)	*Pmn'2$_1$'*	basis= {(2,0,0),(0,1,0),(0,0,1)} origin=(1/4,1/4,0)	(0 0 l) I=0 l=2n+1
mGM1+⊕mY2; mGM3-⊕mY2.	P1(1)P1(1) (a;b,0)	*P mc2$_1$*	basis= {(2,0,0),(0,1,0),(0,0,1)} origin=(1/4,1/4,0)	(0 0 l) I=0 l=2n
mGM2+⊕mY2; mGM4-⊕mY2.	P1(1)P1(1) (a;b,0)	*Pm'c2$_1$'*	basis= {(2,0,0),(0,1,0),(0,0,1)} origin=(3/4,1/4,0)	(0 0 l) I=0 l=2n+1
mGM3+⊕mY1; mGM1-⊕mY1.	P1(1)P1(1) (a;b,0)	*Pm'c'2$_1$*	basis= {(2,0,0),(0,1,0),(0,0,1)} origin=(1/4,1/4,0)	(0 0 l) I=0 l=2n
mGM4+⊕mY1; mGM4-⊕mY2.	P1(1)P1(1) (a;b,0)	*Pmc'2$_1$'*	basis= {(2,0,0),(0,1,0),(0,0,1)} origin=(3/4,1/4,0)	(0 0 l) I=0 l=2n+1
mGM1+⊕mY1; mGM2+⊕mY1; mGM3-⊕mY1.	P1(1)P3(1) (a;b,b)	*P2$_1$/c*	basis= {(0,0,-1),(0,1,0),(2,0,1)} origin=(0,0,0)	(0 k 0) I=0 k=2n
mGM1+⊕mY2; mGM2+⊕mY2	P1(1)P3(1) (a;b,b)	*P2$_1$/c*	basis= {(2,0,0),(0,1,0),(0,0,1)} origin=(1/2,0,0)	(0 k 0) I=0 k=2n
mGM3+⊕mY2; mGM4+⊕mY2.	P1(1)P3(1) (a;b,b)	*P2$_1$'/c'*	basis= {(0,0,-1),(0,1,0),(2,0,1)} origin=(1/2,0,0)	(0 k 0) I=0 k=2n+1
mGM3+⊕mY1; mGM4+⊕mY1.	P1(1)P3(1) (a;b,b)	*P2$_1$'/c'*	basis= {(2,0,0),(0,1,0),(0,0,1)} origin=(0,0,0)	(0 k 0) I=0 k=2n+1
mGM1-⊕mY2; mGM4-⊕mY1.	P1(1)P3(1) (a;b,b)	*P2$_1$/c'*	basis= {(0,0,-1),(0,1,0),(2,0,1)} origin=(0,0,0)	(0 k 0) I=0 k=2n
mGM1-⊕mY1; mGM2-⊕mY2.	P1(1)P3(1) (a;b,b)	*P2$_1$/c'*	basis= {(2,0,0),(0,1,0),(0,0,1)} origin=(1/2,0,0),	(0 k 0) I=0 k=2n
mGM3-⊕mY1; mGM4-⊕mY1.	P1(1)P3(1) (a;b,b)	*P2$_1$'/c*	basis= {(0,0,-1),(0,1,0),(2,0,1)} origin=(1/2,0,0)	(0 k 0) I=0 k=2n+1
mGM3-⊕mY2; mGM4-⊕mY2.	P1(1)P3(1) (a;b,b)	*P2$_1$'/c*	basis= {(2,0,0),(0,1,0),(0,0,1)} origin=(0,0,0)	(0 k 0) I=0 k=2n+1

[1] Campbell B. J., Stokes H. T., Tanner D. E. and Hatch D. M., *"ISODISPLACE: An Internet Tool for Exploring Structural Distortions."* J. Appl. Cryst., (2006) 39, 607-614.

Table A- 3 continue

Representation	Order parameter direction	Magnetic space group	Lattice base vector	Systematic absence
mGM1+⊕mY1; mGM2+⊕mY1; mGM3-⊕mY2; mGM4-⊕mY1.	P1(1)C1(1) (a;b,c)	*Pc*	basis= {(0,0,-1),(0,1,0),(2,0,1)} origin=(0,1/4,0)	no absences
mGM1+⊕mY2; mGM2+⊕mY2; mGM3-⊕mY2; mGM4-⊕mY1.	P1(1)C1(1) (a;b,c)	*Pc*	basis= {(2,0,0),(0,1,0),(0,0,1)} origin=(0,1/4,0)	no absences
mGM3+⊕mY2; mGM4+⊕mY2; mGM1-⊕mY2.	P1(1)C1(1) (a;b,c)	*Pc′*	basis= {(0,0,-1),(0,1,0),(2,0,1)} origin=(0,1/4,0)	no absences
mGM3+⊕mY1; mGM4+⊕mY1; mGM1-⊕mY1; mGM2-⊕mY2.	P1(1)C1(1) (a;b,c)	*Pc′*	basis= {(2,0,0),(0,1,0),(0,0,1)} origin=(0,1/4,0)	no absences

Table A- 4 Fractional atomic coordinates of the $Pb_2Mn_{0.6}Co_{0.4}WO_6$ sample at 1.5 K in the *Pm'c2₁'* space group.[2]

	x	y	z	Occupancy	U_{iso}(Å^2)
Pb1	0.63069	0.03241	0.14034	1	0.0117
Pb2	0.13069	0.03241	0.14034	1	0.0117
Pb3	0.88069	0.46759	0.85966	1	0.0117
Pb4	0.38069	0.46759	0.85966	1	0.0117
W1	0.75	0.49963	0.12119	1	0.0015
W2	0	0.00037	0.87881	1	0.0015
W3	0.5	0.00037	0.87881	1	0.0015
Mn1/Co1	0.75	-0.006	0.8665	0.61/0.39	0.0011
Mn2/ Co2	0	0.506	0.1335	0.61/0.39	0.0011
Mn3/Co3	0.5	0.506	0.1335	0.61/0.39	0.0011
O1	0.62935	0.47535	0.13202	1	0.0349
O2	0.12935	0.47535	0.13202	1	0.0349
O3	0.87935	0.02465	0.86798	1	0.0349
O4	0.37935	0.02465	0.86798	1	0.0349
O5	0.75	0.72943	0.01101	1	0.0149
O6	0	0.77057	-0.01101	1	0.0149
O7	0.5	0.77057	-0.01101	1	0.0149
O8	0.75	0.26582	-0.00381	1	0.0292
O9	0	0.23418	0.00381	1	0.0292
O10	0.5	0.23418	0.00381	1	0.0292
O11	0.75	0.70236	0.25246	1	0.0154
O12	0	0.79764	0.74754	1	0.0154
O13	0.5	0.79764	0.74754	1	0.0154
O14	0.75	0.22847	0.23958	1	0.0328
O15	0	0.27154	0.76042	1	0.0328
O16	0.5	0.27154	0.76042	1	0.0328

[2] the atoms coordinates are reported without e.s.d.'s because they were not refined in the magnetic low symmetry phase.

Table A- 5 List of selected bond lengths (Å) and angles (degrees) of the Pb_2CoWO_6 compound at 150 K.

	Bond lenght (Å)		Bond angle (°)
Pb1-O1	3.147(3)	**O1-W1-O1**	169.9(3)
Pb1-O1	2.561(3)	**O1-W1-O2**	94.64(18)
Pb1-O1	2.582(2)	**O1-W1-O3**	91.98(18)
Pb1-O1	3.165(2)	**O1-W1-O4**	87.71(18)
Pb1-O2	2.954(5)	**O1-W1-O5**	85.40(18)
Pb1-O2	3.123(4)	**O1-W1-O2**	94.64(18)
Pb1-O3	2.849(4)	**O1-W1-O3**	91.98(18)
Pb1-O3	2.861(4)	**O1-W1-O4**	87.71(18)
Pb1-O4	2.937(4)	**O1-W1-O5**	85.40(18)
Pb1-O4	2.590(3)	**O2-W1-O3**	90.4(3)
Pb1-O5	2.446(3)	**O2-W1-O4**	93.5(3)
Pb1-O5	3.043(4)	**O2-W1-O5**	179.1(4)
W1-O1	1.919(3)	**O3-W1-O4**	176.1(4)
W1-O1	1.919(3)	**O3-W1-O5**	88.7(3)
W1-O2	1.848(8)	**O4-W1-O5**	87.4(3)
W1-O3	1.904(8)	**O1-Co1-O1**	159.4(7)
W1-O4	1.993(7)	**O1-Co1-O2**	100.3(3)
W1-O5	2.012(8)	**O1-Co1-O3**	88.2(3)
Co1-O1	2.094(4)	**O1-Co1-O4**	79.7(3)
Co1-O1	2.094(4)	**O1-Co1-O5**	88.2(3)
Co1-O2	1.952(14)	**O1-Co1-O2**	100.3(3)
Co1-O3	2.103(13)	**O1-Co1-O3**	88.2(3)
Co1-O4	2.360(13)	**O1-Co1-O4**	79.7(3)
Co1-O5	2.082(13)	**O1-Co1-O5**	88.2(3)
		O2-Co1-O3	97.5(6)
		O2-Co1-O4	173.8(7)
		O2-Co1-O5	103.0(6)
		O3-Co1-O4	76.3(4)
		O3-Co1-O5	159.4(7)
		O4-Co1-O5	83.1(5)
		W1-O1-Co1	164.9(4)
		W1-O2-Co1	176.0(5)
		W1-O3-Co1	168.9(5)
		W1-O4-Co1	168.6(4)
		W1-O5-Co1	164.4(5)

Table A- 6 Group theory analysis of the Pb_2CoWO_6 sample conducted with the use of the ISODISTORT software.[3]

Representation	Order parameter direction	Magnetic space group	Lattice base vector	Systematic absence
mGM1+⊕mH1; mGM3-⊕mH1	P1-P (a;b,b,0,0)	*$P2_1ma(0,1/2,\gamma)000$*	basis= {(0,0,-1,0),(1,0,0,0),(0,1,0,0),(0,0,0,1)} origin= (3/4,-1/4,0,0)	(h 0 0) I=0 h=2n
mGM3+⊕mH1; mGM1-⊕mH1;	P1-P (a;b,b,0,0)	*$P2_1m'a'(0,1/2,\gamma)000$*	basis= {(0,0,1,0),(1,0,0,0),(0,1,0,0),(0,0,0,1)} origin=(1/4,1/4,0,0)	(h 0 0) I=0 h=2n
mGM2+⊕mH1;	P1-P (a;b,b,0,0)	*$P2_1'm'a(0,1/2,\gamma)000$*	basis= {(0,0,1,0),(1,0,0,0),(0,1,0,0),(0,0,0,1)} origin=(1/4,1/4,0,1/4)	(h 0 0) I=0 h=2n+1
mGM4-⊕mH1	P1-P (a;b,b,0,0)	*$P2_1'm'a(0,1/2,\gamma)000$,*	basis= {(0,0,-1,0),(-1,0,0,1),(0,1,0,0),(0,0,0,1)} origin=(-3/4,1/4,0,1/4)	(h 0 0) I=0 h=2n+1
mGM4+⊕mH1;	P1-P (a;b,b,0,0)	*$P2_1'ma'(0,1/2,\gamma)000$*	basis= {(0,0,-1,0),(1,0,0,0),(0,-1,0,0),(0,0,0,1)} origin=(3/4,-1/4,0,1/4)	(h 0 0) I=0 h=2n+1
mGM2-⊕mH1	P1-P (a;b,b,0,0)	*P21'ma'(0,1/2,γ)000*	basis= {(0,0,-1,0),(-1,0,0,1),(0,1,0,0),(0,0,0,1)} origin=(-1/4,1/4,0,1/4),	(h 0 0) I=0 h=2n+1
mGM1+⊕mH1;	P1-P (a;b,0,b,0)	*$P2_1/b(1/2,0,\gamma)00$*	basis= {(-1,0,-1,-1),(0,0,1,0),(0,1,0,0),(0,0,0,1)} origin=(0,0,0,0)	(0 k 0) I=0 k=2n
mGM3+⊕mH1; mGM4+⊕mH1	P1-P (a;b,0,b,0)	*$P2_1'/b'(1/2,0,\gamma)00$*	basis= {(1,0,-1,0),(0,0,1,0),(0,-1,0,0),(0,0,0,1)} origin=(-1/2,0,0,0)	(0 k 0) I=0 k=2n+1
mGM1-⊕mH1; mGM2-⊕mH1	P1-P (a;b,0,b,0)	*$P2_1/b'(1/2,0,\gamma)00$*	basis= {(-1,0,-1,-1),(0,0,1,0),(0,1,0,0),(0,0,0,1)} origin=(0,0,0,1/4)	(0 k 0) I=0 k=2n
mGM3-⊕mH1	P1-P (a;b,0,b,0)	*$P2_1'/b(1/2,0,\gamma)00$*	basis= {(1,0,-1,0),(0,0,1,0),(0,-1,0,0),(0,0,0,1)} origin=(-1/2,0,0,1/4),	(0 k 0) I=0 k=2n+1
mGM4-⊕mH1	P1-P (a;b,0,b,0)	*$P2_1'/b(1/2,0,\gamma)00$*	basis= {(-1,0,1,-1),(0,0,-1,0),(0,-1,0,0),(0,0,0,1)} origin=(1/2,0,0,1/4)	(0 k 0) I=0 k=2n+1
mGM1+⊕mH1; mGM3+⊕mH1;	P1-P (a;b,b,b,-b)	*$P2_1/b(\alpha,\beta,0)00$*	basis= {(-2,-1,0,0),(1,1,0,0),(0,0,-1,0),(0,0,0,1)} origin=(0,0,0,0)	(0 k 0) I=0 k=2n
mGM2+⊕mH1; mGM4+⊕mH1	P1-P (a;b,-b,b,b)	*$P2_1'/b'((\alpha,\beta,0)00$*	basis= {(-2,-1,0,0),(1,1,0,0),(0,0,-1,0),(0,0,0,1)} origin=(0,0,0,0)	(0 k 0) I=0 k=2n+1
mGM2-⊕mH1 mGM4-⊕mH1	P1-P (a;b,b,b,-b)	*$P2_1'/b(\alpha,\beta,0)00$*	basis= {(2,-1,0,0),(-1,1,0,0),(0,0,1,0),(0,0,0,1)} origin=(0,0,0,1/4)	(0 k 0) I=0 k=2n+1
mGM1-⊕mH1; mGM3-⊕mH1	P1-P (a;b,b,-b,b)	*$P2_1/b'(\alpha,\beta,0)00$*	basis= {(-2,-1,0,0),(1,1,0,0),(0,0,-1,0),(0,0,0,1)} origin=(0,0,0,0)	(0 k 0) I=0 k=2n
mGM1+⊕mH1; mGM2+⊕mH1 mGM3-⊕mH1 mGM4-⊕mH1	P1-C (a;b,c,b,c)	*Pb(1/2,0,γ)0*	basis= {(-1,0,-1,-1),(0,0,1,0),(0,1,0,0),(0,0,0,1)} origin=(0,1/4,0,0)	no absences

[3] Campbell B. J., Stokes H. T., Tanner D. E. and Hatch D. M., *"ISODISPLACE: An Internet Tool for Exploring Structural Distortions."* J. Appl. Cryst., (2006) 39, 607-614.

Table A- 6 continue

Representation	Order parameter direction	Magnetic space group	Lattice base vector	Systematic absence
mGM3+⊕mH1; mGM1-⊕mH1; mGM4+⊕mH1	P1-C (a;b,c,b,c)	*Pb′(1/2,0,γ)0*	basis= {(-1,0,-1,-1),(0,0,1,0),(0,1,0,0),(0,0,0,1)} origin=(1/2,1/4,0,0)	no absences
mGM2-⊕mH1	P1-C (a;b,c,b,c)	*Pb′(1/2,0,γ)0*	basis= {(1,0,-1,0),(0,0,1,0),(0,-1,0,0),(0,0,0,1)} origin=(-1/2,-1/4,0,0)	no absences
mGM1+⊕mH1; mGM3+⊕mH1; mGM3-⊕mH1; mGM1-⊕mH1;	P1-C (a;b,b,c,-c)	*$P2_1(\alpha,\beta,0)0$*	basis= {(0,1,0,0),(1,0,0,0),(0,0,-1,0),(0,0,0,1)} origin=(1/4,1/4,0,0)	(0 k 0) I=0 k=2n
mGM2+⊕mH1; mGM4+⊕mH1	P1-C (a;b,-b,c,c)	*$P2_1'(\alpha,\beta,0)0$*	basis= {(0,1,0,0),(1,0,0,0),(0,0,-1,0),(0,0,0,1)} origin=(1/4,1/4,0,0)	(0 k 0) I=0 k=2n+1
mGM2-⊕mH1 mGM4-⊕mH1	P1-C (a;b,-b,c,c)	*$P2_1'(\alpha,\beta,0)0$*	basis= {(0,-1,0,0),(-1,0,0,0),(0,0,-1,0),(0,0,0,1)} origin=(-1/4,-1/4,0,0)	(0 k 0) I=0 k=2n+1
All combinations	P1-C (a;b,c,b,-c))	*P-1(α,β,γ)0*	basis= {(0,1,0,0),(1,0,0,0),(0,0,-1,0),(0,0,0,1)} origin=(0,0,0,0)	no absences
All combinations	P1-4D (a;b,c,d,e)	*P1(α,β,γ)0*	basis= {(0,1,0,0),(1,0,0,0),(0,0,-1,0),(0,0,0,1)} origin=(0,0,0,0)	no absences

Table A- 7 Fractional atomic coordinates of the PCW sample at 2 K in the *Pm'c2₁'* space group.[4]

	x	y	z
Pb1	0.7565	0.0332	0.1461
Pb2	0.2569	0.465	0.8575
W1	0	0.506	0.1073
W2	0.5	-0.007	0.8803
Co1	0	0.016	0.8809
Co2	0.5	0.496	0.1303
O1	0.761	0.482	0.1409
O2	0.261	0.022	0.8705
O3	0	0.76	0.02
O4	0.5	0.767	-0.001
O5	0	0.269	-0.006
O6	0.5	0.262	-0.007
O7	0	0.694	0.244
O8	0.5	0.785	0.749
O9	0	0.239	0.231
O10	0.5	0.313	0.76

[4] the atoms coordinates are reported without e.s.d.'s because they were not refined in the magnetic low symmetry phase.

Acknowledgments/Ringraziamenti

I would to thanks all the people that help me with this thesis work starting with all the researchers, professors and students that try with me to unlock the mystery of multiferroics.

First I would like to thank my supervisors for supporting me patiently all these Ph.D. years. Prof. Calestani thanks for all the advice, crystallography lessons and for always let me "white paper" in the laboratory, leaving me to follow every good or bad idea. Thanks, also, for the passion for scientific research that you had conveyed to me.

Thanks to Dr. Righi that has taught me everything he knew on the super-space and diffraction and having followed me step by step in this research. Thanks for all the help with the experiments in facilities.

Dr. Mezzadri thanks for your patience and for all the things you taught me, for suffer with me the infernal heat of the office, and for having patiently answered my questions, sometimes really stupid, and for help with the experiments at the facilities.

A big thanks goes to Dr. Pascal Manuel and Dr. Dmitry Khalyavin for welcoming me on their beam line throughout my 5-month Erasmus. Pascal thanks for all the help for arrange my visit, for help with the house, for all the kindness. Thanks also for all you've taught me on diffraction and on WISH especially for allowing me to stay as far as possible on the beam line. Dmitry

thanks for all the discussion about symmetry and for try to teach me some group theory.

I also want to thank all the people who have carried out some of the physical characterisations. Thanks to Prof. Solzi, Dr. Pernechele and Dr. Porcari for all magnetic measurements and for the patience for all the samples that I sent. Dr. Cabassi and Dr. Bolzoni for the electrical and pyrocurrent measurements and for putting at my disposal their experience. Dr. Migliori for the wonderful TEM images and fantastic electron diffraction pattern. Prof. Zappettini and Dr. Calestani for borrow me the tube furnace for all synthesis. Dr. Delmonte, my mate in the multiferroic odyssey, and Dr. Pernechele for the electrical hysteresis measurements. Thanks to Dr. Prodi for the help with some neutrons experiments. A sincere thanks to Dr. Merlini for the help on my first experiment at the synchrotron, has been a very busy week.

A big thanks goes to Dr. Ritter of the ILL institute for the help with the neutron diffraction experiment and for inviting me, giving me the opportunity to explain my work at the ILL.

A grateful thanks goes to the ILL institute and the ESRF institute of Grenoble for making at my disposal the neutron and synchrotron diffraction facilities. Thanks to ISIS facility of Didcot (UK) to giving measure time at the facility and for host me during my Erasmus period.

A dutiful thanks goes to prof. Dalcanale who coordinated the doctorate course during these three years.

Roberta grazie per tutto l'aiuto in qualsiasi cosa, in laboratorio, in ufficio con i vari documenti, spedizioni, ordini di vetrerie reagenti ecc… e grazie anche per la compagnia in ufficio e per tutti i preziosi consigli di questi anni.

Come non ringraziare tutti i ragazzi del LAB che hanno reso le giornate in dipartimento molto più divertenti. Andrea grazie mille per tutto l'aiuto con i sol ma soprattutto per le lunghe chiacchierate nelle pause e per il "mitico" caffe.

Ilaria grazie per tutti i suggerimenti e per tutte le info sulla Titania "ciccina" che sono certo che cambierà il mondo, soprattutto con le nuove (segrete, folli) idee!! E ovviamente per tutte le news sui nuovi corsi alla moda nelle palestre. Claudia grazie per le chiacchierate e per tutto l'aiuto con la burocrazia del dottorato e dell'Erasmus.

Dopo aver ringraziato tutti gli "accademici" è il momento di ringraziare tutte quelle persone che mi sono state accanto in questi tre incredibili anni. Le persone da ringraziare per questo lavoro sono tantissime e c'è sempre il rischio di dimenticarsi qualcuno, spero di non farlo ma nel caso sappiate che non è fatto di proposito ma ormai inizio a odiare questo "bellissimo" programma di scrittura…

Per primi voglio ringraziare i miei genitori! Finalmente siamo alla fine degli studi c'è l'abbiamo fatta!! Senza di voi non avrei neanche iniziato quest'odissea, grazie per tutto l'appoggio, per i consigli, per la pazienza che avete dimostrato. Per avermi supportato in tutte le mie scelte, anche quando pensavate non fossero le più sagge, nei miei sogni e nelle mie passioni. Grazie per avermi insegnato a essere responsabile e a capire l'importanza delle cose, a essere onesto con me stesso e con gli altri. Sono sicuro di non avervi mai ringraziato a sufficienza per tutto e di sicuro questo non è il luogo adatto ma GRAZIE!!!

Un bacio gigante a Cecilia, senza il tuo supporto tutto questo non sarebbe stato possibile, mi hai sostenuto in tutto questa lunga avventura stando sempre al mio fianco, portandomi sempre serenità e gioia in tutti questi anni seguendomi addirittura in terra straniera!

Un doveroso grazie va a tutta la mia famiglia: Matti, Alle, Zio, Zia, Marci, Vero, Nonne, che è sempre stata a disposizione nel caso avessi avuto bisogno e hanno seguito da vicino tutta questa lunga avventura.

Come non ringraziare la Grande famiglia del Kyu Shin Do Kai: Maestro, President, Lucia, Derna, Max, Michele, Luca, Chiara, Giulia, Francesco, Clara tutti i miei compagni di squadra dai più "piccoli" cadetti ai "vecchi" senior. Grazie mi avete insegnato a non mollare mai, che le difficoltà sono solo un passaggio lungo il percorso, che le preoccupazioni sono solo uno spreco di energia e che l'importante non è l'arrivo ma il percorso che uno compie. A tutti i piccoli allievi della scuola che ho avuto il privilegio di "seguire", grazie per tutte le emozioni i bei momenti e grazie per tutto quello che mi avete insegnato.

Infine volevo ringraziare tutti gli amici che hanno reso più spensierati questi anni. Tizio, Luca, Rava, ormai siamo insieme da tantissimi anni siamo stati un po' sparsi per tutto il mondo ma questo non ci ha assolutamente fermato. Fava grazie per essere sempre a disposizione per qualsiasi malsana idea culinaria, e per aver messo a disposizione la magione per far baracca. Gec, Delca e Giulia per essere sempre pronti a far baldoria tutti insieme.

Grazie a tutto il Circolo Della Domenica Culturale per tutte le splendide giornate, grigliate, cavallate giornate in piscina. Fortunatamente siamo tantissimi e per ringraziare tutti mi servirebbe un'altra tesi, ma spero che avremo l'occasione di festeggiare. Comunque W il CDDC (che è palindromo).

Fabio Orlandi